2003-04-29

Electrostatic Density Measurements in Green-State P/M Parts

Georg H. Leuenberger
Worcester Polytechnic Institute

ELECTROSTATIC DENSITY MEASUREMENTS IN GREEN-STATE PM PARTS

by

Georg H. W. Leuenberger

A Dissertation

Submitted to the Faculty

of the

WORCESTER POLYTECHNIC INSTITUTE

in Partial Fulfillment of the Requirements for the

Degree of Doctor of Philosophy

in

Electrical Engineering

by

_____

April 2003

APPROVED:

Professor Reinhold Ludwig, Major Advisor	Professor Robert A. Peura
Professor Diran Apelian	Professor John M. Sullivan, Jr.
Professor William R. Michalson	Professor John Orr, ECE Department Head

Abstract

The goal of this research is to show the feasibility of detecting density variations in green-state powder metallurgy (P/M) compacts from surface voltage measurements. By monitoring a steady electric current flow through the sample and recording the voltages over the surface, valuable information is gathered leading to the prediction of the structural health of the compacts. Unlike prior research that concentrated on the detection of surface-breaking and subsurface defects, the results presented in this thesis target the density prediction throughout the volume of the sample. The detection of density variations is achieved by establishing a correlation between the conductivity and their respective density. The data obtained from the surface measurements is used as part of an inversion algorithm, calculating the conductivity distribution, and subsequently the density within the compact.

In a first step, the relationship between conductivity and density of green-state P/M compacts was investigated. Tests were conducted for a number of parts of various powder mixtures. In all cases a clear correlation between conductivity and density could be established, indicating that measurements of electric conductivity could indeed be exploited in an effort to render valid information about the density of the sample under test. We found a linear correlation for non-lubricated parts and a non-linear behavior for lubricated samples. Specifically, it was found that the conductivity increases with increasing density only up to a maximum value obtained at approximately 6.9g/cm^3. Interestingly, any additional density increase leads to a reduction of the conductivity. This behavior was confirmed to be inherent in all powder mixtures with lubricants. The thesis research is able to provide a physical model and a mathematical formulation describing this counter-intuitive phenomenon.

A finite element solver in conjunction with an inversion algorithm was then implemented to study arbitrarily shaped part geometries. Based on the principles of electric impedance imaging, the developed algorithm faithfully reconstructs the density distribution from surface voltage measurements.

The feasibility of the instrumentation approach for both simple and complex parts can be demonstrated using a new sensor concept and measurement arrangement. Measurements were performed on both geometrically simple and complex parts.

Acknowledgments

This dissertation would not have been possible without the help and support from many people. My heart felt appreciation goes to my advisor Reinhold Ludwig, whose enthusiasm for scientific research and the exploration of new areas was a great inspiration during all my work. His guidance and support helped me through all the problems that arose along the way.

Special thanks go to Diran Apelian and the members of the Powder Metal Research Center, who supported my work in numerous ways. Especially the members of the focus group contributed greatly through many helpful, constructive discussions. Also they provided special P/M samples for my research and helped with the development of sensors. I am grateful for the financial support I received from the PMRC.

My thanks go to Bill Michalson, Bob Peura and John Sullivan for serving on my committee and for their constructive comments that helped improve my dissertation.

In addition, I would like to thank all my friends and colleagues at the RF lab and throughout the department for making this time enjoyable and memorable.

And I want to thank “the women behind the man”. Without the continued support of my two daughters Sara and Laura and my wife Bea, this whole adventure would never have been possible. Thank you for believing in me!

Table of Contents

List of Figures

1 Problem Statement

1.1. Goals and Objectives

Nondestructive evaluation of is an integral part of any manufacturing process. It even gains in importance for industries that produce goods in high volume with a low cost per piece. In such an industrial setting, process monitoring and early process intervention is crucial to the commercial success of a product.

The production of metallic parts through compaction from metal powders fits this description exactly. Due to the innovative metal handling processes in powder metallurgy (P/M), quality control is essential in gaining new markets that were traditionally held by metal casting or forging companies. A number of destructive and nondestructive techniques are available to monitor the quality of the P/M processes. However, none of the nondestructive methods is currently applicable to the pre-sintered, green-state.

Past research into the electrostatic crack detection of surface-breaking and subsurface defects in pre-sintered green-state P/M compacts has resulted in an array sensor concept [43]. In this concept current is injected into the sample and voltage distributions on the surface are processed in an effort to detect hairline cracks as small as 20 microns in size [46]. This electrostatic current flow concept is applicable to P/M compacts, since the green-state P/M specimens are generally moderate to low conducting samples. Therefore, even small currents can produce a detectable voltage profile across the surface that can be recorded by an array of sensing probes arranged in a planar or non-planar configuration [47, 71]. The presence of flaws, which are due to conductivity contrasts, can be sensed through a local voltage perturbation against the unflawed baseline voltage response [8].

In extending the theory of the previously developed crack detection approach from two to three dimensions, it is reasoned that the same electrostatic approach may be applied to detect density gradients in green-state compacts. However, although the basic idea is the same, the two approaches are fundamentally different. The main difference between crack detection and the

measurement of density variations lies in the fact that the former implies a microscopic exploitation of high differences in conductivity between the metal compact and its microscopically small defects such as air inclusions, whereas the latter requires the macroscopic evaluation of potentially low differences in conductivity. As a result, the electrostatic evaluation approach differs in both its evaluation and processing methodology.

The goal of this project is to develop a new theory and method that allows the monitoring of density variations in green-state powder metallurgy parts through resistivity measurements. The idea is to detect differences in the conductivity within a compact and relate this change in conductivity to a density variation. Since the method should be nondestructive, we have only access to the surface of the device under test.

Two versions of the method can be envisioned. The first, simple version does not calculate a full density map of the part. Rather it records the surface voltages resulting from a specific current injection pattern and compares this pattern against the voltage pattern recorded on other parts. This allows discriminating quickly between compacts of acceptable quality and parts that exhibit unacceptably large density variations within their volume. The second version of the method would record the voltage pattern in the same way, but then calculate a full density map through an inversion algorithm.

1.2. Approach

The project was analyzed and, after reviewing the literature, an approach was devised that should develop the necessary theory as well as provide results from practical measurements. In this respect, research milestones have been defined that account for the key items that have to be addresses in this project:

- Establish correlation between density and electric conductivity of green-state P/M compacts with the ultimate aim of detecting density variations through electric conductivity measurements. Prior information on this relationship is currently not available, so that it has to be established through suitable measurements.
- In taking the results from the first step, we need to formulate a generic mathematical voltage-current-conductivity model for green-state P/M compacts.
- Develop an algorithmic approach to infer density distributions from voltage measurements recorded over the compact's surface. This algorithm will be based on algorithms found in current electric impedance imaging. It converts the recorded voltages to con-

ductivity predictions via an inverse algorithm, and then from the knowledge of the conductivity distribution to the density distribution.

- Propose instrumentation that monitors density distributions. This instrumentation can be different depending on the desired result of production monitoring or full density analysis of the compact.

1.3. Organization

After this section, which introduced the project goal and the research approach taken, the main content of this thesis is subdivided into six sections.

Section 2 introduces the reader to the basic principles of powder metallurgy (P/M) and the P/M industry. It also contains a review of non-destructive evaluation techniques employed on P/M parts discussing their advantages and limitations. Special emphasis is given to the problem of measuring density in P/M compacts, since the goal of this project is to measure density variations.

Section 3 is a theoretical part of this thesis, investigating the propagation of electric current injected into 2D and 3D models. Understanding the propagation of the current and the resulting differences of electric potential on the surface are key to a successful interpretation of voltage measurements on analyzed P/M samples.

In section 4, work is reported establishing a relationship between the conductivity and the density of green-state P/M samples. Since the literature does not yet contain any significant results in this respect, a series of measurements had to be conducted to establish this relationship. Subsequently, the physical basis for the results is explained in a new model.

Section 5 contains the work related to the inversion of the measured voltages and their mapping into a density distribution. This work is based of the electric impedance tomography (EIT) principles. An introduction to EIT is given. Then the specific algorithms used to calculate the impedance distribution in P/M compacts are discussed and the novel application of EIT to green-state P/M parts is introduced.

The results of density measurements on both geometrically simple and complex parts are reported in section 6. An initial measurement series was conducted on cylindrical parts, which allowed the verification of the density reconstruction algorithm through conventional, destructive techniques. Further measurements were then performed on a complex shaped three level gear. The applicability of the method in an industrial setting is discussed.

Section 7 summarizes the findings and draws conclusions from the presented research results.

Section 8 contains suggestions and thoughts toward possible future work in the area that would extend the project results and continue its introduction into the industrial setting.

2 Introduction to Powder Metallurgy

2.1. The Powder Metallurgy Industry

Powder metallurgy (P/M) is a manufacturing method, where metal parts are made by pressing metal powder mixtures into the desired shape under high pressures. One of the attractions of P/M is its versatility when compared to other metalworking technologies. Modern P/M is a fast-growing industry that is replacing the traditional metalworking approaches with a low-cost, high-efficiency process [18].

There are many reasons, why P/M has become an important manufacturing technology for metal parts. First are the many applications that rely on the low cost production of complex parts. Components for the automotive industry represent a good example of this area. P/M provides a technology that is very attractive in both the cost and the precision. The P/M process is material and energy efficient. The finished product typically utilizes 97% of the metal powder consumed, and the sintering process producing the solid state bonding between the particles consumes much less energy compared to the energy required to melt metals [1]. Another reason for the popularity of P/M parts is the ability to mix powders with unique micro structural properties, which cannot be achieved by other metalworking techniques [24].

The initial interest in powder metallurgy grew from the desire to find new, lower cost ways to form the common elements like copper or iron. Initially, the availability of powders dictated the evolution of the P/M industry. Still iron based powders represent the majority of the materials used to produce powder based compacts. Probably more exciting than the evolution of powder mixtures is the evolution of the applications of P/M products that the industry has undergone. Initially, P/M parts were selected simply for their low cost. More recently, improvements in the processes, quality control, and powder mixtures shifted the focus to high quality parts maintaining tight tolerances [24]. It is the combination of high quality and cost effectiveness that holds the promise of a bright future for the P/M industry.

Powder metallurgy uses a set of processes that is fundamentally different from traditional metalworking such as casting, machining and forging. In P/M parts are produced in three basic production steps:

- powder mixing,
- compaction, and
- sintering.

The metal parts are formed from metal powders, previously mixed to the desired composition, by compressing them into a die at high pressure. These compacts are then sintered – heated to a temperature below the melting point of the base material in a controlled atmosphere furnace - to produce the final products [29, 34]. All these manufacturing processes are fully automated, very fast and efficient. However, in order to maintain the cost advantage over other manufacturing methods, stringent quality assurance measures have to be put in place, because the occurrence of flaws in the products can significantly reduce the output and efficiency of the process, adversely affecting cost.

2.1.1. Powders

All powder processing starts with the main ingredient, the powder. Metal powders are precisely engineered materials that meet a wide range of performance requirements. They are available in numerous types and grades, their properties being affected by three factors [1]:

1. Material type
2. Powder fabrication process
3. Component fabrication techniques.

One of the big advantages of the P/M process is the ability to produce alloys in an easy way by simply mixing different powders. The selection of the alloy greatly influences the properties of the final compact. By mixing powders, one can produce alloys which are very difficult or even impossible to produce with conventional techniques. Recent developments in powder manufacturing techniques even allow bonding the alloying materials to the bulk material particles, this way achieving optimal mixing properties. All these possibilities open up a wide field of applications for P/M parts.

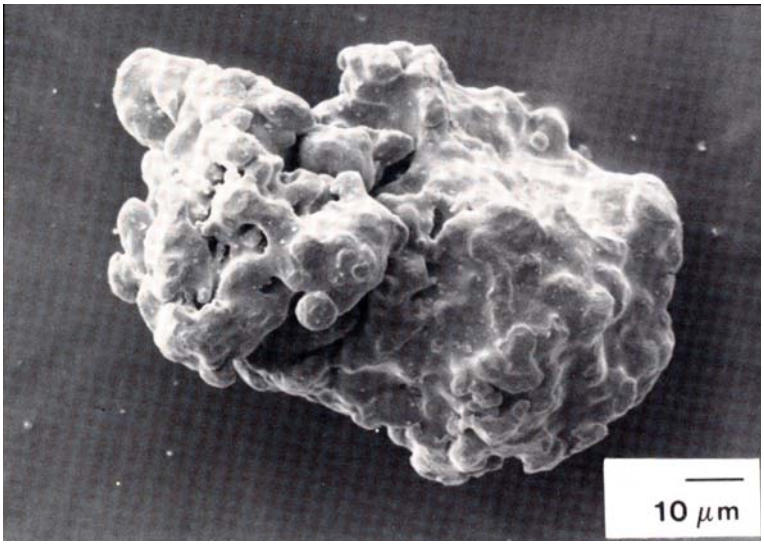

Figure 2.1: Typical shape of an atomized iron particle [30].

Next to the selection of the base material, particle size distribution is the most important property of powder characterization. Powders can be manufactured with virtually any particle size, the manufacturing cost being the limiting factor. Measurement of the particle sizes, however, is not an easy task. As illustrated in Figure 2.2, particle shapes can be highly irregular, rendering a repeatable measurement difficult. Furthermore, particle sizes within a powder vary and the powder has to be characterized with a particle size distribution rather than with a single size. Figure 2.1 depicts the typical shape of an atomized iron as seen under an electron microscope.

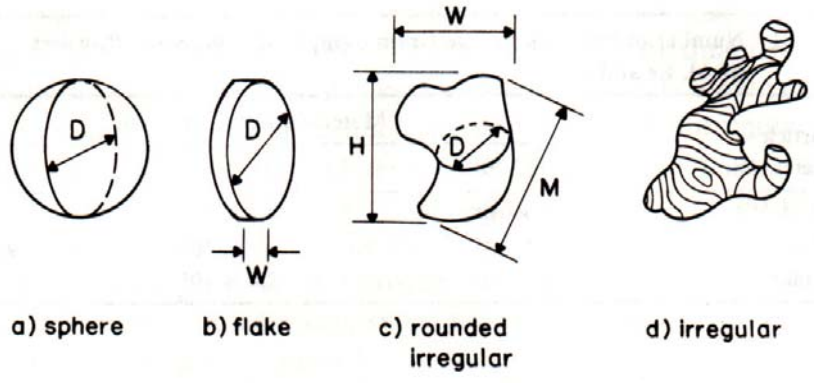

Figure 2.2: Various particle shapes and possibilities to measure their size [24].

Most metal powders used to manufacture P/M parts are mixed with a lubricant. The main function of the lubricant is to reduce friction between the P/M compact and the die wall and between the powder particles. The lubricant is usually non-metallic, and only makes up a small percentage of the mixture, on the order of 1%. However, it plays an important role in the compaction cycle.

A major loss of compaction energy takes place because of the friction forces in non-lubricated powders. Minimizing these friction induced losses allows greater pressure to be applied to the powder for a given loading and thus achieving higher compaction densities and green strength [30, 68]. Equally important is the reduction of the friction encountered during the ejection of the compact from the die. One of the most difficult tasks is the efficient ejection of the compacts without damaging the parts. Diminishing the frictional forces through lubricant addition helps both to reduce the die wear and to ease ejection.

Since the lubricant is a non-metallic substance of far lower specific weight than the main powder, adding lubricant actually reduces the specific weight of the mixture. A critical concentration of lubricant can be found for each system below which the green density for a given pressure is greater than the non-lubricated powder - due to the reduced friction -, and above which it may become lower again – due to the increased amount of material with lower specific weight [30].

2.1.2. Compaction

Figure 2.3 illustrates the compaction process for a simple, single-level P/M part. A three-piece set of an upper punch, lower punch and a die are used for shaping and compacting the powder. In a first step, the lower punch is positioned to let a pre-determined amount of powder enter the die. Powder is vibrated into the die from an external feed shoe, with possible motion of the lower punch at the same time, assisting the powder to pack uniformly. When the required amount of powder has entered the die, the feed shoe is removed and the upper punch enters the die, as illustrated in step two. Subsequently, pressure is applied to both punches compacting the powder. At the end of compaction, shown in step three, the powder experiences the highest pressure. In step four, the upper punch is removed, and the lower punch ejects the compact out of the die. The product of this compaction process is the so-called green-state compact, the strength of these compacts is termed the green strength.

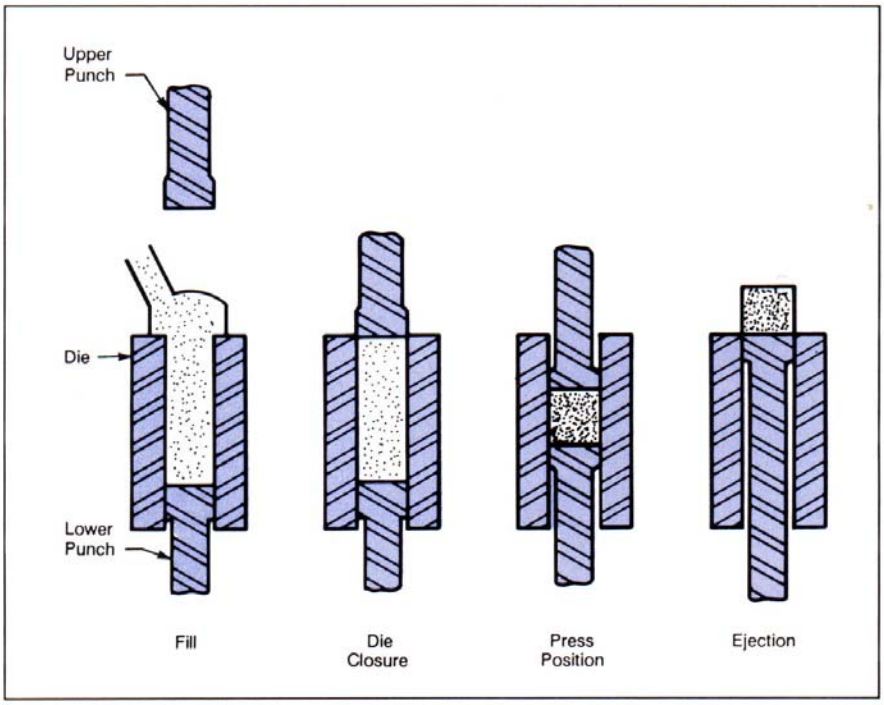

Figure 2.3: Tool motions during a compaction cycle [29].

The green-state compact consists of metal powder particles pressed together. Although the green-state compacts look to the eye like any solid metal part, there are no bonds in the compact other than interparticle bonds created through the deformational forces that pressed the metal particles together. Consequently, the green-state compact is very fragile and susceptible to damage.

The press shown in Figure 2.2 has very a simple configuration. In reality, to create complex P/M parts as shown in Figure 2.4, the upper and lower punches can have multiple moving components, and the assembly may contain core rods and other components [36]. All these complications cause the pressure during compaction to be irregular and vary throughout the volume of the part. As a result, problems with cracking may start to appear when the pressure is not entirely equal everywhere. These cracks are particularly frequent in places where there is a sharp change in pressure, such as a step in a core rod or the interface between two punches. The subject of cracking in P/M components is a well known problem and has been thoroughly investigated. As a result the most favored crack locations can be accurately predicted [82].

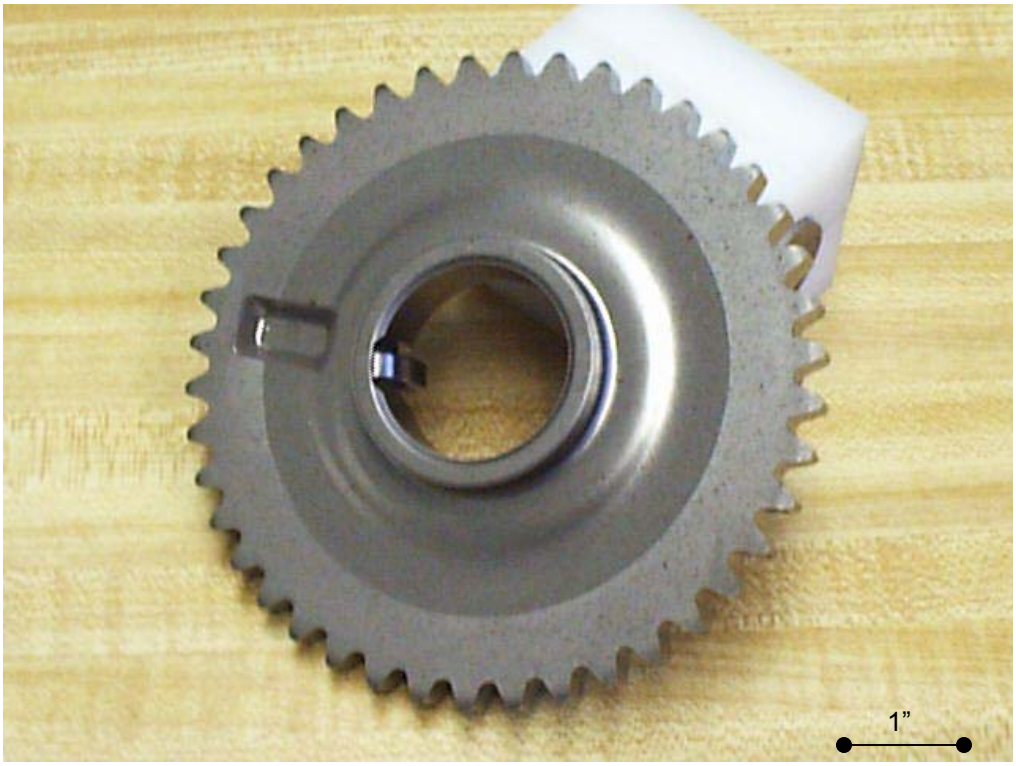

Figure 2.4: Complex, multi-level P/M part (courtesy of BorgWarner).

2.1.3. Sintering

Sintering is the process where metal powder particles form bonds at temperatures below the melting point. The contact points between particles, which were originally formed under the mechanical pressure during compaction, increase in size and strength, improving mechanical properties.

After compaction, the green-state part is transferred to a sintering furnace, where it is heat treated for up to several hours. Although the temperature inside the furnace is below the melting point of the metal, it causes a significant transformation in the microstructure of the P/M compact. First, the individual particles start to weld together, forming solid bonds between them, as illustrated in Figure 2.5. After prolonged exposure to these elevated temperatures, the particles form grains, creating the same structure found in solid metal parts. The only remaining difference between such P/M compacts and solid metal are pores, which come from air gaps that are still in the part. After sintering, these gaps become isolated, nearly spherical pores in the material.

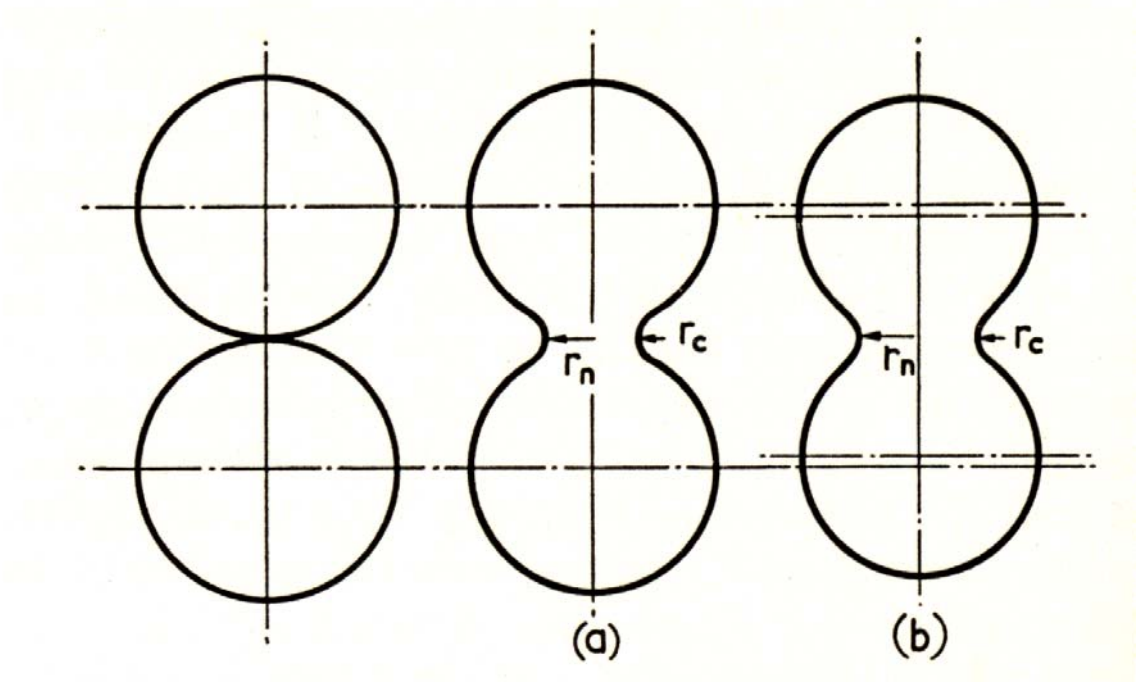

Figure 2.5: Interparticle bond formation during sintering without (a) and with (b) overall shrinking of the part dimensions [30].

An additional important accomplishment of the sintering process it the removal of the lubricant and any organic materials from the powder mixture. Although lubricants are required to enhancing the compaction properties and the green strength of the compact, they ultimately weaken the final product and should be removed as far as possible. This is achieved during sintering, since these substances evaporate or oxidize at the temperatures used in the furnace. Therefore the typical sintering cycle consists of three phases:

- A preheat section, where the temperature of the part is slowly elevated and lubricant or other additives are evaporated.
- The main section, where the temperature is at its highest and interparticle bonds form.
- A cooling cycle, slowly bringing the temperature back to room temperature to avoid distortions or crack development caused by temperature shocks or uneven cooling.

2.1.4. Quality Measures in P/M

The properties of parts produced by a P/M process have similar properties to parts produced by conventional metal working techniques. Therefore, many of the properties characterizing the quality of such P/M compacts are the same as for regular alloys. Three groups of such quality measures apply directly to both types of processes. These are [62]:

- Mechanical properties, such as strength, toughness and fatigue life.
- Physical properties, including thermal, electrical and magnetic characteristics.
- Surface properties, such as catalytic, filtration and corrosion behavior.

It is important to note that a quality measure applied to P/M compacts cannot be directly compared to the same property of a cast or wrought metal part. While the method of testing is often identical in both cases, the different nature of the structure of these parts will result in different outcomes. Especially the surface properties will be significantly different from wrought or cast alloys to P/M compacts. However, the method of characterizing the quality remains the same in both cases.

A next group of quality measures applies only to P/M alloys. These properties measure the quality of a product with respect to either the powder that was used, or the process it was produced in. Measures that fall into these categories are:

- Microstructural characteristics like grain size, dispersion of phases.
- Measures qualifying the pore structure, including pore size, porosity, pore shape and interconnectivity.

These quality measures are directly influenced by the quality of the raw material and the production process. It is therefore essential that these properties are closely monitored, even more so as it is obvious that these microstructural properties also directly influence the mechanical quality of the P/M compacts.

2.2. Nondestructive Evaluation of P/M Parts

Powder metallurgy is a technology in which the goal of the manufacturing process is usually either to achieve the highest possible quality or the lowest possible cost. To do either necessitates very close control over every operation and step, from the raw powder to the finished product [34]. As complete a knowledge as is economically possible is required at every stage of production.

The described P/M production process can be very efficient, as all the three main tasks can be performed independently and their resource requirements are low compared to traditional metal working procedures. However, in order to take full advantage of the modularity of the process, each step should be monitored to guarantee the product quality. In reality, quality assurance is usually applied only to the finished state [44]. This can cause a significant reduction on production efficiency. One may consider the situation of a malfunctioning press that starts to produce defective parts due to a worn out tool. The delay from compaction to quality assurance inspection can be hours to days in which thousands of defective parts are produced. All these parts would have to be either scrapped or inspected individually.

As a special metal working technique, P/M also has special requirements for quality assurance. While the inspection of dimensional tolerances and the search for cracks and material impurities is similar to conventionally produced metal parts, P/M compacts also require the verification of their density. This includes not only the average density, but even more importantly the density distribution within a compact. Unfortunately, no reliable non-destructive tests have been found that allow the measurement of density distributions, especially not for green-state compacts. Current non-destructive testing on P/M parts is therefore limited to crack detection and the measurement of average densities.

Process control in P/M starts with the assessment of the powder quality. However, besides the measurement of the particle size and shape, the powder properties can only be observed in the properties of the compacted parts through [18]:

- Behavior during pressing
- Properties of the green compact
- Behavior during sintering
- Properties of the sintered compact

When considering the three basic P/M steps of mixing, compacting, and sintering, it is the compaction process producing the green-state parts that offers the highest pay-off for quality control through nondestructive evaluation (NDE) techniques. Detection of compaction related problems in the green-state will permit early process intervention, and thus prevent the creation of potentially significant numbers of faulty parts prior to sintering.

Numerous tests can be performed to analyze the properties of P/M compacts. The following list names the ones that are most commonly employed in the industry [29]:

- Dimensions
- Weight

- Density determination
- Permeability tests
- Electric resistivity
- Mechanical strength
- Micro-macrostructure
- Structural defects

For a specific test to be applicable on a large number of parts, it has to be non-destructive. Many of the above mentioned physical tests can only be performed on a few compacts, since they will render the inspected part unusable. A set of non-destructive tests has to be identified that sufficiently characterizes the production quality without reducing the production efficiency by an intolerable amount.

The properties of sintered P/M parts are very similar to those of solid metals. Therefore, all the methods developed for NDE of metals are applicable. These NDE methods include eddy current, electrical resistivity and ultrasonic testing, thermal imaging, x-ray inspection, and many others [30, 44]. Some of these methods are actively used in the industry to inspect finished P/M components.

The properties of the green-state P/M compacts, however, are different. Due to the amorphous structure of the compressed powder, where particles only adhere through mechanical forces, most of the NDE techniques applied to solid metals cannot be applied successfully.

The following paragraphs discuss the available NDE techniques and discuss their shortcomings with respect to the inspection of green state P/M parts.

2.2.1. Eddy Current Testing

Eddy current testing involves the use of time varying magnetic field produced by a test coil to excite circulating currents in electrically conductive materials. These induce currents are called eddy currents. The eddy currents oppose the magnetic field set up by the test coil and generate in turn an induced time-varying magnetic field. The strength of the magnetic field in the coil then becomes a function of the eddy current distribution inside the sample. A defect in the material causes a change in the eddy current, changing the secondary magnetic field and resulting in a change of the impedance of the coil. This impedance change can be detected. This allows using eddy currents for flaw detection in metal samples.

Many factors affect the flow of eddy currents in the inspected parts. The following list discusses a few of these factors:

- Sample conductivity: Higher conductivity increases the eddy currents generated by a particular magnetic field and increases measurement sensitivity.
- Discontinuities: The occurrence of discontinuities, such as cracks or pores, redistributes the eddy current flow and can be monitored as changes of the electric impedance of the test coil.
- Sensor lift-off: The distance between the test coil under the inspected part directly influences the coil impedance. Therefore it is important to keep this distance constant at all times, since variations might trigger false impurity detections.
- Skin effect: Due to the skin effect, the penetration depths changes with the excitation frequency. Lower frequencies allow better penetration, higher frequencies, on the other hand, increase the signal sensitivity.

Eddy current testing is well suited to inspect sintered P/M parts. Since a relatively high number of defects are expected to occur at or near the surface, eddy current testing ideal to investigate these parts. However, this is only true for sintered parts. The amorphous structure of green-state P/M parts exhibits electric conductivities that are lower than for sintered parts by several orders of magnitude. This greatly reduces the ability to excite eddy currents in green parts and subsequently reduces detection sensitivity. In addition, the irregular distribution of particles in the compact complicates the eddy current patterns, further reducing measurement accuracy. The effects of these problems can be reduced by increasing the excitation frequency. As a result, eddy current testing is still somewhat successful in detecting surface and near-surface flaws in green-state compacts, but it cannot be used to inspect the deeper regions.

2.2.2. Ultrasonic Inspection

Ultrasonic testing is one of the most widely used NDE methods. It can be used to analyze many different material properties. Its main application, however, is the detection and characterization of internal material impurities or flaws.

In ultrasonic testing, sound waves are transmitted into the device under test, usually through a piezoelectric transducer. These sound waves are reflected or scattered at various impedance discontinuities within the part. The energy of the reflected sound waves is then converted back into a voltage by a receiving transducer. The received voltage can now be analyzed and characterizes the material properties of the inspected part.

Advantages of the ultrasonic inspection methods are numerous. By sending these acoustic waves deep into the part, ultrasonic test systems are capable of detecting and locating even

small flaws within the body of the part. Also is the required test equipment inexpensive when compared to many of the other NDE techniques. A large variety of ultrasonic inspection systems is available on the market.

Ultrasonic testing is widely used for inspection of sintered P/M parts to detect cracks, determine density variations or monitor the sintering process. However, the method is unsuccessful when applied to green-state P/M parts, since the porous structure of the pressed powder presents extremely high attenuation to the sound waves. The penetration depth is therefore no longer sufficient to adequately test the parts. Furthermore, the coupling of the transducers to the part under test often requires the presence of a fluid or gel, which is unacceptable for green-state P/M compacts.

2.2.3. X-Ray Inspection

X-ray inspection is a long known technique most widely used in the medical field. It is based on the absorption of X-rays by the sample under test. An X-ray image, depicting the internal composition of the sample under test, can be compared to that of an unflawed reference sample to detect flaws. Although X-ray imaging applies to many different types of materials and can be used also on green-state P/M compacts, it has some general disadvantages. The slow inspection speed and the expensive equipment render the technique ill-suited for high volume, low cost applications.

Regarding the application of X-ray inspection to P/M parts and green-state P/M parts in particular, there are no physical limitations as with many of the other NDE techniques. Full test coverage of the whole production at several production stages could be implemented with one technique. However, the typical flaws in P/M parts occur near the surface or near corners or edges. In these locations, flaws are difficult, if not impossible to detect with X-rays.

2.2.4. Thermal Imaging

The basic principle of thermal imaging involves the mapping of surface temperatures over time, when thermal energy flows through the part under test. The flow of the thermal energy follows the diffusion equation

$$\frac{\partial T}{\partial t} = \frac{k}{c\rho}\nabla^2 T\,, \tag{2.1}$$

where T represents the temperature, k the thermal conductivity, c the specific heat of the medium and ρ the density of the part. The solution to Equation (2.1) indicates a specific heat flow pattern for a given part. A flaw in the device under test causes this heat flow pattern to change, where both changes of absolute temperature or changes in temperature gradients can be observed.

Thermal imaging is usually performed by depositing a defined amount of thermal energy onto parts of the surface inspected of the device that diffuses through the material. Special infrared cameras monitor the surface temperature distributions, indicative of the heat flow inside the sample. The temperature data is fed into an imaging algorithm and can be used to automatically determine a variety of material properties and detect flaws.

The ability to analyze compacts of virtually any shape has resulted in many applications of thermal testing of sintered products in the P/M industry. The cost and expertise required to run a thermal imaging system (heat source, infrared camera, image acquisition hardware and software) are the only limitations to this technique. However, thermal imaging has not yet been applied successfully to green-state P/M compacts. The potential of this technique in its application on green-state parts is again limited by the high attenuation, the same issue as encountered with ultrasonic and eddy current testing.

2.2.5. Electrical Resistivity Inspection

Special emphasis is given to the electrical resistivity measurements, since our research approach focuses on this technique (see also section 1.2).

The electrical impedance non-destructive evaluation method is based on the four-wire impedance measurement method. While in principle two wires are enough to supply a current flow and record a voltage drop over an unknown impedance, the four-wire method has the advantage to accurately measure impedance without the effects of lead and contact resistance. The principle is simple: a well controlled current is supplied by a current source through two leads and the voltage drop across the resistor is measured with a voltmeter attached to two other leads. This method is illustrated in Figure 2.6. Since the current source provides the same amount of current regardless of the impedance it is presented with, the current flowing through the unknown impedance equals the source current, independent from the contact resistance R_1. The voltage recording device finds the voltage drop over the unknown impedance through comparing the measurement current to the current through the impedance. The volt meter actually records:

$$V_{meas} = I_V * R_{\text{int}ernal} = I_{source} * \frac{R_{meas}}{R_{meas} + R_{\text{int}ernal} + 2R_2}. \qquad (2.2)$$

Because the internal impedance of a voltmeter is so high compared to the unknown impedance (usually on the order of 1MOhm), the current flowing through it is virtually non-existent. Hence, we can neglect the error voltage from R2 in (2.2). As a result the contact impedances of the probes do not affect the measurement in this arrangement.

A non-destructive testing instrument using the resistivity method was invented around 1960 at the AT&T Bell Laboratories. This traditional electrical resistivity inspection method uses four in-line probes to contact the surface of a material of unknown, but assumed constant conductivity. A current source is used to inject an electric current into the device under test through the outer probes and the resulting voltage drop is measured across the inner probes. The measurement arrangement is depicted in Figure 2.7. The measured voltage is indicative of the material conductivity in that region. The recorded conductivity value can then be used to characterize and compare the inspected devices. A change in material properties or the presence of inclusions or flaws can be monitored as a change in the material resistivity.

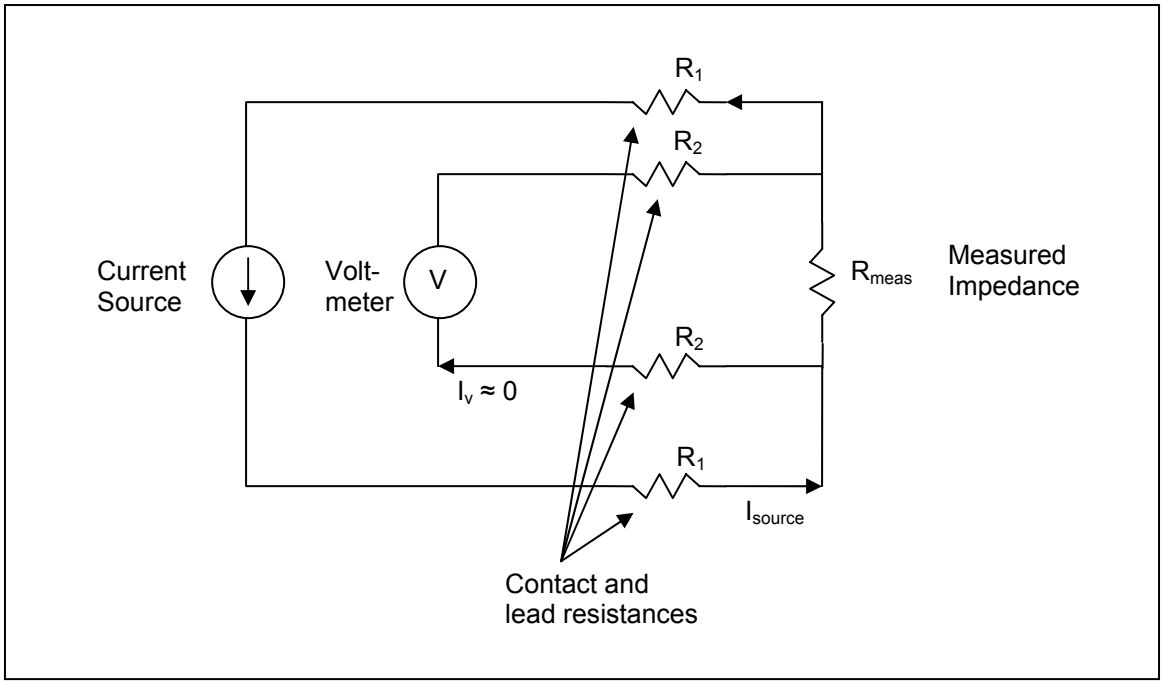

Figure 2.6: Four-probe impedance measurement setup.

In this arrangement, the relationship between the measurements and the material conductivity is more complicated and can no longer be approximated by the ratio of current and voltage. Since we cannot assume the direction and the density of the current throughout the material to be constant, the geometry of the part has to be taken into consideration. If the solid is large enough so that we can assume it to extend to infinity with respect to the dimensions of the probe

placement, then boundary effects can be neglected and the underlying Laplace equation can be solved by modeling the solid as a half-space. In this simplified geometry, the relationship between the unknown conductivity σ, the injected current and the recorded voltage is given by:

$$\sigma = \frac{I}{2\pi V}\left[\left(\frac{1}{r_1}-\frac{1}{r_2}\right)-\left(\frac{1}{r_3}-\frac{1}{r_4}\right)\right]. \tag{2.3}$$

Equation (2.3) is an analytical solution of the current flow in a uniform conducting half-space [9]. If the material is relatively thin and the effects of current flow extending to the edge of the material have to be taken into consideration – as is the case in a sheet of metal - the material thickness enters the equation as a correction factor [44].

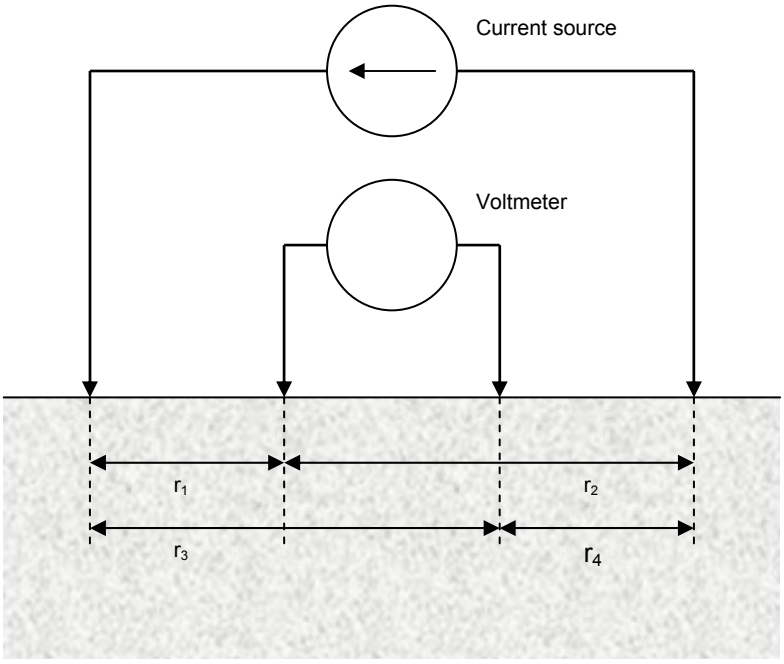

Figure 2.7: Four-probe setup for resistivity measurement [9].

In P/M compacts, resistivity is a good indicator of material properties. The technique can be used on both sintered and green-state parts. Its application is not limited by properties specific to P/M compacts but rather by the limitations of the technique itself. Since current cannot be directed within the part but rather distributes according to the physical laws, the resolution and the application to specific areas of interest are limited. Nevertheless, successful implementations

have shown the technique's value especially in the detection of surface and near sub-surface flaws. When a flaw is present between the voltage probes, the resistivity reading will be higher than normal and the flaw can be detected.

Several versions of this method have been investigated in recent years. The traditional four-probe inline resistivity inspection as developed by AT&T has two main disadvantages. First, the sensor must be moved across the entire surface of the part, rendering the inspection very slow. Second, the spacing of the probes allows only to either increase the resolution by placing the probes close together, or increasing the ability to detect deep subsurface flaws, but not both at the same time.

These limitations have been addressed by an apparatus for crack detection in green-state P/M compacts developed at Worcester Polytechnic Institute [8, 71]. This crack detection system extends the four-probe approach by applying a grid of spring loaded needle contacts to the surface of the tested part. While current is still injected through two of the contacts, a large number of differential voltages are recorded between the remaining probes covering the part under test. It is the voltage distribution that is subsequently processed in a signal processing algorithm and results in the detection and location of surface and sub-surface flaws. Flaws caused a perturbation in the voltage signals when compared to flawless samples, and this perturbation can be detected using a statistical algorithm [9].

2.2.6. Other Techniques

Numerous other techniques have been invented to inspect P/M products. Some of these techniques are named in the following list:

- Resonance frequency testing
- Magnetic particle inspection
- Liquid penetration measurement

Each technique finds a specialized application and supporters for certain cases. All of them have only limited application, if any at all, regarding the inspection of green-state P/M parts. The special composition of the green-state samples with respect to their amorphous structure, their low mechanical strength and high attenuation provides insurmountable obstacles for the successful application for all of these techniques.

2.3. Density Measurements in P/M Compacts

Density measurements have a special importance in P/M produced parts. The many reasons for this are rather obvious. Since P/M compacts are produced from a powder, the density of the part promises direct characterization of the powder purity, the quality of the filling and compacting processes, and , ultimately, of the mechanical strength of the final product. Hence most P/M component properties are closely related to the final density.

The density of P/M compacts can be expressed in two ways. It can be either recorded in the regular units of weight per unit volume, usually in g/cm^3, or it can also be expressed as percent of theoretical density, which is the ratio of the density of the P/M component to that of its cast metal counterpart. This measure gives direct information about the remaining porosity of the part, where a part with 85% theoretical density is said to have a porosity of 15%.

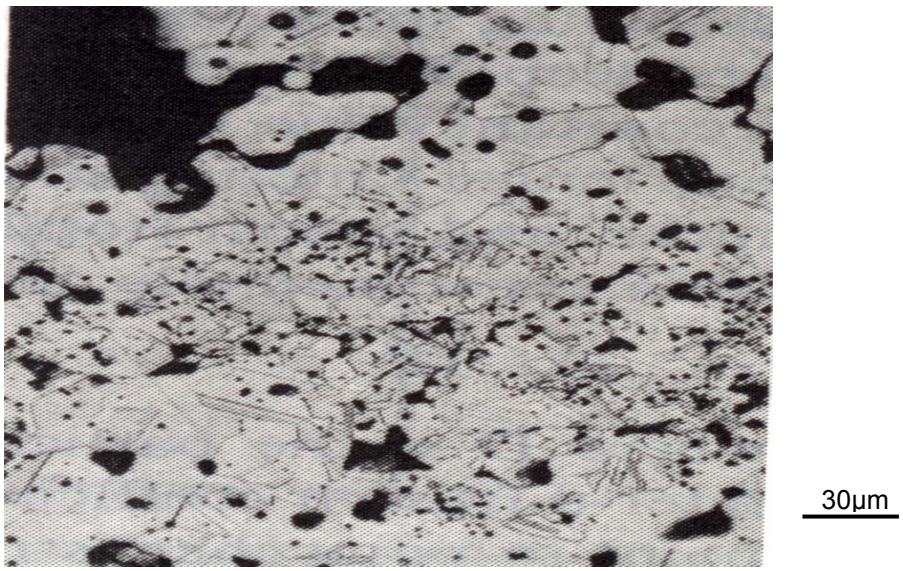

Figure 2.8: Micrograph of a sintered P/M compact from a bronze alloy (90% copper, 10% tin) [1].

Density measurements in P/M compacts are not an easy task and most methods fall short when applied to this special situation. While most of the above mentioned non-destructive measurement techniques detect local changes in density, they usually can only find regions, where the density differs by orders of magnitude from the average density of the bulk material. This situation includes all the flaw detection methods, where flaws consist of material impurities or cracks, all locally reducing the apparent density drastically. However important and useful these measurements are, they cannot provide information on density variations due to process inconsistencies.

Apart from the very local density measurements that enable the detection of inclusions or cracks, all other non-destructive techniques available today only allow to measure an average density for the whole part. This means that they simply measure the weight and the part dimensions, and from that calculate the average density. The only method that allows measuring a density distribution within the P/M part, in both the green and sintered state, is by micrographs. In this method, the part is cut into several thin slices that subsequently are analyzed under the microscope. By measuring the area of the pores compared to the area of the metallic material, a local density can be calculated. Figure 2.8 shows such a micrograph for a sintered bronze alloy, where the remaining pores are clearly visible.

3 Current Flow in 2 and 3 Dimensions

An important step toward understanding the results from voltage measurements on a conductive part is the insight into the flow of electric current in two and three dimensions. In many cases one is only concerned about the macroscopic view of current flowing through an impedance. In such a case we are not concerned about the direction of the current flow, but merely assume a uniform current density throughout the volume, with the current flowing from higher to lower potential. In the case of DC current, this behavior can be mathematically described by the relationship of voltage and current over a resistor:

$$V = IR\,, \tag{3.1}$$

where R is the lumped resistance value, I is the current flowing through the part and V is the resulting drop in potential.

This simplified view, however, does no longer apply to a scenario, where current is injected into a part through contacts, whose surfaces are small compared to the measured part, and where voltages are measured in several positions on the surface. In order to calculate the voltage distribution and the current flow within the measured part, we now have to find a solution to Laplace's equation

$$\nabla \cdot \sigma \nabla \Phi = 0\,, \tag{3.2}$$

given the boundary conditions of the injected current density at defined locations on the boundary of the part. In general, we have to assume a non-uniform conductivity in the sample. This spatial dependency of the conductivity makes both $\sigma = \sigma(x, y, z)$ and $\Phi = \Phi(x, y, z)$ a function of the spatial coordinates x, y, z. In the case of a uniform conductivity, (3.2) reduces to

$$\nabla^2 \Phi = 0\,. \tag{3.3}$$

Generally, a closed form solution for (3.2) cannot be found. In some cases, where the geometry is such that a closed solution to the resulting integrals can be found, the flow of the current and the resulting voltage distribution can be determined anywhere in the geometry. The following paragraphs go through a two-dimensional and a three-dimensional case that are both of interest to our research.

3.1. Two Dimensional Current Flow

Let us consider two concentrical circular regions of conductive materials as shown in Figure 3.1. The inner circular area has a radius R_0 and conductivity σ_0, the outer ring has a radius R_1 and conductivity σ_1. A current I of strength I_0 is applied to this part through point contacts at the angular position $\varphi = 0$ and a current sink of equal magnitude at position $\varphi = \pi$, so that

$$I = I_0(\delta(\xi) - \delta(\xi - \pi)), \tag{3.4}$$

In order to find the steady state voltage distribution and current flow pattern in this circular region, we need to solve Equation (3.2). Rewriting (3.2) in polar coordinates, we get:

$$\frac{1}{r}\frac{\partial}{\partial r}\left(r\frac{\partial \Phi}{\partial r}\right) + \frac{1}{r^2}\frac{\partial^2 \Phi}{\partial \varphi^2} = 0. \tag{3.5}$$

Using the method of the separation of variables, we separate the dependence of Φ on r and φ into two separate functions, each depending on only one of the two independent variables:

$$\Phi(r,\varphi) = S(r)T(\varphi). \tag{3.6}$$

Using these variable separated functions, (3.5) becomes

$$\frac{r}{S(r)}\frac{\partial}{\partial r}r\left(\frac{\partial S(r)}{\partial r}\right) + \frac{1}{T(\varphi)}\frac{\partial^2 T(\varphi)}{\partial \varphi^2} = 0. \tag{3.7}$$

Equation (3.7) can now be solved for S(r) and T(φ) independently as we can write

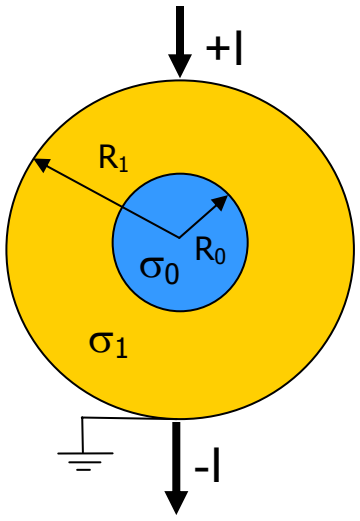

Figure 3.1: **Current injection into two concentric rings with different electric conductivity.**

$$r\frac{\partial}{\partial r}r\left(\frac{\partial S(r)}{\partial r}\right)=r\frac{\partial S(r)}{\partial r}+r^2\frac{\partial^2 S(r)}{\partial r^2}=w^2S(r), \tag{3.8}$$

where w is independent of r:

$$-w^2=\frac{1}{T(\varphi)}\frac{\partial^2 T(\varphi)}{\partial\varphi^2}. \tag{3.9}$$

Since (3.8) and (3.9) are now simple differential equations of one variable, we can solve them and find

$$\begin{aligned} &S(r)=Ar^w \quad \text{or} \quad S(r)=Br^{-w} \\ &T(\varphi)=C\cos(w\varphi) \quad \text{or} \quad T(\varphi)=D\sin(w\varphi) \end{aligned} \tag{3.10}$$

Substituting these solutions back into (3.6) and making the appropriate assumptions according to the physical situation, we get the following electric potentials for the inner and outer rings respectively:

$$\begin{aligned}\Phi_0(r,\varphi) &= Ar^n\cos(n\varphi)\\ \Phi_1(r,\varphi) &= \left(Br^n + Cr^{-n}\right)\cos(n\varphi)\end{aligned} \tag{3.11}$$

The unknown constants A, B, and C can now be calculated by taking into account the proper boundary conditions of the problem. In words, these boundary conditions can be stated as follows:

- The potential at the inner boundary between the two areas must be continuous.
- The current flow at this inner boundary must be the same in both regions.
- The current flow at the outer boundary is defined by the two points of the current source and the current sink.

Additionally, the potential was fixed to 0 at the current sink location. This convention is arbitrary, but we need to fix the potential at one point in the volume to make the solution unique. Mathematically, these boundary conditions allow us to setup up the following three equations:

$$\Phi_0\Big|_{r=R_0} = \Phi_1\Big|_{r=R_0} \tag{3.12}$$

$$\sigma_0 \frac{\partial\Phi_0}{\partial r}\Big|_{r=R_0} = \sigma_1 \frac{\partial\Phi_1}{\partial r}\Big|_{r=R_0} \tag{3.13}$$

$$\sigma_1 \frac{\partial\Phi_1}{\partial r}\Big|_{r=R_1} = I(r,\varphi) \tag{3.14}$$

Using (3.12), (3.13), and (3.14) to evaluate the proportionality constants, we find for the potential in the region of interest

$$\Phi(r,\vartheta) = \begin{cases} \sum_{n=1,3,5,\ldots}^{\infty} b(n)(h-1)r^n\cos n\vartheta\,, & r \le R_0 \\ \sum_{n=1,3,5,\ldots}^{\infty} b(n)(-r^n + hR_0^{2n}r^{-n})\cos n\vartheta\,, & R_1 \ge r \ge R_0 \end{cases}, \tag{3.15}$$

where $h = \dfrac{\sigma_1 - \sigma_2}{\sigma_1 + \sigma_2}$, $\qquad b(n) = \dfrac{2I_0}{\pi\sigma_2 n}\dfrac{R_1^{n+1}}{R_1^{2n} + hR_0^{2n}}$.

The series in the solution converges quickly and can be approximated with only a few terms of the sum. The series was programmed in Matlab® and the results of the simulations are

shown in the following figures. Figures 3.2, 3.3, and 3.4 illustrate the current flow and the potential distribution in the case, where the outer ring is highly conductive compared to the center of the circular area. One can clearly see that the current flows primarily in this outer ring and avoids penetrating the region with lower conductivity.

Figure 3.5 and Figure 3.6 show the results when the conductivities of the two regions are reversed. The differences are clearly visible, showing that the current now prefers to find a path through the highly conductive center region. The changes in the pattern of the equipotential lines can also be clearly observed.

These simulations illustrate the mechanisms that allow observing changes in the conductivity of a solid by measuring voltages on its surface. The changes in the current flow result in different voltage patterns that can be recorded without having access to the inner parts of the measured device.

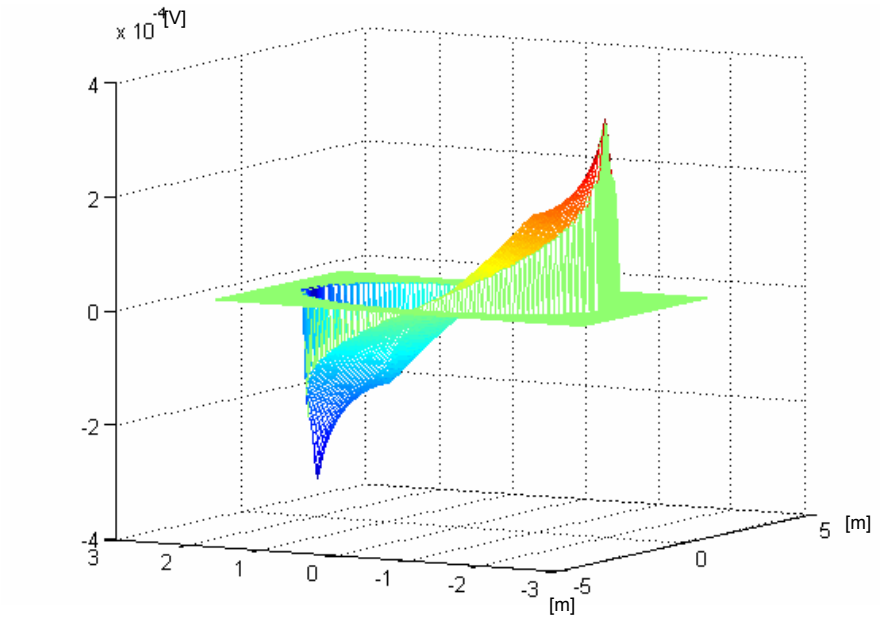

Figure 3.2: Potential distribution in an area with R_0=1m, σ_0=1000 S/m, R_1=2m, σ_1=10000 S/m when injecting a current of 1A, visualized in a 3D-surface graph.

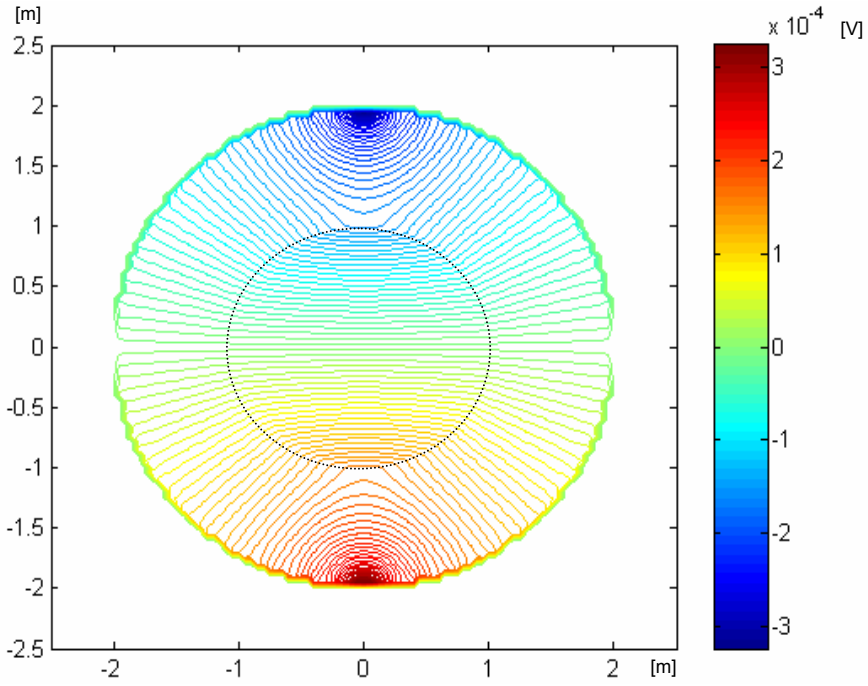

Figure 3.3: **Equipotential lines in an area with R_0=1m, σ_0=1000 S/m, R_1=2m, σ_1=10000 S/m when injecting a current of 1A.**

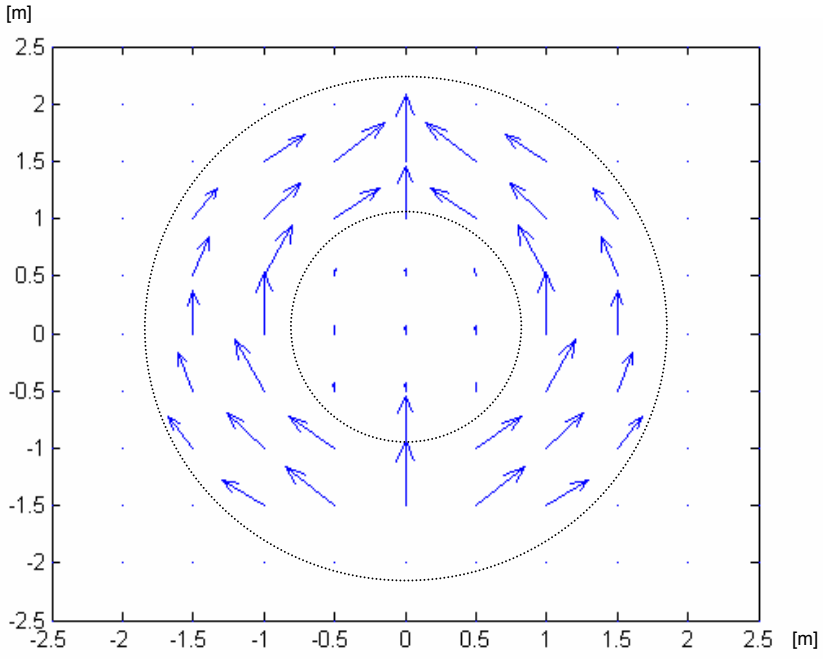

Figure 3.4: **Current flow vectors in an area with R_0=1m, σ_0=1000 S/m, R_1=2m, σ_1=10000 S/m when injecting a current of 1A, where the length of the arrow symbolizes the magnitude of the vector.**

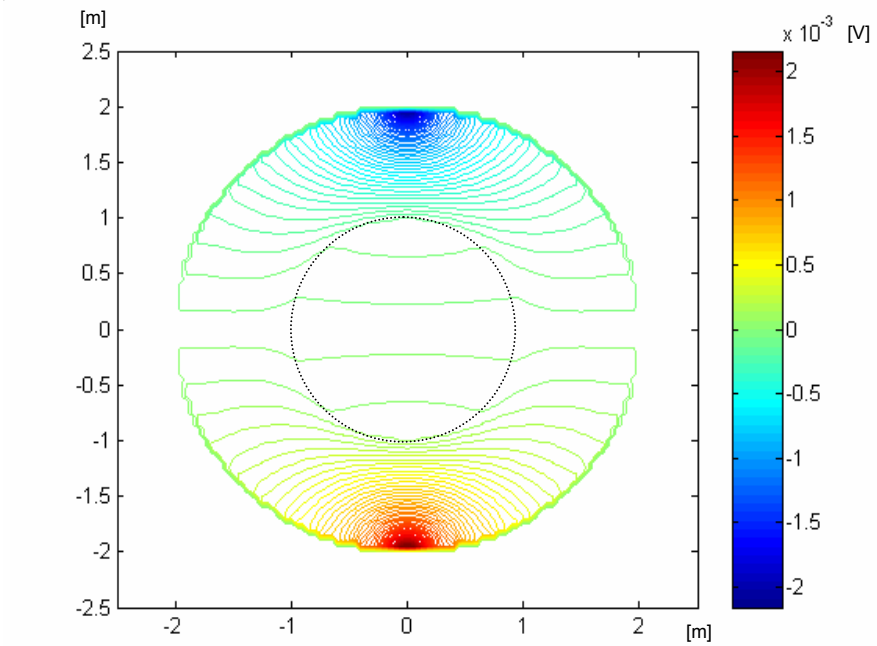

Figure 3.5: **Equipotential lines in an area with R_0=1m, σ_0=10000 S/m, R_1=2m, σ_1=1000 S/m when injecting a current of 1A.**

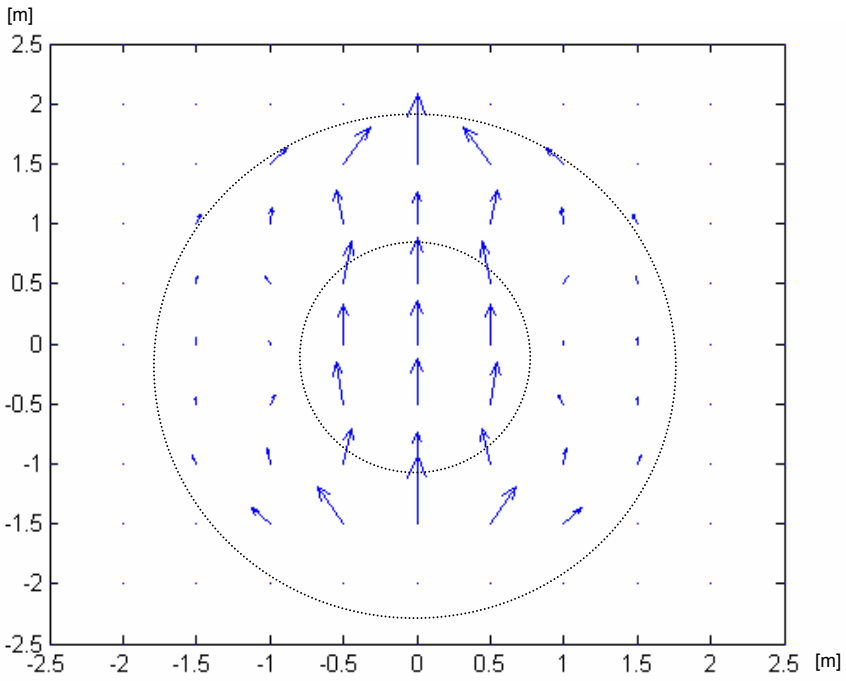

Figure 3.6: **Current flow vectors in an area with R_0=1m, σ_0=10000 S/m, R_1=2m, σ_1=1000 S/m, where the length of the arrow symbolizes the magnitude of the vector.**

3.2. Three Dimensional Current Flow

3.2.1. Basic equations

The electric current flow through a P/M compact can be cast in terms of an electrostatic model formulation of Laplace's equation whereby the surface currents and voltages represent boundary conditions, and the conductivity σ is in general spatially non-uniformly distributed throughout the part. Previously, we assumed the conductivity to be constant in a predefined region and not vary with location. Generally, this is not true and hence, the voltage $\Phi(\mathbf{r})$, as a function of the spatial observation vector $\mathbf{r} = \mathbf{r}(x,y,z)$, is therefore given by the generalized Laplace equation [28]

$$\nabla[\sigma(\mathbf{r})\nabla\Phi(\mathbf{r})] = 0\,. \tag{3.16}$$

The practically relevant boundary condition involves a prescribed current density input

$$J_n = \sigma\frac{\partial\Phi}{\partial k} = -\sigma\nabla\Phi \tag{3.17}$$

(where ***k*** denotes the normal vector at the boundary) over an otherwise flux free surface. This current density is normal to the sample surface whose surface normal ***k*** is pointing outwards. An alternative approach involves Poisson's equation where the current excitation is incorporated as part of the right hand side source term

$$\nabla[\sigma(\mathbf{r})\nabla\Phi(\mathbf{r})] = -I\delta(\mathbf{r}-\mathbf{r}_0)\,. \tag{3.18}$$

Here $\mathbf{r}_0$ denotes the location of the current source *I*. and δ is the delta function. Although the conductivity cannot be regarded as homogeneous throughout the volume, we will for the moment consider this specialized case, which allows us to simplify Equation (3.19) considerably. For homogeneously conductive samples Equation (3.18) reduces to

$$\nabla^2\varphi(\mathbf{r}) = -I\delta(\mathbf{r}-\mathbf{r}_0)/\sigma\,. \tag{3.19}$$

To develop a potential solution in a cylindrical (r, θ, z) coordinate system of a sample with total radius R and length L subject to flux-free (or Neumann-type) boundary condition, we develop a spectral solution by utilizing eigenfunctions of the form [57, 58]

$$\Psi_{mnp}(\mathbf{r}) = J_m(\lambda_{mn} r / R)\cos(m\theta)\cos(p\pi z / L)\,. \tag{3.20}$$

Here $J_m(\lambda_{mn} r / R)$ is the Bessel function of order *m*. Index *n* denotes the zeros of the first derivative of the Bessel function, i.e. $J_m'(\lambda_{mn}) = 0$, as required to satisfy the flux-free boundary condition. These functions can be expanded as part of a Green's function expansion [58]

$$G(\mathbf{r} \mid \mathbf{r}_0) = \frac{I}{\sigma}\sum_{m,n,p}^{\infty} \frac{\overline{\Psi}_{mnp}(\mathbf{r}_0)\Psi_{mnp}(\mathbf{r})}{(\lambda_{mn}/R)^2 + (p\pi/L)^2}\,, \tag{3.21}$$

where the overbar is used to denote an orthonormal set. The function $\overline{\Psi}_{mnp}$ is found by applying the orthonormality conditions of the Bessel functions J_m [75]

$$\int_0^R J_m(\lambda_{mn} r / R) J_m(\lambda_{mn'} r / R)\, r dr = \frac{R^2}{2}\left(1 - \frac{m^2}{\lambda_{mn}^2}\right) J_m^2(\lambda_{mn})\delta_{nn'}\,, \tag{3.22}$$

orthogonality of trigonometric functions $\cos(m\theta)$

$$\int_0^{2\pi} \cos(m\theta)\cos(m'\theta) d\theta = 2\pi\delta_{mm'} / \varepsilon_m\,, \tag{3.23}$$

and orthogonality of trigonometric functions $\cos(p\pi z / L)$

$$\int_0^L \cos(p\pi z / L)\cos(p'\pi z / L) dz = L\int_0^1 \cos(\pi p x)\cos(\pi p' x) dx = L\delta_{pp'} / \varepsilon_p\,, \tag{3.24}$$

where the primed indices indicate identical functions but with different values of the running index.

In (3.23) and (3.24) we use the Neumann factor

$$\varepsilon_m, \varepsilon_p = \begin{cases} 1, m = 0,\ p = 0 \\ 2, \text{otherwise} \end{cases}$$

This leads to the orthonormal eigenfunctions

$$\overline{\Psi}_{mnp}(\mathbf{r}) = \left\{ \frac{\varepsilon_m \varepsilon_p}{\pi L R^2 \left(1 - \frac{m^2}{\lambda_{mn}^2}\right) J_m^2(\lambda_{mn})} \right\} \Psi_{mnp}(\mathbf{r}) . \tag{3.25}$$

Substituting (3.20) and (3.25) into (3.21) permits us to develop a series expression for the Green's function in the form

$$G(\mathbf{r} \mid \mathbf{r}_0) = \frac{I}{\sigma} \sum_{m,n,p=0}^{\infty} [G_{mnp} J_m(\lambda_{mn} r / R) \cos(m\theta) \cos(\pi p z / L) \\ J_m(\lambda_{mn} r_0 / R) \cos(m\theta_0) \cos(\pi p z_0 / L)] \tag{3.26}$$

where the coefficient G_{mnp} is a combination of the orthonormality condition (3.25) and the eigenvalue expression in (3.21). Evaluating the integrals, we explicitly obtain

$$G_{mnp} = \frac{\varepsilon_m \varepsilon_p}{\pi L R^2 \left(1 - \frac{m^2}{\lambda_{mn}^2}\right) \left(\frac{\lambda_{mn}^2}{R^2} + \frac{\pi^2 p^2}{L^2}\right) J_m^2(\lambda_{mn})} . \tag{3.27}$$

A simplification of expressions (3.26) and (3.27) can be achieved if the cylinder is axis-symmetric. Since this implies independence of angle θ, we can re-write (3.26) as

$$G(\mathbf{r} \mid \mathbf{r}_0) = \frac{I}{\sigma} \sum_{n=0,p=0}^{\infty} G_{np} J_0(\lambda_n r / R) \cos(\pi p z / L) \cos(\pi p z_0 / L) . \tag{3.28}$$

where the coefficient G_{np} in (3.28) is given by

$$G_{np} = \frac{\varepsilon_p}{\pi L R^2 \left(\frac{\lambda_n^2}{R^2} + \frac{\pi^2 p^2}{L^2}\right) J_0^2(\lambda_n)} . \tag{3.29}$$

Evaluation of (3.28) is a rapidly converging series, typically requiring fewer than 20 terms to achieve satisfactory precision.

In the above calculations we are considering the source to be a true point source and the solution presented in (3.28) is strictly speaking only valid for an infinitely small point source. Such a source cannot be practically implemented. In reality, every source will exhibit some finite contact area, through which the current is flowing into the part. The following paragraphs discuss the extension of the point source solution to the solution for a source with finite aperture.

Let us consider a ring source with an external radius R_A and internal radius R_B as seen in Figure 3.7. According to the superposition principle, we can subdivide our source of finite aperture into small subsections. The effect of each of the sub sources is summed up to give the effect of the whole source. In (3.26), the term related to the source component is

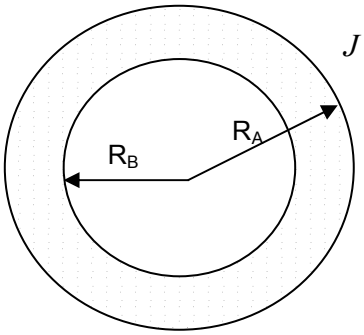

$$J = I / A = \frac{I}{(R_A{}^2 - R_B{}^2)\pi}$$

Figure 3.7: Illustration of ring current source with strength I.

$$J_m(\lambda_{mn} r_0 / R)\cos(m\theta_0)\cos(\pi p z_0 / L)\,. \tag{3.30}$$

Replacing the point source by a number N of sub sources which build the mentioned ring source, the term in (3.30) becomes

$$\sum_{i=1}^{N} J_m(\lambda_{mn} r_{0i} / R)\cos(m\theta_{0i})\cos(\pi p z_{0i} / L)\,, \tag{3.31}$$

where due to the symmetry in the axis symmetric cylinder only the term depending on r_{0i} truly depends on the actual shape of the source. The other two terms either vanish completely or are constant with respect to the size of the source. Taking the symmetry and geometric dependencies into account, the term depending on the shape and size of the source reduces to

$$\sum_{i=1}^{N} J_m(\lambda_{mn} \frac{r_{0i}}{R}) . \tag{3.32}$$

In the limit $N \to \infty$ and representing the position and size of the sub sources in polar coordinates, (3.32) becomes

$$\frac{1}{\left(R_A{}^2 - R_B{}^2\right)\pi} \int_{R_B}^{R_A} \int_{0}^{2\pi} J_0\left(\lambda_n \frac{r_0(\rho,\varphi)}{R}\right) \rho \, \partial\rho \, \partial\varphi . \tag{3.33}$$

Due to the symmetry the integral over the angle is constant. The remaining integral of the zero order Bessel function can be evaluated using the identity

$$\int_0^1 x^{1-\nu} J_\nu(ax) \partial x = \frac{a^{\nu-2}}{2^{\nu-1}\Gamma(\nu)} - a^{-1} J_{\nu-1}(a) . \tag{3.34}$$

Using this integral relationship and adjusting the integration borders to reflect our ring source dimensions, we find for the integrated source term

$$\frac{2R}{\left(R_A{}^2 - R_B{}^2\right)\pi} \left[R_A J_1\left(\lambda_n \frac{R_A}{R}\right) - R_B J_1\left(\lambda_n \frac{R_B}{R}\right) \right] . \tag{3.35}$$

This expression can now be used in (3.28) so that the final series for any ring source that is axis symmetric with the cylinder and lies on its face becomes

$$G(\mathbf{r} \mid \mathbf{r}_0) = \frac{I}{\sigma} \frac{2R}{\left(R_A{}^2 - R_B{}^2\right)\pi} \sum_{n=0,p=0}^{\infty} \frac{G_{np} J_0(\lambda_n r / R) \left[R_A J_1\left(\lambda_n \frac{R_A}{R}\right) - R_B J_1\left(\lambda_n \frac{R_B}{R}\right) \right]}{\times \cos(\pi p z / L) \cos(\pi p z_0 / L)} . \tag{3.36}$$

Equation (3.36) is again a fast converging series requiring less than 20 terms to achieve acceptable precision. Furthermore, additional mathematical manipulations allow reducing the double series to a single series, so that the calculation becomes even easier. It is worth noting that the solution presented for a ring source is valid for all possible combinations of source radii, s long as $R_A > R_B$. When $R_B = 0$, the source becomes a disc that is concentric with the cylinder. In the case $R_A = R_B = 0$, the source degenerates to a point source and (3.36) becomes the same as (3.28) for a point source.

3.2.2. Current flow through a three-dimensional cylinder

The electric voltage predictions are conducted based on the generic test arrangement shown in Figure 3.8. In particular, point and rod electrodes are employed to initiate the current flow distribution throughout the compact of uniform conductivity. If a uniform current flow is injected into the sample (Figure 3.8, right), we can expect a simple current-voltage relation based on Ohm's law

$$V = \frac{I L}{\sigma A}, \tag{3.37}$$

where *A*, *L* denote, respectively, sample surface area, and length. For the point electrode excitation (Figure 3.8, left) the theoretical Green's function model (3.28) with flux-free boundary conditions solving (3.19) has to be utilized.

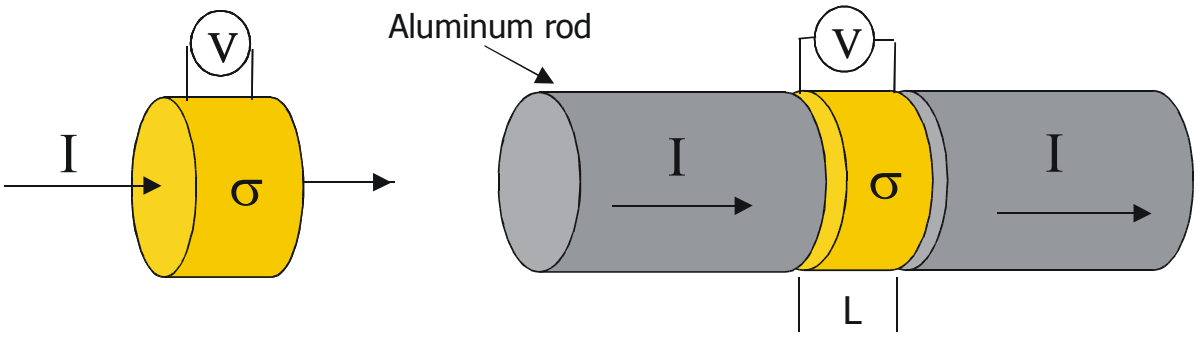

Figure 3.8: **Model development for controlled green-state samples. The compacts receive the current excitation either through point contact copper electrodes (left), or blocks of aluminum rods covering the entire surface of the sample (right).**

3.2.3. Numerical predictions

Given a measurement setup with a current source driving the current through the cylindrical sample, the above derivation (3.28) in conjunction with (3.17) enables us to calculate and plot the magnitude of the total current density and the associated relative voltage distribution throughout the axis-symmetric interior of the compact, as shown in Figure 3.9 and Figure 3.10 respectively. The current injection is accomplished through a single point electrode applied normal to the surface and acting along the center of the cylinder on either face of the cylinder. Clearly observable in both figures is the non-uniform field behavior, exhibiting a source region of maximum strength at the left hand side, and a sink region of minimum strength at the right hand

side of the cylinder. The current spreads out from the source and sink point, generating highly non-linear effects.

Of particular interest, however, is the voltage along the surface since this ultimately forms the basis of the model comparison with measurements. It is the measurement of the surface voltages, which ultimately will provide the information about the internal structure of the analyzed compact. The functional behavior of the surface voltage along the length of the cylinder is non-linear as seen in Figure 3.11 for a cylinder with a 1-to-6 diameter-to-length (D/L) ratio. The voltage has been normalized against the highest voltage that occurs in the cylinder. This allows eliminating the magnitude of the injected current and the conductivity of the cylinder material, leaving only the non-linear effects of the spreading of the current from the source points on the surface voltages.

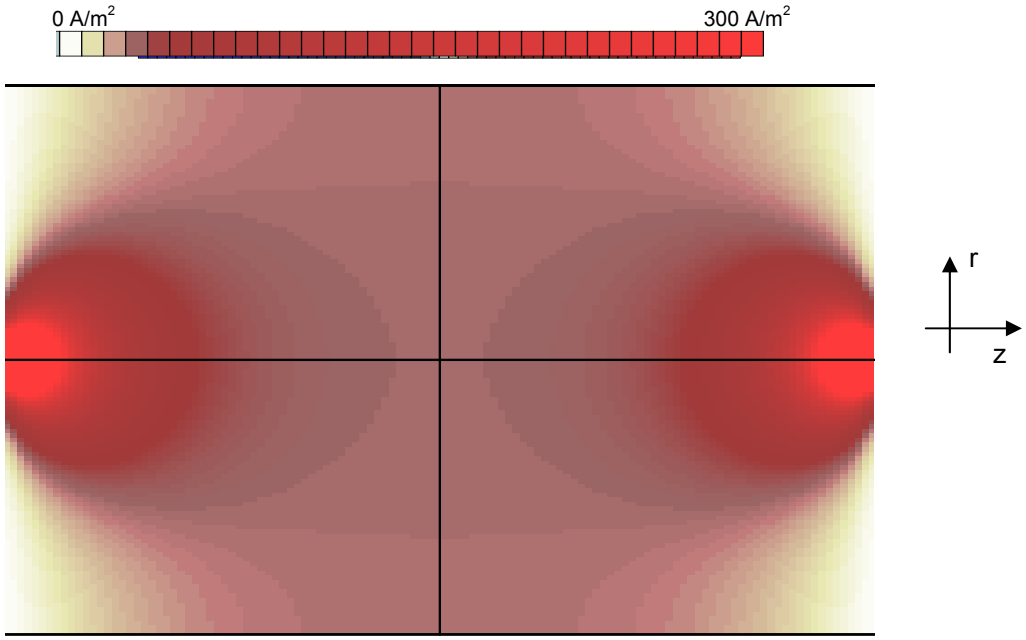

Figure 3.9: Current density for a cylindrical compact with a length of 3 cm and a diameter of 2 cm when excited by a point current source of 1A.

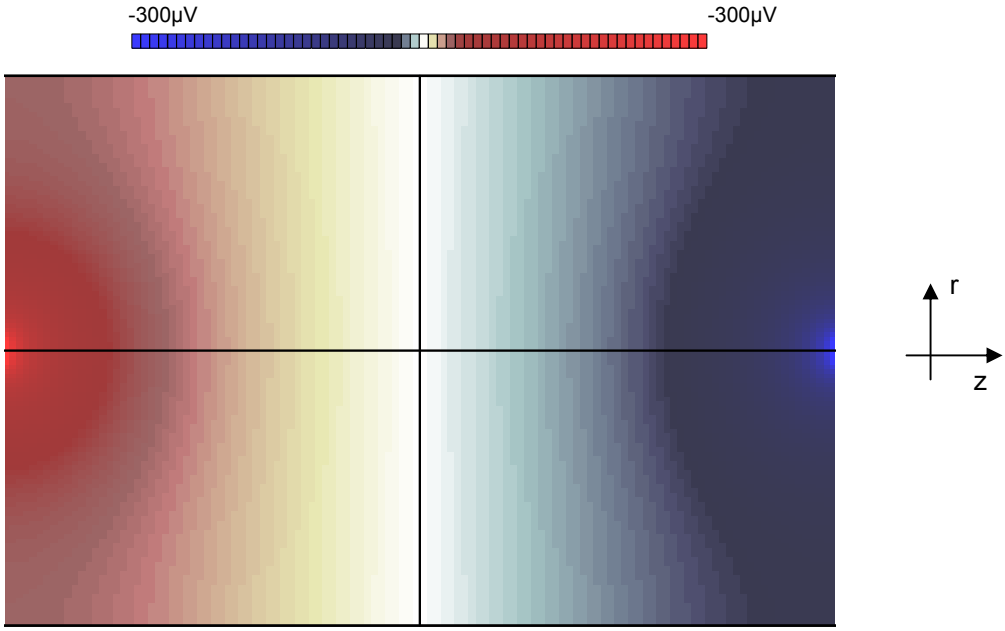

Figure 3.10: **Voltage distribution for a cylindrical compact with a length of 3 cm and a diameter of 2 cm when excited by a point current source of 1A.**

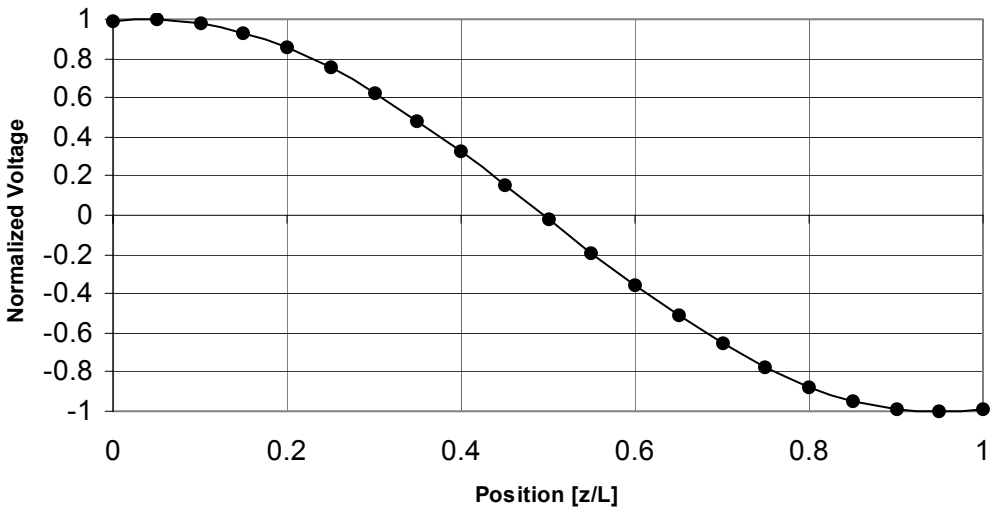

Figure 3.11: **Predicted normalized surface voltage for a measurement setup as the model shown in Figure 3.8,left, with a diameter-to-length ratio of 1:6.**

Based on the Green's function model, Equation (3.28), voltage predictions can be made for various diameter-to-length (D/L) aspect ratios. Specifically, Figure 3.12 provides voltage distributions along the outer surface of the sample as a function of the ratio of the diameter and the length of the cylinder, *D/L*. As expected, for small *D/L* ratios, where the current flows uniformly through most of the part, the voltage distribution follows almost a linear, lumped element distribution as predicted by Ohm's law, Equation (3.37). However, as the ratio becomes larger, the electric field begins to show a flow pattern with more gradual voltage gradients seen in the corners, which is reflected in the increasingly non-linear behavior of the surface voltage measurements.

A different voltage prediction is obtained by plotting the radial voltage drop from the positive current injection point in the center of the cylinder face to the outside perimeter R of the upper cylinder surface. Figure 3.13 depicts the voltage distribution as a function of *D/L* ratios recorded along the radial direction for the left hand end surface, the face with the positive current injection. We notice the rapid drop in magnitude along the radial direction as the (D/L) ratio increases.

The practical implications of these simulations are such that long samples approach a one-dimensional behavior that can suitably be described by Ohm's law. For samples with a large aspect ratio D/L, however, the non-linear effects can no longer be neglected.

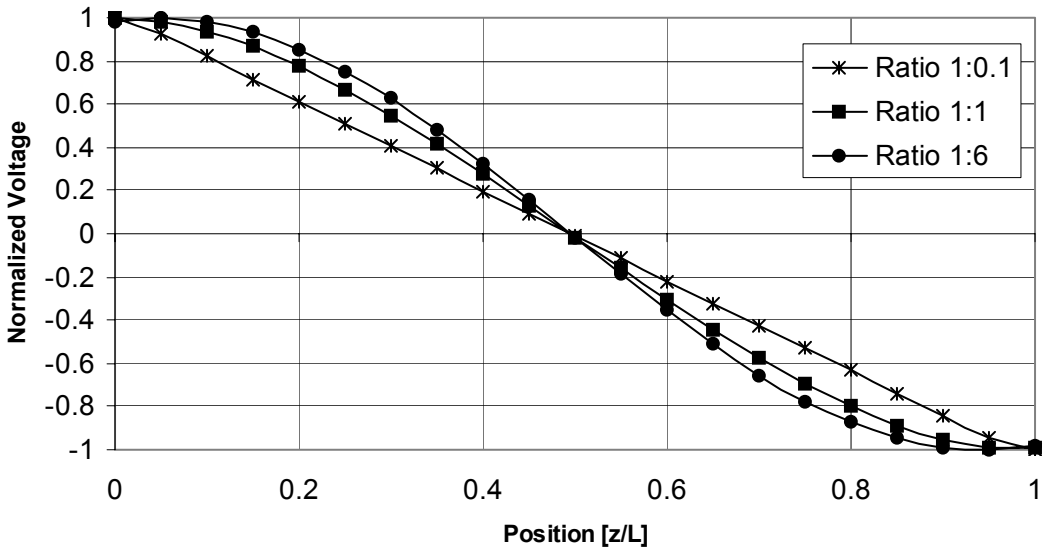

Figure 3.12: Voltage distribution along the outside surface of the cylinder (normalized values) as a function of various D/L ratios.

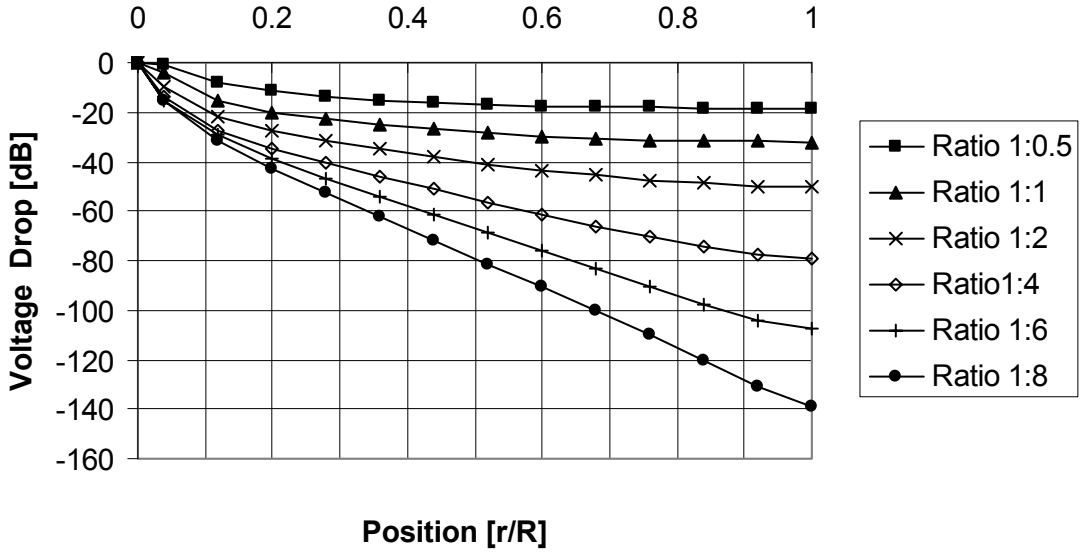

Figure 3.13: Theoretical voltage predictions on the face of a cylindrical sample as measured from the center outwards. Calculations are shown for various D/L ratios.

3.2.4. Comparison with Measurements

Finally, to test the analytical model against measurements, a generic test arrangement was configured as illustrated in Figure 3.14.

The controlled current source is capable of producing currents up to 2.5 A, where the current could be fine adjusted to be within 0.5% of its nominal setting. An HP3478A precision bench voltmeter with microvolt resolution and 0.0015% error was employed to record the voltages on the cylinder surface. Comparing the voltage predictions with measurements, a green-state cylinder of pure iron compacted to 6.5 g/cm^3 and with dimensions of D = 1.5 cm and L = 6 cm is chosen and subjected to a constant current of I = 1 A supplied through point electrodes on the left and right cylinder face surfaces. Steel nails with a flat contact area of 0.25 mm^2, which is negligible compared to the face surface area, approximated the point sources. The measurement arrangement with separated current and voltage probes effectively eliminated any errors due to contact resistances (see Section 2.2.5 for a more detailed discussion).

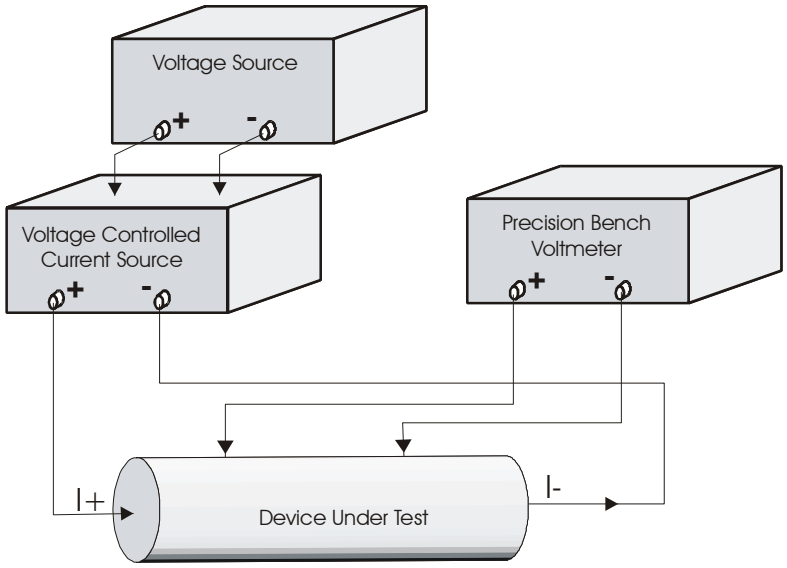

Figure 3.14: Schematic block diagram of the measurement arrangement.

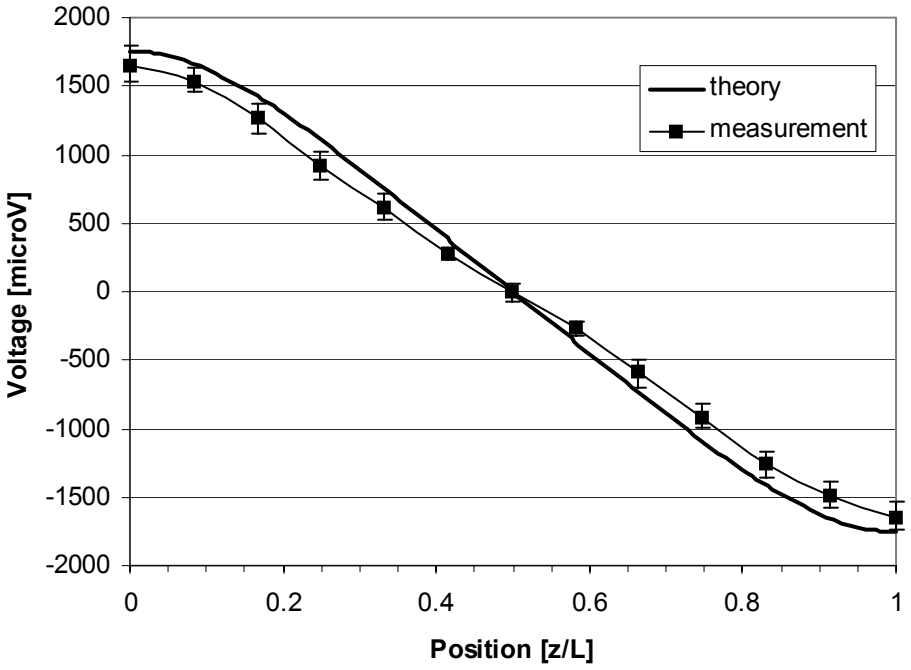

Figure 3.15: Comparison between theoretical voltage predictions and measurements along the surface of a long, thin cylindrical sample of L = 6 cm and D = 1.5 cm.

Figure 3.15 compares actual voltage measurements with scaled theoretical predictions along the entire length of the sample. The results track very closely and sufficiently confirm the results of the theoretical predictions. The differences encountered between predictions and actual measurement mainly stem from the composition of the measured cylinder. Since the cylinder was compacted from metal powder, it can not be regarded as completely uniform over its whole length. Small differences in material properties may lead changes in the measured voltage distribution.

Voltages recorded in radial direction on the top or bottom surfaces drop off very quickly, as demonstrated in the theoretical results shown in Figure 3.13, rendering experimental voltage measurements impractical and thus preventing a reliable experimental verification.

4 Conductivity-Density Relationship

The conductivity-density relationship for green-state P/M parts lies at the core of our proposed approach to measure density distribution in such compacts. Since we are actually measuring conductivity variations and establishing a conductivity profile of the part, we need to be able to relate the measured conductivities to a green-state density.

Intuitively we expect the compaction density of a part consisting of metal powders to be related to its conductivity. Since the literature does not reveal any prior research in this area, the first step in our approach to detect density variations through conductivity measurements was to establish this conductivity-density relationship. A series of measurements was conducted and followed up by theoretical considerations. The following section provides the results of these investigations.

4.1. Measurements on Green P/M Samples

4.1.1. Measured Parts

Controlled cylindrical green state compacts have been manufactured specifically for the purpose of conductivity measurements. The cylindrical shape with a large diameter to length ratio of 4:1 (diameter D = 6cm, length L = 1.5 cm) was chosen for several reasons:

1. The simple cylindrical geometry allows mathematical modeling, and permits a simple measurement setup.
2. The disc like shape with its short compacted length would assure a uniform density distribution within the green-state compacts.
3. The large diameter/length ratio would force the current to flow through the inside of the part rather than on the surface only.

Figure 4.1: Controlled green-state P/M compacts used for the conductivity measurements.

In a first step the base material for these samples, shown in Figure 4.1, consists of pure iron powder (1000B) and the nominal compaction densities range from 6.0g/cm^3 to 7.4g/cm^3. Each specimen density was replicated three times to take into account possible process variations. Additionally, the parts were divided into four sets, which differed in the amount of lubricant in the powder mixture in order to examine the effect of these lubricants on the conductivity versus density relationship. Tight specifications imposed on the manufacturing process of the P/M samples should reduce measurement uncertainties. In addition, the influence of the production process can be investigated by having four different manufacturers, each producing a set of identical parts. The green state samples were specified as follows:

- One powder manufacturer produces four batches of iron 1000B; one batch containing no lubricant, the other 3 batches containing 0.3%, 0.5% and 0.75% Acrawax (AWX), respectively. The AWX was bonded to the iron particles for optimal mixing properties.
- Four different parts manufacturers each produced 4 sets of cylindrical parts from the same powder (specified above) with the following features:
    - Length/diameter ratio of approximately 1:4
    - One set of parts for each powder mixture, each set starting at a nominal density of 6.6g/cm^3, and increments of 0.2g/cm^3 up to the maximally achievable density
    - Three parts for each density to minimize the effect of factory tolerances
    - Use of automatic feeders whenever possible to ensure uniformity of parts

- Additionally, a fifth manufacturer produced parts starting at 6.0g/cm^3 in order to quantify conductivity effects at the lower density scale.

The prepared samples should provide a high degree of reproducibility. Moreover, the bonding of the AWX to the iron particles should prevent lumps of lubricants within the parts, thereby minimizing inhomogeneities. The large amount of samples (approximately 280 parts), prepared by 5 different manufacturers in 5 different production environments and on different machinery should yield sufficient data to draw conclusions on the conductivity versus density relationship on a sound basis. Such an approach will assist us to ascertain the dependency of electric properties on manufacturing influences.

After evaluating the results and establishing a relationship for the above mentioned powder mixtures, the effects of other constituents was to be investigated. The detailed study of the 1000B iron with AWX lubricant raised questions about the qualitative effects of additional alloying or lubricating constituents in the powder mixture. Although we would not be able to test all possible combinations of base materials and lubricants, the decision was made to extend the investigations to some additional mixtures. These mixtures were chosen with the goal to answer as many questions as possible without increasing the number of experiments into unmanageable proportions. The green-state compacts for these additional tests were made from the following mixtures:

- 1000B iron powder with zinc stereate (ZnSt) lubricant, to test the effect of a lubricant with larger particle size.
- A series of mixtures from 1000B iron with 0.5% AWX and varying graphite content to test the influence of different amounts of a conductive lubricant. Six sets of parts were pressed with the graphite content varying from 0% to 0.8% in 0.2% increments.
- A complex alloy made from FN-0405 (Ancorsteel 1000B + 3.5% Ni + 0.6% graphite + 0.75% P-11 lubricant + ANCORBOND) which shed light on the effects occurring in parts manufactured from complex mixtures. This powder mixture is used regularly for industry production.

4.1.2. Setup

The large number of samples required a rather sophisticated measurement setup. However, the basic measurement concept was very simple: a uniform direct current is injected into the part through a contact covering the entire surface as shown in Figure 4.2. The resulting homoge-

neous current flow produces a surface voltage difference *V*, which can be directly related to the conductivity σ of the part through the equation

$$V = I \frac{L}{\sigma A} \tag{4.1}$$

where *L* represents the length over which the voltage is measured, *I* is the current strength, and *A* represents the surface area of the part.

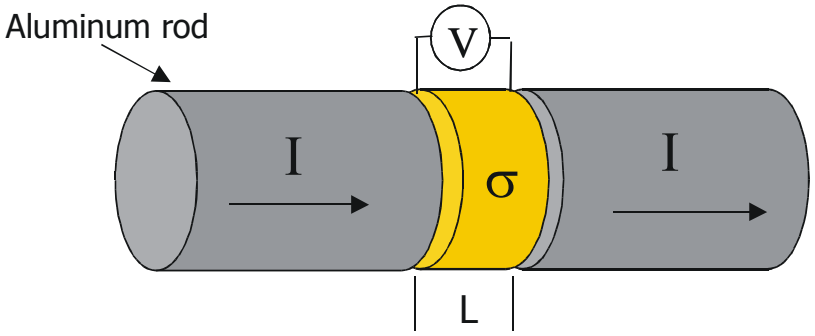

Figure 4.2: Current excitation and voltage measurement for controlled green-state samples. The compacts receive the current excitation blocks of aluminum rods covering the entire surface of the sample.

A semi-automated testing arrangement was developed to accommodate the large number of samples as well as to ensure measurement reproducibility. The parts were contacted through electrodes mounted on a computer-operated bench press, shown in Figure 4.3, which guaranteed constant contact pressure and repeatable geometric positioning. A conductive, meshed material was used to generate the contact between the aluminum rod electrodes and the part under test. This was used to overcome the problem of contacting an evenly distributed contact between two planes. Any irregularities in the surface planes would be equalized by the meshed material, resulting in a reliable contact.

A voltage controlled electric current source with three different pre-set settings allowed the injection of currents of 1A, 2A and 2.5A. This voltage controlled current source, the schematic of which is shown in Figure 4.4, was developed specifically for these measurements and allows the setting of a DC current in the range between 0 and 2.5A. The preset current strengths can be selected by a switch for easy access. Higher current strengths are possible with minor modifications.

Figure 4.3: **Semi-automated measurement setup for extended conductivity measurements.**

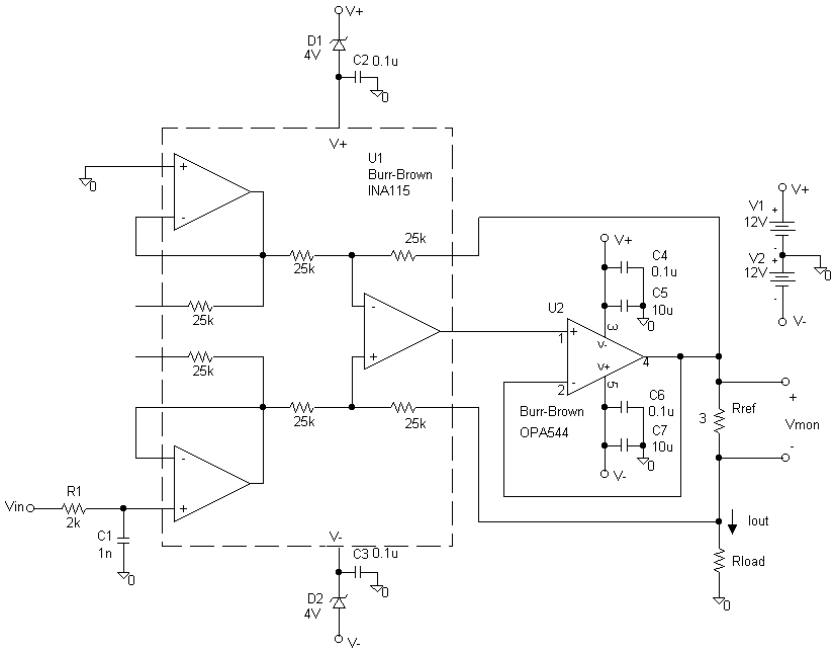

Figure 4.4: **Schematic for voltage controlled current source used to conductivity measurements.**

4.1.3. Sensors

The voltage sensing is, in theory, straightforward. A simple two pin sensor with a fixed distance between the measuring points will record an identical voltage, wherever it is placed on the circumference of the green-state compact, as long as it stays aligned with the direction of the current flow. Such a sensor is depicted in Figure 4.5. Furthermore, this simple configuration provides a four probe measurement setup with the advantage of the removal of the probe contact resistances from the measurement results, as discussed previously in section 2.2.5. And since the current density throughout the volume as well as the conductivity of the sample is assumed uniform, the voltage drop over a certain length is expected to be constant too without any dependence on the positioning of the sensor.

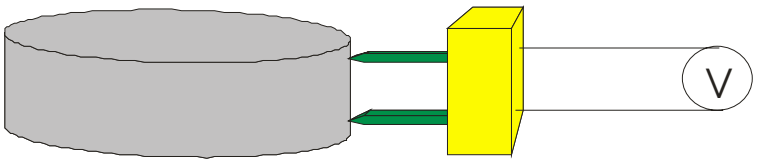

Figure 4.5: Regular two-pin voltage sensor with fixed contact distance.

However, during the measurements it was discovered that changing the position of the two pin sensor could change the measurement result considerably. The reasons for this phenomenon are not quite clear, although several possible causes come to mind. First, it is possible that the mixing process did not produce a completely balanced mixture, so that some areas in the part receive a higher percentage of lubricant than others. Also lubricant particles could clot together, again forming regions of higher lubricant concentration. A second possibility is the migration of lubricant particles toward the part surface during the compaction process. It is well known that some lubricant migration occurs and that could again lead to an uneven distribution of the non-conducting lubricant particles. A third possibility is the influence of differences in the surface itself. The green-state P/M parts have a shiny, smooth surface that looks like solid metal. Inside the compacts clearly exhibit the grainy structure of pressed powder. These structural differences between the immediate surface area and the bulk material may influence the conductivity. All these reasons would lead to a non-uniform conductivity distribution and as a result, make the voltage measurement dependent on the exact positioning of the two-pin sensor.

In order to overcome the limitations of the two-pin senor, additional sensor configurations and their applicability have been explored. These sensors were specifically developed to investigate the effects of surface conductivity, geometrical averaging or lubricant migration. One sensor

used the identical concept for current injection as described above, the voltage sensing, however, relied on two ring bands, which contacted the green state compact along the entire circumference, as depicted in Figure 4.6. The effect of this scheme is an averaging of the voltage between any two points on these rings. This eliminated the dependency of the recorded voltage on the geometrical positioning of the two-pin sensor and improved measurement repeatability considerably. Another sensor employed an isolated center pin within the aluminum rod for the voltage sensing, as shown in Figure 4.7. The current was injected through the outer ring, which still contacted almost the entire surface for current injection, and the resulting voltage was measured from top to bottom of the contacted part between these isolated center pins. As it turned out, this arrangement allowed for the highest reciprocity, since the contact placement and the contact pressure were assured to be identical for each measurement. Also the top and bottom surfaces seem to exhibit less variation regarding lubricant migration. Although the current density can no longer be regarded as completely uniform within the volume when using this current injection scheme, the effect of the isolated section in the center can be neglected and equation (4.1) still holds with good approximation. It was this sensor that was used subsequently to generate the results below.

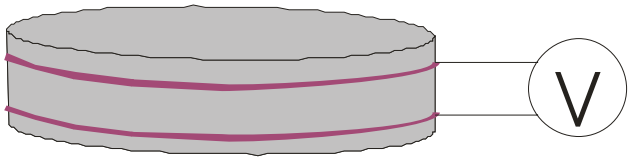

Figure 4.6: Voltage sensing around circumference of cylindrical part.

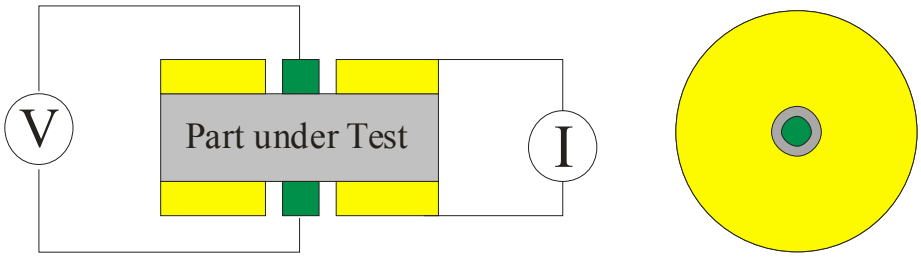

Figure 4.7: Sensor with isolated center pin for voltage sensing and ring electrodes for current injection (cross-sectional view left, top view right).

4.1.4. Results

Figure 4.8 shows the conductivity as a function of density for pure iron compacts made from 100B iron powder. The measurement points shown in the graph are generated as a result of averaging the numerical values over 3 different current strengths and over three samples with the same nominal density. From these measurements it can be concluded that density versus conductivity follows a linear correlation over the given density range. This linear relationship was found to be consistent for parts produced by all manufacturers and measured with all of the above-mentioned sensors. However, the absolute values of conductivity found in the different batches differ somewhat. Differences in the powder handling procedures may be the cause of that effect, altering the base conductivity of the powder. The graph is therefore given for the non-lubricated parts of one batch only, while the basic behavior is the same for the parts from all four batches.

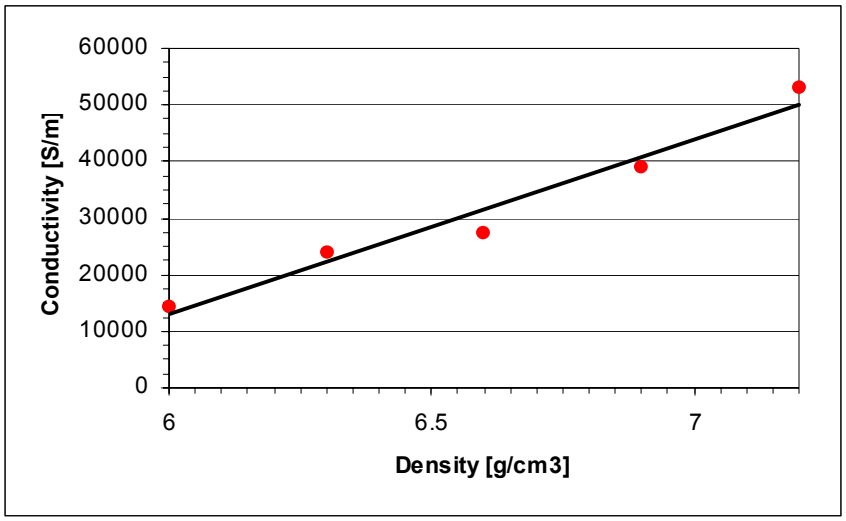

Figure 4.8: Conductivity versus density for measured green state P/M samples from 1000B iron powder without lubricants added.

While the recordings for pure iron powder yielded the expected results, the measurements of parts from iron/lubricant mixtures resulted in a surprising outcome. First parts from 1000B iron powder with various amounts of Acrawax (AWX) lubricant were analyzed. As shown in Figure 4.9, the conductivity in this case exhibits a more complicated behavior, which can best be approximated by a parabolic function. Contrary to the non-lubricated case, we find a maximum in conductivity for a density of approximately 6.8 g/cm^3. If the density is increased beyond this point, the conductivity begins to decrease. Furthermore it is interesting to note that the amount

and type of lubricants in the green-state samples significantly influence the density versus conductivity correlation [41, 42].

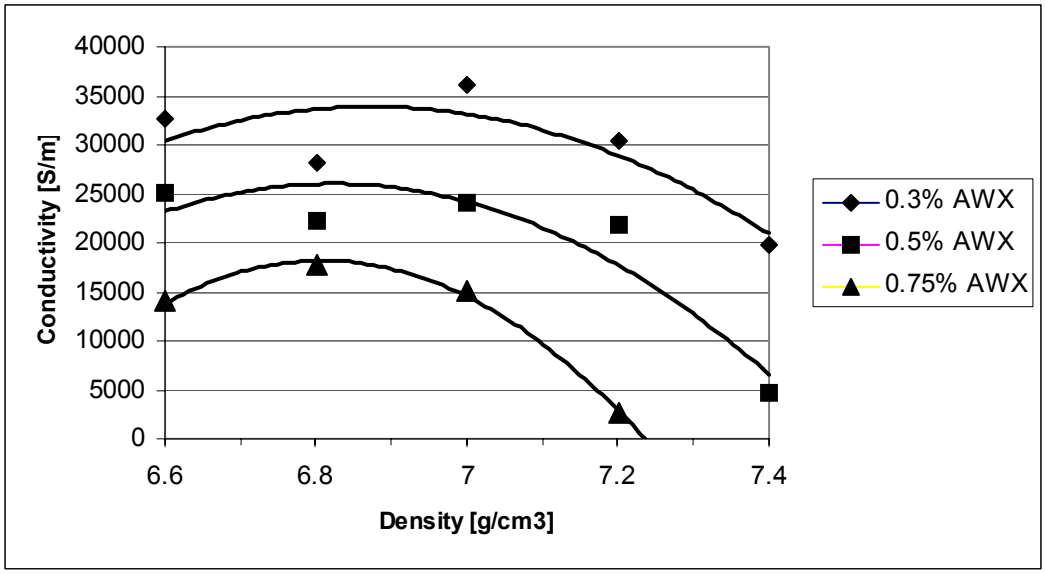

Figure 4.9: Comparison between the conductivity of green-state samples from 1000B iron with different amounts of lubricant (AWX).

This non-linear relationship was observed in all the measured lubricated samples from all P/M part manufacturers. It was consistent over all measurements of samples from 1000B iron with AWX lubricant. An additional batch of parts was tested in order to determine the influence of the type of lubricant added to the iron powder. A new batch of parts was manufactured from 1000B iron under identical conditions, except that ZnSt was used as lubricant. As a result of this investigation it was found that the inversion behavior at high densities is present in this mixture too and that the correlation between density and conductivity not only depends on the presence and the amount, but also on the type of lubricant used. In Figure 4.10 the influence of 0.75% Acrawax versus 0.75% ZnSt on the conductivity-density relationship is depicted. While the amount and type of lubricant change the absolute conductivity level and conductivity/density gradient, the curves for both sets of compacts exhibit a conductivity maximum at approximately 6.8g/cm^3 and show the same basic inversion behavior at high densities.

Additional powder mixtures were tested to evaluate the influence of additional powder constituents. Figure 4.11shows the conductivity for green P/M compacts made from FN-0405 powder. This ANCORBOND mixture, where the particles of the different materials are bonded to the bulk iron particles for optimal mixing properties, consists of the following ingredients:

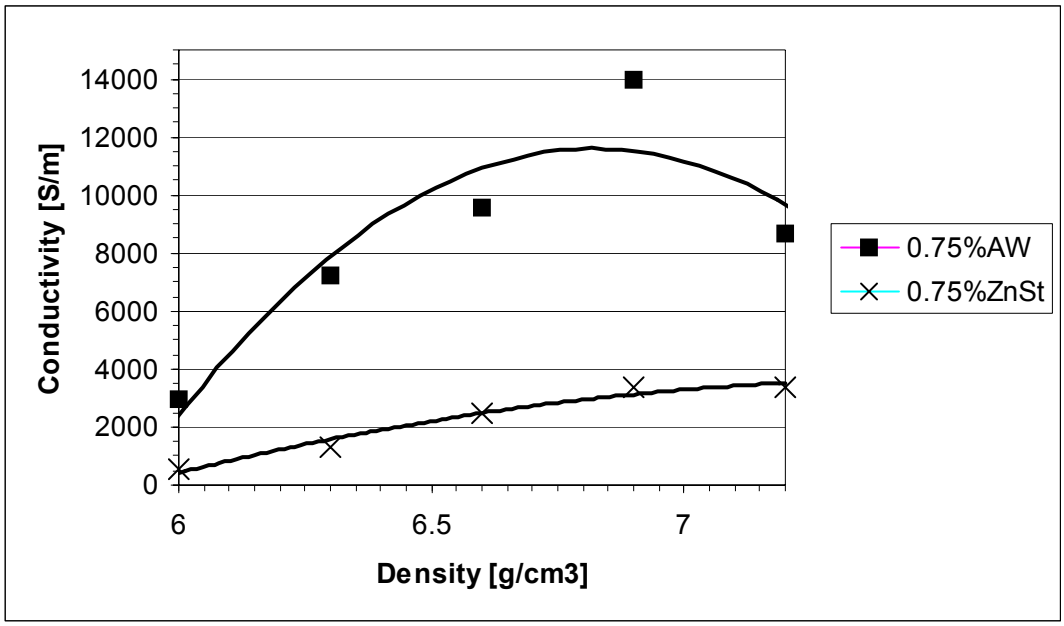

Figure 4.10: **Comparison between the conductivity of green-state samples from 1000B iron with different types of lubricants (AWX and ZnSt).**

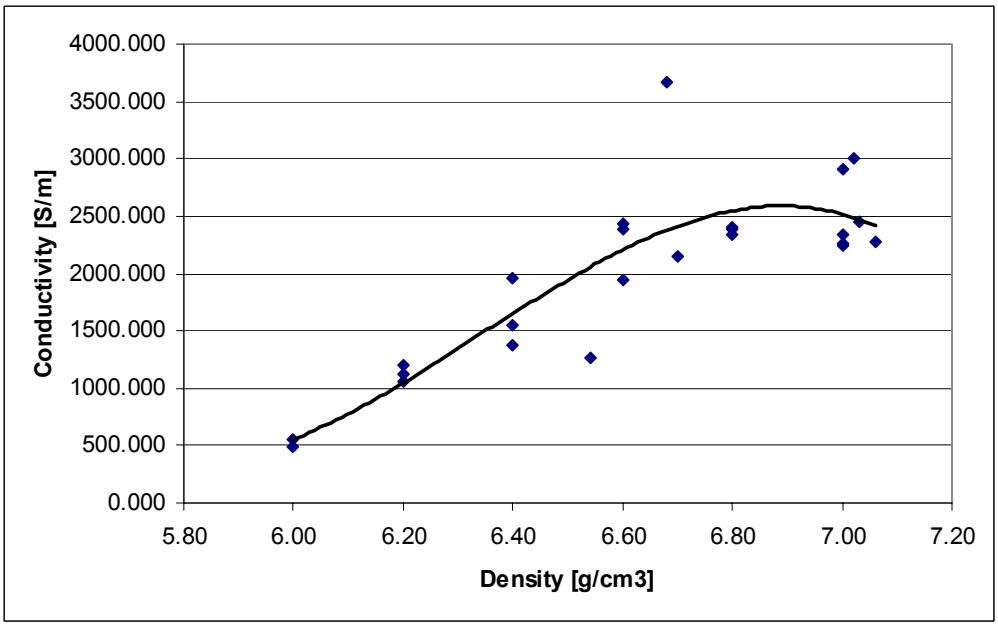

Figure 4.11: **Conductivity versus density for a FN-0405 (Ancorsteel 1000B + 3.5% Ni + 0.6% graphite + 0.75% P-11 lubricant + ANCORBOND) powder.**

- Ancorsteel 1000B
- 3.5% Ni
- 0.6% graphite
- 0.75% P-11 lubricant

In measuring this mixture, the influence of various changes to the originally inspected material could be observed. The results show the influence of an additional alloying metallic component, of added graphite and of a different type of non-conducting lubricant, the P11. As can be observed in resulting graph in Figure 4.11, the conductivity-density behavior is still the same as for all other lubricated powder mixtures.

In an additional test series the influence of a conductive lubricant like graphite was to be investigated. The goal was to test whether the addition of a somewhat conductive lubricant would significantly change the conductivity-density relation, specifically to test for the occurrence of an inversion point. For that purpose a series of green-state compacts was manufactured from 1000B iron powder with 0.5% AWX and additional graphite content ranging from 0% to 0.8% in 0.2% increments. The results of these measurements are visualized in Figure 4.12 and Figure 4.13. For all mixtures we can clearly see the inversion in the least square fitted trend lines. Although it is not intuitive to deduct a clear correlation between the graphite content and the conductivity of the sample, we can clearly see that the qualitative behavior is not significantly altered by the increasing graphite content. Hence we can conclude that the presence of graphite does not change the behavior and that the observations, which were made earlier for lubricated compacts, are valid for these samples too.

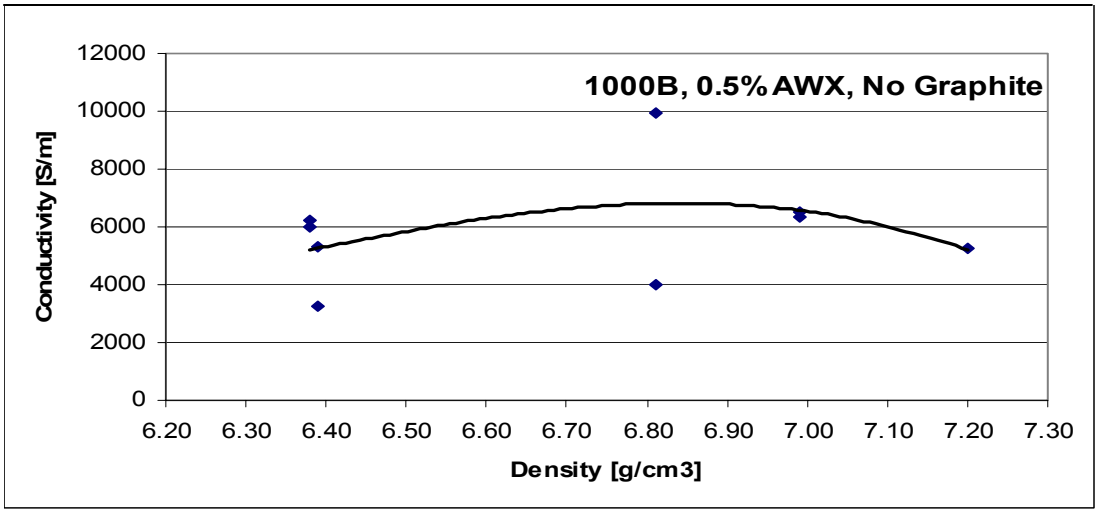

Figure 4.12: Conductivity versus density for green-state compacts from 1000B iron with 0.5%AWX. There was no graphite added in this series.

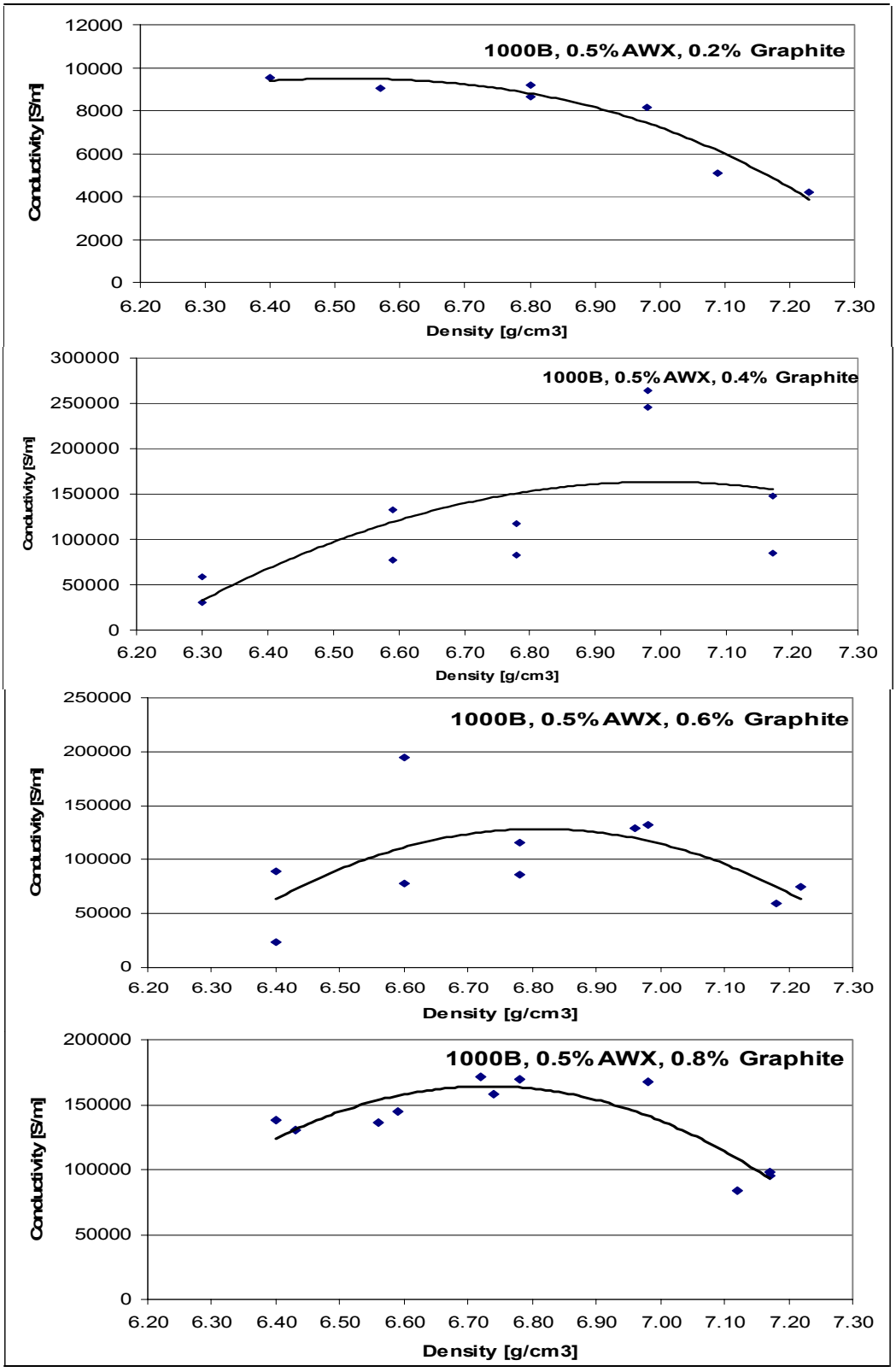

Figure 4.13: Conductivity versus density for green-state compacts from 1000B iron with 0.5%AWX and varying amounts of graphite.

4.2. Conductivity of Mixtures

4.2.1. Non-Conducting Particles in Conducting Medium

There are many reasons why the apparent averaged conductivity in P/M components containing lubricants may decrease with increasing density (as seen for example in Figure 4.9). Some of these are:

- Lamination effects
- Lubricant migration
- Increased corrosion

However, none of the above does sufficiently explain the observed results.

The one phenomenon in lubricant containing P/M compacts that has the potential to cause a non-linear relationship is the redistribution and geometrical deformation of the lubricant upon compaction, thus affecting the electrostatic response of the compact. This phenomenon and its underlying theory are further elaborated below.

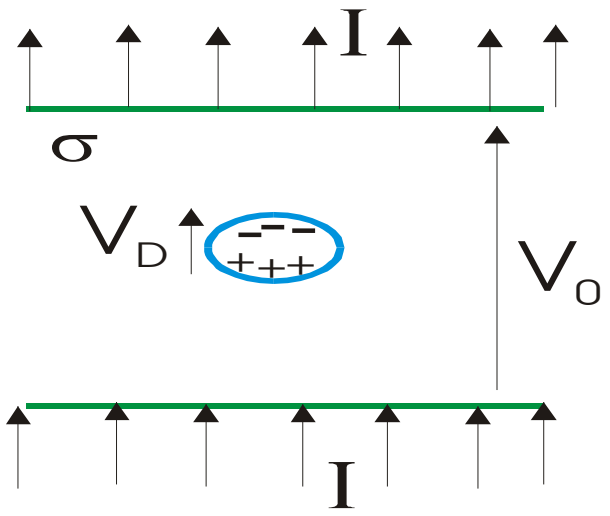

Figure 4.14: Single lubricant particle with induced charges in homogeneous background conductivity.

Let us consider a single, non-conducting lubricant particle within an otherwise homogeneous material of conductivity σ, as depicted in Figure 4.14. The field $\boldsymbol{E_0}$ induced by the current flow in absence of any inhomogeneities is

$$E_0 = \frac{1}{\sigma} J_0 . \tag{4.2}$$

The non-conducting lubricant particle can be regarded as a depolarizing dipole, whose field is generated by surface charges induced by the impressed current density ***J***. The surface charges on the non-conducting particle orient themselves in such a way that they annihilate the local field at the particle boundaries. As a result, the depolarization field is oriented in the same way as the global field $\boldsymbol{E_0}$.This dipole field contributes to the voltage measured at the outside of the part so that the outside voltage becomes

$$V = V_0 + V_D . \tag{4.3}$$

If we next contemplate the situation as depicted in Figure 4.15, where a powder/lubricant mixture is shown at two different compaction states, we deduce an increase of lubricant particles within a given volume at high densities. Since each of these particles generates a dipole field, we have to conclude that the total induced voltage $\boldsymbol{V_D}$, which is the sum of the dipole voltages over all lubricant particles, increases at the circumference of the part. Keeping the impressed current ***I*** constant, this results in an increase of the measured resistance as seen in (4.4):

$$R = \frac{V}{I} = \frac{V_0 + V_D}{I} = \frac{L}{\sigma A} \tag{4.4}$$

where V_0 is the voltage due to the background conductivity $\boldsymbol{\sigma_0}$ and $\boldsymbol{V_D}$ is the sum of the dipole potentials.

These results allow us to model the conductivity-density relationship of a non-lubricated part by a linear equation as given in (4.5)

$$\sigma = \sigma_0 (1 + \alpha_1 \rho) , \tag{4.5}$$

where $\boldsymbol{\sigma_0}$ refers to the background conductivity and $\boldsymbol{\alpha_1}$ is a constant model parameter.

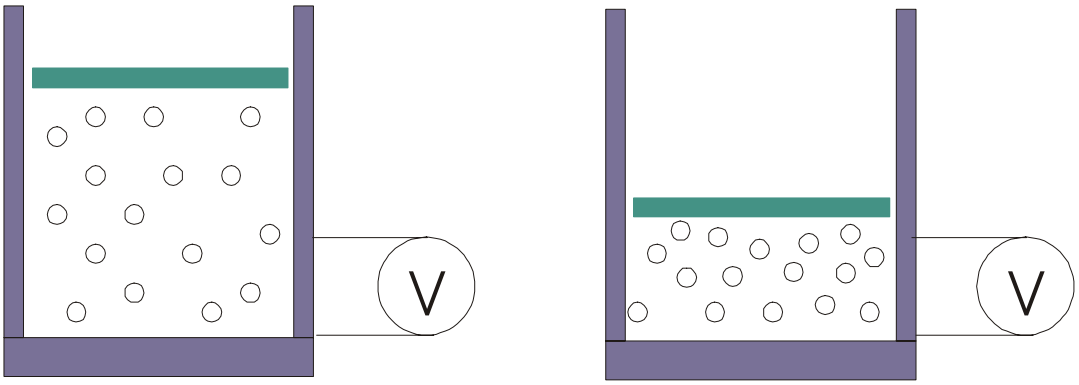

Figure 4.15: Lubricant particles in a green state P/M part at two different compaction densities, illustrating the increase in lubricant particle count per volume with increased density.

If we now take lubricated parts into account, we have to expand the initial equation so that it becomes a quadratic equation as in (4.6), where the first part is identical to the non-lubricated situation, and the second term models the inversion behavior. The factor α_2 again refers to part attributes such as lubricant concentration, type of lubricant, particle size, etc.

$$\sigma = \sigma_0(1+\alpha_1\rho)(1-\alpha_2(V_D)\rho) \tag{4.6}$$

Although Equation (4.6) with its quadratic nature allows approximating the parabolic nature of the conductivity – density dependency found in lubricated P/M compacts, it only provides a mathematical tool and does not explain the physical reasons.

When considering the conductivity of green-state P/M parts, we have to deal with the theory of the conductivity of mixtures. Here the metal powders, which is the main constituent of the mixture, presents the conducting medium, the lubricant particles and air bubbles are considered non-conducting. Although numerous researchers have investigated the conductivity of binary mixtures [48, 65], none of the existing theories can explain the electric behavior encountered in green-state P/M parts.

The problem of determining the electrical conductivity and the dielectric constants are closely related. Both cases result in almost identical Laplace-type equations, where an electric potential must be continuous across the interface of adjacent regions with different material parameters. The required boundary condition arises from the continuity of the electrical current density,

$$J = \sigma E\,, \tag{4.7}$$

perpendicular to the interface in the conductive case. Here σ denotes the electric conductivity and $\mathbf{E}$ is the electric field. Furthermore, the continuity of the displacement,

$$D = \varepsilon E \tag{4.8}$$

perpendicular to the interface must be maintained (ε represents the dielectric constant). Since the field **E** plays the same role in both cases, the governing equations for the conductivity and the dielectric constant become identical.

If the non-conducting particles in a conducting medium are treated like molecules in a solid or liquid dielectric spaced in such a way that we can assume that the effect of their presence does not considerably alter the electric field acting on the neighboring particles, then the Clausius-Mossotti equation applies:

$$\varepsilon E_{eff} - \varepsilon_0 E_0 = \frac{4\pi}{3}\varepsilon P = \frac{4\pi}{3} nLE_{eff} \tag{4.9}$$

This equation calculates the summed effect of all particles within the volume due to the external electric field E_0, resulting in an effective field E_{eff}. Here P is the macroscopic polarization vector, n is the particle concentration, and L represents the depolarization factor. Such a model appears to be a plausible explanation, as the lubricant can be considered as individual particles embedded in the green-state P/M base material. Since the lubricant concentration is generally low, on the order of 5% or less, the mutual interaction between the polarizable particles can be neglected. The sum of their effects, however, still leads to an effective field that differs from the applied field.

The idea of having two separate material constituents with different electric properties can also be treated from a purely mechanical point of view. Considering a medium consisting of two (or more) constituents with conductivities σ_1 and σ_2 and volume fractions f_1 and f_2 on a completely symmetrical basis, leads to Bruggeman's symmetric theory [11, 21]. This theory allows us to calculate the conductivity of a random mixture of spherical particles of two constituents, both of which completely fill the medium as depicted in Figure 4.16. Generalizing the equation to three dimensions *d*=1,2,3, the conductivity of medium σ_m is thus given by the equation [51, 54]

$$f_1 \frac{(\sigma_1 - \sigma_m)}{(\sigma_1 + (d-1)\sigma_m)} + f_2 \frac{(\sigma_2 - \sigma_m)}{(\sigma 2 + (d-1)\sigma_m)} = 0\,. \tag{4.10}$$

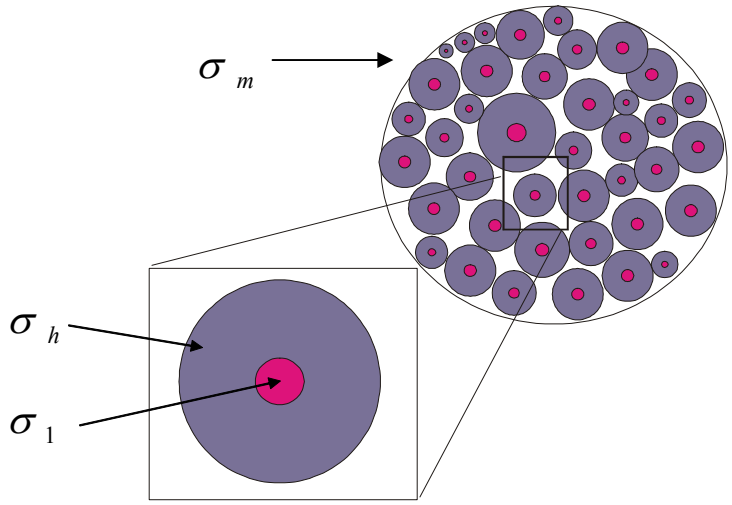

Figure 4.16: Schematic representation of a symmetric mixture in the Bruggeman sense, where one constituent is at all times completely surrounded by the other.

For the case of a non-conducting dispersive material ($\sigma_1 = 0$) in a highly conductive host medium with $\sigma_2 = \sigma_h$, Equation (4.10) is solved for the conductivity of the resulting mixture as

$$\sigma_m = \sigma_h \left(1 - \frac{fd}{d-1}\right) = \sigma_h \left(1 - \frac{f}{f_c}\right) \tag{4.11}$$

Here f_c denotes the critical insulator volume fraction at which the conductor - insulator transition occurs. In three dimensions f_c becomes 2/3 [52].

The volume fraction of each constituent can easily be calculated from the known densities of the two constituents and the mixture. Using

$$g = V\rho \tag{4.12}$$

(with V being the volume and ρ the specific weight), we can calculate the contribution of each part to the weight of the mixture. Setting the weights into relation to each other, the volume fractions of either constituent can be determined as

$$f_1 = \frac{V_1}{V_{mix}} = \frac{\rho_2 - \rho_{mix}}{\rho_2 - \rho_1}. \tag{4.13}$$

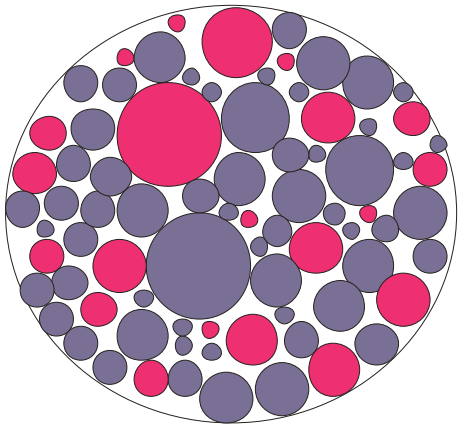

Figure 4.17: Schematic representation of an asymmetric mixture in the Bruggeman sense, where the two constituents completely fill the media with spherical particles of all sizes.

The conductivity of a medium can be calculated using Bruggeman's asymmetric theory, where the dispersion with conductivity σ_1 consists of an effectively infinite size range of spheres, each of which remains coated at all volume fractions with the host medium of conductivity σ_m [12, 39]. A schematic representation of such a mixture is shown in Figure 4.17. Using the more general approach of oriented ellipsoids instead of spheres, the equation for the conductivity of this mixture can be written as [52]

$$\frac{\left(\sigma_m - \sigma_d\right)^{1/L}}{\sigma_m} = \frac{\left(1-f\right)^{1/L}\left(\sigma_m - \sigma_h\right)^{1/L}}{\sigma_h}, \tag{4.14}$$

Specifically, L denotes the depolarization factor of the ellipsoids with the short axis oriented in the direction of current flow. When the dispersion is regarded as an insulator compared to the conductivity of the host medium ($\sigma_1 = 0$), Equation (4.14) becomes

$$\sigma_m = \sigma_h \left(1 - f\right)^{\frac{1}{1-L}}. \tag{4.15}$$

Combining the two theories into a semi-phenomenological effective medium equation developed by McLachlan [53] results in one equation that allows us to treat media whose morphologies are those of the symmetric and asymmetric media of Bruggeman or lie in between these two extremes. The generalized effective medium equation is therefore given by

$$\frac{f\left(\sigma_1^{\,1/t} - \sigma_m^{\,1/t}\right)}{\sigma_1^{\,1/t} + \frac{f_c}{1-f_c}\,\sigma_m^{\,1/t}} + \frac{\left(1-f_c\right)\left(\sigma_2^{\,1/t} - \sigma_m^{\,1/t}\right)}{\sigma_2^{\,1/t} + \frac{f_c}{1-f_c}\,\sigma_m^{\,1/t}} = 0. \tag{4.16}$$

with $t = f_c/(1-L)$ for oriented ellipsoids and f_c being the volume fraction at which the conductor-insulator transition occurs. Again assuming $\sigma_1 = 0$, we find

$$\sigma_m = \sigma_h \left(1 - \frac{f}{f_c}\right)^t \tag{4.17}$$

for the conductivity of the mixture. Although this equation can be used for any mixture and morphology type, the value for f_c is not readily available. Furthermore we can assume that in our case all the lubricant particles will be surrounded by the metal powder, since the volume fraction of the lubricant is very low. Hence, we may use Bruggeman's equation for asymmetric media as given in (4.15).

Modeling the conductivity of a green state P/M compact was accomplished by calculating the volume fraction of air and lubricant at each density. Employing Equation (4.15), the conductivity for non-lubricated parts was calculated with the conductivity iron as the base material. In a next step, the resulting conductivity was used as the background conductivity in the calculation of the lubricated parts, resulting in an overall equation of

$$\sigma_{PM} = \sigma_{Fe}\left(1 - f_{air}\right)^{\frac{1}{1-L_{air}}}\left(1 - f_{\mathrm{lub}}\right)^{\frac{1}{1-L_{\mathrm{lub}}}}. \tag{4.18}$$

Using these parameters to simulate the conductivity–density relationship over a wide density range does not show the results we obtained during the experiments. Although the volume fractions for the air and the lubricant account for a reduction in the overall conductivity, the functional relationship stays linear. This is explained by the fact that the volume fraction of the

lubricant remains constant through the compaction process. The increased amounts of non-conducting lubricant particles per volume at high densities only result in a lower slope in the still linear relationship and cannot explain the inversion behavior.

4.2.2. Depolarization Effect

In the previous section the lubricant particles and the air inclusions within the pressed part are considered as perfect spheres. As seen above, the linear increase of low-conducting particles per volume with a linear increase in density leads to a linearly increasing conductivity, where the amount of lubricant in the mixture determines the slope of the relationship. While a spherical shape is a valid approximation for the lubricant particles in the non-compacted state, the compaction process deforms the lubricant particles to spheroidal shapes [45]. Unlike the simple increase of lubricant particles per volume at higher densities as seen in Figure 4.15, we now consider the situation as shown in Figure 4.18. Hence, instead of regarding the depolarizing particles as spheres of constant size, we now modify this viewpoint and take into account the geometrical deformation of the lubricant during compaction.

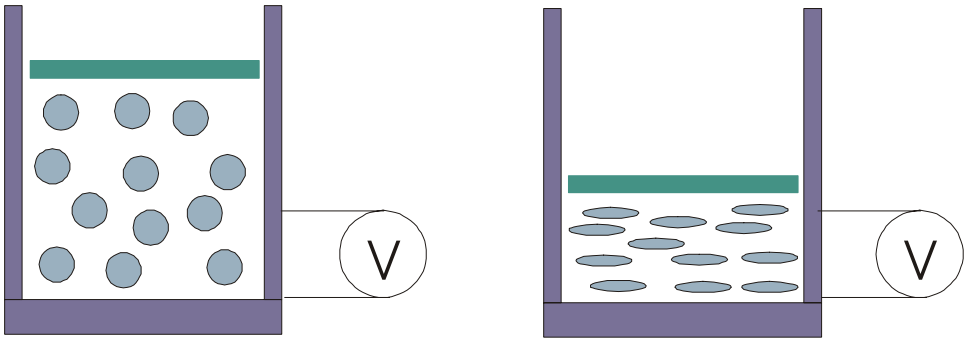

Figure 4.18: Geometrical deformation of lubricant particles with increasing density.

The depolarization factor, which enters equation (4.16), depends on the geometry of the embedded particles. Let us consider an ellipsoidal particle of uniform dielectric properties, which is bounded by a surface defined by

$$f(x,y,z) = \left(\frac{x}{a}\right)^2 + \left(\frac{y}{b}\right)^2 + \left(\frac{z}{c}\right)^2, \tag{4.19}$$

where a, b, and c represent the three half-axes. In the presence of a uniform external field E_0, the interior field is given by the superposition of the external field and the depolarization field E_1,

which is produced by a surface charge. The depolarization potential at any point within the ellipsoid is given by the surface integral

$$\Phi(r') = \frac{1}{4\pi\varepsilon_0} \oint \frac{\mathbf{P}\cdot\mathbf{n}}{|r-r'|} dS\,, \tag{4.20}$$

where $P = \chi_e E_1$ is the polarization of the dielectric and χ_e is the electric susceptibility. Since the depolarization field inside the ellipsoid is uniform [50], we can determine it at any point. The center of the ellipsoid is the obvious point to choose. Here the exterior electric field is given by

$$E_1(r') = E_1(0) = -\frac{1}{4\pi\varepsilon_0} \oint \frac{P\cdot n}{r^3} r dS = -\int\left(\frac{P_x x}{a^2} + \frac{P_y y}{b^2} + \frac{P_z z}{c^2}\right) r d\Omega\,. \tag{4.21}$$

The depolarization factors are usually defined by

$$E_{1i} = -L_i P_i\,, \tag{4.22}$$

where i = x, y, z. Due to the symmetry of the ellipsoid, all the cross terms of xy, xz, and yz do not contribute to the result when integrated over the solid angle [61]. This allows us to separate the variables and calculate the three depolarization factors independently. Rewriting (4.23) in polar coordinates [81], we find the following integral for L_z:

$$L_z = \frac{1}{c^2} \int_0^{2\pi} \partial\varphi \int_0^{2\pi} \sin\vartheta \frac{\cos^2\vartheta}{\frac{\sin^2\vartheta}{a^2}\cos^2\varphi + \frac{\sin^2\vartheta}{b^2}\sin^2\varphi + \frac{\cos^2\vartheta}{c^2}\cos^2\varphi} \partial\vartheta \tag{4.23}$$

In a spheroidal geometry ($a = b \neq c$) this integral can easily be evaluated. If the external field is applied along the z-axis the depolarization factor for the oblate spheroid, where $c < a$, results in

$$L_Z = \frac{4\pi}{e^2}\left(1 - \frac{\sqrt{1-e^2}}{e}\sin^{-1} e\right), \tag{4.24}$$

where $e = \sqrt{1-(c^2/a^2)}$ represents the ellipticity of the rotated ellipse with *c* denoting the short half-axis, and *a* the long half-axis of the oblate spheroid.

As depicted in Figure 4.19, the depolarization factor changes in non-linear fashion. Starting from a perfect sphere with L_z=1/3, a linear change in z direction results in a non-linear change of the depolarization factor and approaches the numerical value of 1 when the extension in z-direction approaches 0.

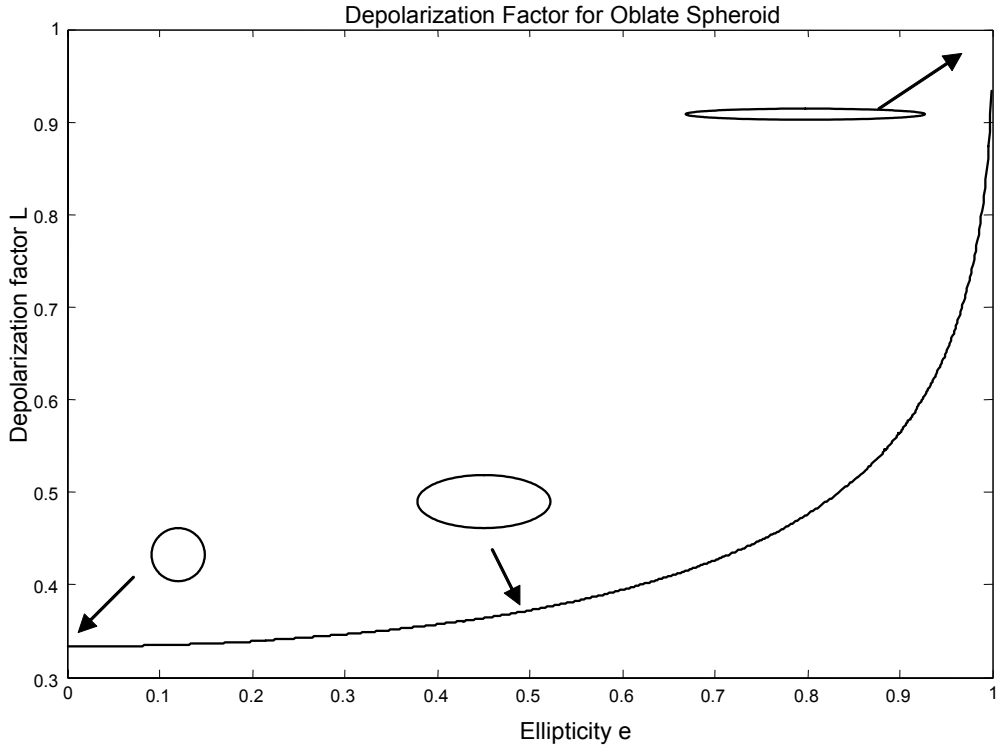

Figure 4.19: Change of depolarization factor of the oblate spheroid with the geometry changing from a sphere to a flat disk. The external field is assumed in the direction of the short half axis of the spheroid.

If we again use Equation (4.18) as the basis for calculating the conductivity of the P/M samples, the depolarization factor no longer remains constant. Increasing the density of the parts will result in a deformation of the lubricant particles. Since the lubricant itself is incompressible and can only change the shape, the volume of each lubricant particle is assumed constant. Furthermore, assuming that the spheroidal properties of the particle are conserved, any compression in z-direction results in a reduction of the short half axis *c* and a corresponding increase of the longer half axis *a*. This enlargement of the cross-section perpendicular to the current flow enhances the non-linear effect of the depolarization factor with increasing density. The sharp increase of this depolarization factor ultimately leads to a highly increased depolarization effect at high densities. Therefore the voltages recorded over a given length, based on injecting a constant

DC current, begin to increase. This, in turn, leads to the experimentally observed decrease in conductivity at high densities.

Figure 4.20 demonstrates the simulation of Equation (4.18) over a large range of nominal densities. We can clearly see the linear behavior for the non-lubricated powder as well as the inversion behavior for the mixtures containing various amounts of lubricants.

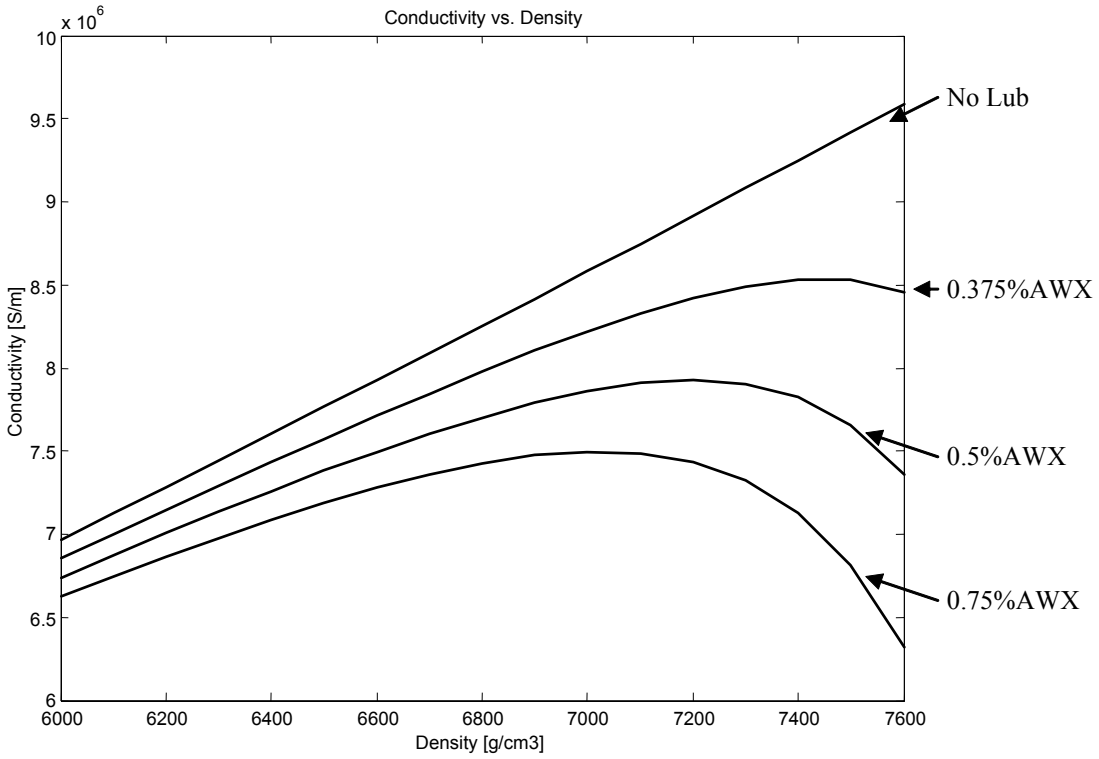

Figure 4.20: Simulation of conductivity vs. density behavior for green state P/M parts with different amount of lubricants.

Although a physical explanation for the qualitative behavior could be found in the above developed theory of the conductivity of green-state P/M parts, it is clear from a direct comparison of the absolute values of the simulated graph to the real measurements that there are still differences. The many parameters that are available to adjust the theory have not yet been further investigated. Some of the effects that have to be taken into account are:

- Base conductivity of 100% dense iron powder is not the same as of pure iron, as assumed in the simulation.

- Grain size is not currently included in the model but definitively impacts both the base conductivity through the contact area between grains and the deformation properties of the mixture.
- Density at which lubricant deformation starts to be effective (after rearranging in the first part of compaction).
- Rate of lubricant deformation.

These and certainly some additional effects have to be investigated more thoroughly if one wants to model the conductivity – density behavior more closely. However, since our goal was to prove the existence of such a relationship and subsequently explain the physical basis, we did not pursue these contemplations any further. Additional work is required should one want to generate a universal formula for the calculation of the conductivity of green-state P/M compacts at all densities.

4.3. Conductivity-Density Relationship for Green P/M Samples

The conductivity-density relationship for green-state P/M samples lies at the core of our proposed approach to the measurement of density variations throughout the volume of a sample by injecting currents and conducting voltage measurements on its surface. Since we are basically measuring conductivities, the ability to relate the recorded conductivity to a certain density is a necessity. The extensive measurements together with the theoretical considerations produced some interesting results in this respect.

The nature of the conductivity-density relationship for green-state P/M samples is not independent of the powder mixture. While it was expected that the absolute value of the conductivity would change with the conductivity of the main powder constituents, the qualitative difference encountered between lubricated and non-lubricated parts was surprising. It was found that the relationship for non-lubricated parts follows a linear dependency over the whole density range. This allows for easy reconstruction of densities from any given conductivity measurement over the whole range.

The relationship in lubricated parts is more complex and is not only non-linear, but it even exhibits an inversion from the expected line at high densities, meaning that the conductivity actually decreases with increasing density after a certain point. This qualitative behavior was found in all samples made from a mixture containing a non-conducting lubricant. The physical considerations detailed in section 4.2 above explain the occurrence of this phenomenon.

The inversion effect renders the density calculation from the measured conductivity more complicated than in the linear case. Even more important, it places some physical constraints to the applicability of our method. Since the sensitivity on the conductivity due to density variations is zero or almost zero in the vicinity of the inversion point, variations around this point cannot be detected with our method. The approach is therefore ill-suited to analyze compacts whose nominal density is at or near the inversion point. However, since the industry trend goes to ever increasing densities, most parts manufactured will stay well "to the right" of the inversion point and will not be affected by this limitation. Also, since this inversion point changes with changing powder mixture, a general statement about the ability to measure parts of a certain density cannot be made. It has to be determined for each mixture individually.

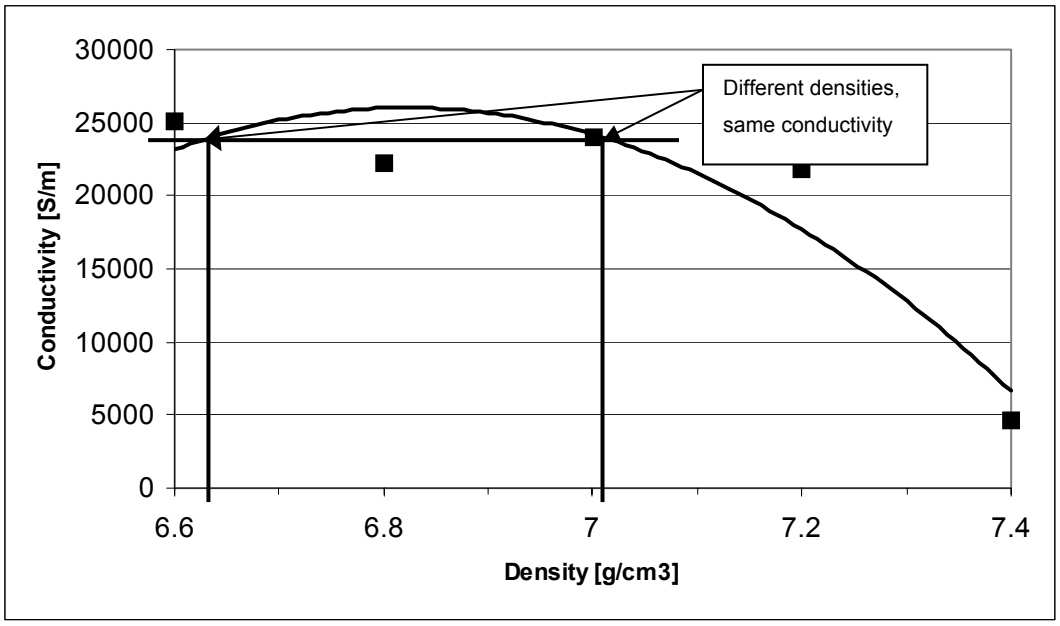

Figure 4.21: Two different densities with the same conductivity in a green-state sample of 1000B with 0.5% AWX.

Additionally, the inversion behavior produces an ambiguity for the density reconstruction. Since the conductivity decreases again with increasing density, there are usually two densities for any given conductivity reading, as shown in Figure 4.21. Naturally, this would prevent a successful density reconstruction from a conductivity measurement. This complication can be overcome with the additional information that is usually available when analyzing a compact. When we are given a green-state sample with a nominal density of 7.1g/cm^3, we can expect a reading in the vicinity of this nominal value. Should a measurement result in a conductivity of 24000S/m, we could therefore conclude that the density must be 7.02g/cm^3. And after we have established a

number of density values, we know that the density will vary only gradually. Any new reading taken in the vicinity of the previous ones will not show a drastically different density value. This again gives us enough information to overcome the ambiguity and to select the correct density value when presented with a new conductivity measurement.

Although the nature of the conductivity-density behavior encountered in lubricated green-state P/M samples somewhat complicates the task of measuring density by recording conductivities, the proposed method can still be used successfully in most cases.

5 Electric Impedance Tomography

5.1. Introduction

5.1.1. Definition of Tomography

The term tomography refers to a general procedure for the synthesis of two-dimensional (2D) cross-sectional images or slices of a three-dimensional (3D) object. The images are obtained from external measurements of a spatially varying function. Line integrals are the most common external measures, which are also known as projections. Availability of multiple projections at different orientations allows accurate recovery of the original tomogram. Additionally, several of these 2D images can be stacked together to obtain a 3D representation of the object.

Tomographic systems allow one to view the internal structure of objects in a noninvasive and nondestructive manner. There are several methods available to record these 2D images and, depending on the specific method, tomographic inspection can be used for many different applications. Because practical implementation of tomography typically requires the management of a large amount of data combined with extensive numerical calculations, modern computing technology is indispensable for tomographic applications. Hence, the term CT for computerized tomography applies to all of today's tomographic applications.

By far the best known tomographic application is the X-ray imaging of the human body. A commercial X-ray imaging system is shown in Figure 5.1. Other medical devices, including ultrasonic scanners and magnetic resonance imaging systems, also make use of tomographic principles. Outside the medical realm, tomography is used in applications ranging from microscopy through nondestructive material testing and radar imaging to geophysical imaging and radio astronomy.

Figure 5.1: Medical X-ray CT system, which conducts scanning 2D projections and reconstructs 3D images.

In order to understand the advantages of tomographic image reconstruction, let us look at the differences between conventional X-ray radiography and X-ray computer tomography. In conventional X-ray radiography, a stationary source and planar detector are used to produce a 2D projection image of the patient. This image has an intensity proportional to the amount by which the X rays are attenuated as they pass through the body. In other words, the 3D spatial distribution of X-ray attenuation coefficients is projected into a 2D image. The resulting image provides important diagnostic information due to differences in the attenuation coefficients of bone, muscle, fat, and other tissues in the 40 keV to 120 keV range used in clinical radiography. The utility of conventional radiography is limited by the fact that the 3D anatomy is projected into a 2D image, causing certain structures to be obscured. For example, tumors in the lung may be obscured by a more dense rib that projects into the same area in the radiograph.

Computerized tomography systems do not form the image directly as in the case of conventional techniques. Instead, several 2D pictures are obtained by rotating the source and detector around the investigated object. The sampled data are processed by an image-reconstruction algorithm to produce a digital representation of the desired image. A computed tomography system collects measurements of 1D line integrals, or projections, along parallel paths through a 2D slice of a 3D object. By collecting these projections at different angles relative to a fixed coordinate system, we build up the 2D Radon transform from which the image is reconstructed. This function is based on the theories around the properties of the integrals of *N*-D functions over (*N* - 1)-D hyperplanes.

In the early days of computing, one major limitation of the first generation of CT systems was that a single scan would take several minutes and the subsequent computational time again would be on the order of several minutes for a single image. Using modern scanning techniques and the computational power of today's computers, modern scanners can scan a single plane in less than one second.

Tomographic principles have also been applied in a number of other diagnostic medical imaging instruments. One major application, for which the early developments actually were researched before X-ray CT, is nuclear imaging. Based on the same principle of measuring the varying absorption of electromagnetic waves, measurements of physiological processes are obtained by tomographic imaging of the spatial distribution of a biochemical tracer or probe that has been tagged with a radioactive isotope. Using these systems with various probes, it is possible to produce 3D images of metabolic activity throughout the body, variations in neurotransmitter and receptor densities in the brain, and the functioning of the heart and blood vessels.

Magnetic resonance imaging (MRI), another well known tomographic application in the medical field, differs from X-ray and emission CT in the sense that the image Fourier transform or "k-space" is measured directly. This is achieved by using a magnetic field gradient to produce a spatial frequency-encoding of the magnetic resonance signal from hydrogen nuclei in the body. Using combinations of time-varying magnetic field gradients and radio-frequency pulses, it is possible to obtain k-space measurements with a wide range of sampling patterns. This encoding allows measuring the response from each sub-volume separately and provides an easy way to build an image.

Tomographic methods have also proven very powerful in applications other than medical imaging. Different systems have been widely used for nondestructive testing of manufactured components and materials. Tomography has also had an enormous impact in exploring the natural world. Applications range from microscopic imaging using electron micrographs and microscopes to imaging of celestial bodies using radio telescopes. Electromagnetic techniques have been used for resistivity imaging between bore holes in geophysical applications and imaging of ionospherical electron density. Similarly, acoustical signals have been used for tomographic imaging over a wide range of scales from acoustic microscopy to large-scale mapping of the oceans grounds, as well as 3D mapping of the earth's interior using natural seismic data.

5.1.2. Principles of Electric Impedance Tomography

Electric Impedance Tomography (EIT) refers to a specific method to acquire the data used in the tomographic reconstruction. According to its name, it characterizes and images the distribution of the electric impedances in the analyzed object. EIT is a non-invasive, non-

destructive technique, in which we inject currents into a body and measure the resulting electric potential using electrodes placed on the boundary of the volume. Then, using this boundary data of current and voltage measurements, the internal electric impedance of the inspected volume is reconstructed and visualized in either a 2D or 3D graph.

EIT provides a technique to inspect the internal electric impedance or conductivity from external measurements. The knowledge of this conductivity distribution can then be used to determine certain properties of the volume that is to be analyzed without having physical access to the inner regions of this volume. Of course it is essential that the investigated property is linked to the electric impedance of the body and that changes in the material result in changes of the impedance. Key properties of the EIT method are:

- Non-destructive, non-invasive access to internal sections of the analyzed volume.
- Low cost
- Low risk
- Compact system
- Visualization of properties

Like all other tomographic applications, EIT has its limitations. For EIT, these include the inability to probe enclosed high impedance layers due to the limited current penetration into these regions, and low resolution, due to the limited number of independent measurements that are feasible. These limitations dictate the applicability of EIT to certain measurement conditions. In general, EIT is best suited to measure impedance variations over large distances compared to the electrode placement, or to monitor impedance changes with time.

Impedance imaging was first developed by Dynes and Lytle in 1981 [65]. Its application to the medical field, which is today's best known and most researched application of the method, was introduced in 1982 by Barber and Brown [6]. Since different tissues in the human body have different impedances, it is possible to discriminate tissues from the impedance measurements as well as to detect physiological events that change the electric impedance of the tissue.

Whether the application of EIT is of medical nature or not, the principles of the method remain largely the same in all cases. A direct or alternating current is injected into the inspected volume through strategically placed surface electrodes. Differential voltage measurements through the remaining electrodes are recorded. Usually, the current injection and voltage recording pattern is varied and several measurements with different configurations are taken. The voltage data from these measurements is then fed to a reconstruction algorithm that calculates

the impedance distribution in the tested volume. Figure 5.2 shows a block diagram of the main components of an EIT system.

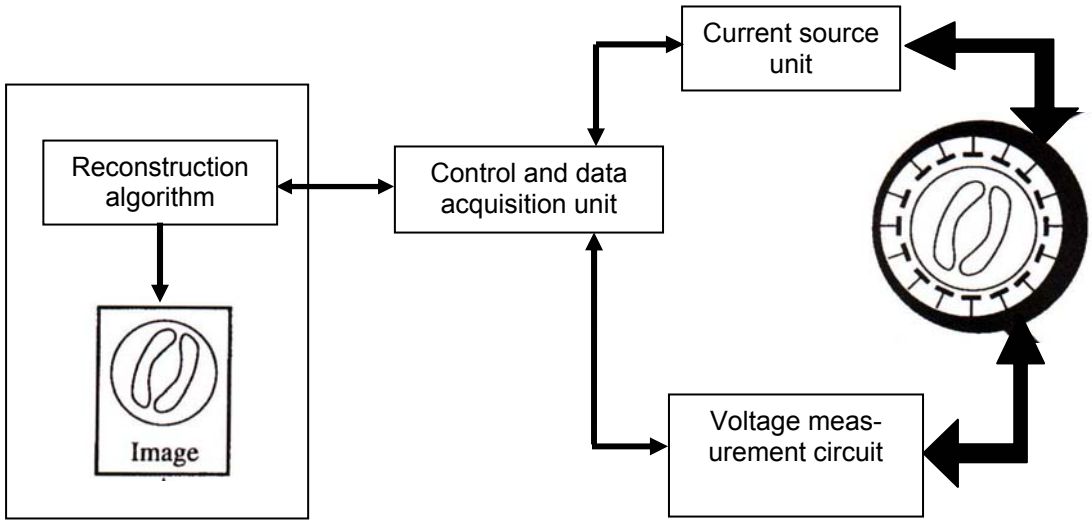

Figure 5.2: Generic system arrangement of EIT.

Due to the nature of the physical phenomenon employed to discriminate between regions exhibiting varying properties, the reconstruction of the impedance distribution from the recorded data is quite complicated. Unlike X-ray CT, where the image represents a line integral of the absorption characteristics of the material, the voltage distribution resulting from a specific current injection pattern is very difficult to calculate. Since the electric currents do not follow a predefined, well known path, but rather are influenced by the unknown impedance distribution of the material, the task of reconstructing the impedance is much more daunting. The fact that the current flow and hence, the voltage distribution, is influenced by the unknown medium property, calls for an iterative procedure to calculate it.

Similar to other tomographic techniques, EIT is used by applying a source of energy, in this case electric current, to the boundary of the volume of interest. Through a number of electrodes placed on the same boundary, the absorption characteristics of the material to the specific form of energy are recorded, here in the form of electric potentials. In order to find the distribution of the unknown physical property, the impedance, we have to solve two separate problems. First, we need to solve the so called forward problem. Given the boundary conditions of the current injection and flux free boundaries as well as the conductivity distribution, the forward problem calculates the expected voltage distribution throughout the volume. Starting with Laplace's equation (3.2), the electric potential in the volume is calculated. Since for most volume shapes it is not

possible to do so in closed form, numerical techniques have to be used instead. Therefore, the forward problem usually involves the setup of a numerical model based on the model parameters, and result in a prediction of what the data would look like, if the parameters were as assumed. In the second step, the actual data is compared to the data prediction obtained from the forward problem. The differences between the actual and the predicted data lead to a new estimation of the model parameters through the solution of the so called Inverse Problem.

The inverse problem tries to find the model parameters, given the boundary conditions and the measurement data. Figure 5.3 illustrates the differences between the forward and the inverse problem. As suggested by their names, the data flow in the two problems is directly opposite. In the forward case, we assume to know all the model parameters and material properties, from which we can then calculate the system data at any point. In the inverse problem, on the other hand, we know the data from measurements and try to calculate the material parameters.

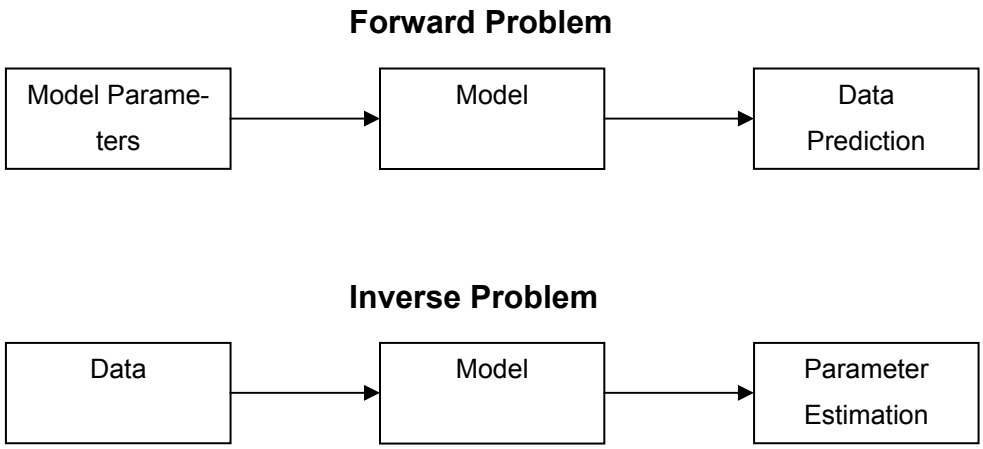

Figure 5.3: Differences between the forward and the inverse problem.

In some cases it is possible to directly solve for the model parameters using an inverse solution to the forward approach. In these cases, a system of linear equations with model parameters as unknowns can be established that can be solved using regular linear algebra or numerical techniques. This is the most direct approach as suggested by Figure 5.3. The solution of the inverse problem in EIT, however, can usually not be solved directly. This is due to the fact that the model parameters and the data as presented in the boundary conditions and the voltage measurements have a non-linear relationship. In these cases, an iterative approach, utilizing both the forward and inverse solution, is required to produce an EIT image. Usually, a forward solution is produced with a set of assumed model parameters. The result of the forward solution is then

compared to the boundary data and the model parameters are adapted in an attempt to minimize the difference between the forward solution and the measured data.

5.1.3. Applications

The basic principles of EIT can be used in many different applications. Successful use of the method has been employed in fields as diverse as chemical process engineering, biomedical and environmental applications. With its advantageous properties of low cost and low risk, EIT has found applications practically everywhere where physical properties can be linked to the electric conductivity distribution. Specifically, some examples are:

- Medical imaging of internal organs and tissue
- Geological examinations
- Non-destructive evaluation of conductive materials
- Industrial process monitoring

It is important to note that by monitoring the differences of electrical impedance, differentiation not only based on the impedance itself, but also on factors influencing the impedance can be observed. In medical applications for example, the conductivity of blood is strongly dependent on the blood temperature. Hence, thermal monitoring for hypo- or hyperthermia patients is an application for EIT, where the monitoring of the blood impedance is used to monitor the thermal stability of a patient.

Another example, where the conductivity variations that are measured through EIT are used to characterize a different property, is the application we propose to measure density variations in green-state P/M parts. As we have demonstrated in chapter 4, the density of green-state P/M compacts is closely related to their conductivity. By imaging the electric conductivity throughout the part, we can therefore measure the density.

EIT can be carried out in two different ways. One method is the so called static imaging, where the absolute values of the impedance are measured and reconstructed. Another approach that is especially popular in medical applications is the dynamic imaging [33]. Dynamic imaging records a first set of boundary data at time T_1 as a reference set. Then, at time T_2, an additional boundary data set is measured. By back-projecting the difference between them, a dynamic image of the impedance change can be extracted, showing any changes in the impedance distribution between the times T_1 and T_2 [6]. Difference imaging is considerably easier to implement than static imaging since various errors are cancelled out by the subtraction process. However, dynamic imaging can only be employed for cases where the parameter that is to be observed, is expected to change within a short time span. Medical applications are good candidates for the

differential process, since the physiological processes introduce a constant change of many parameters.

5.1.4. Notation

The following notation is used in the subsequent sections dealing with the mathematical aspects of EIT (see also Figure 5.4):

- Ω studied domain, open, bounded, three dimensional
- Γ boundary of Ω that can be divided into Γ_N, where the Neumann boundary conditions apply and Γ_m, where the Dirichlet boundary conditions apply.
- $\overline{\Omega}$ $= \Omega \cup \Gamma$
- Γ_m Subset of Γ made up of the points where voltages are measured, defining a Dirichlet boundary condition.
- Γ_N Subset of Γ made up of the points where the current source is applied, defining a Neumann boundary condition.
- σ $= \sigma(x, y, z)$ conductivity distribution
- $\mathbf{n}$ unit vector of the normal to Γ directed toward the exterior of Ω
- $\mathbf{J}_0$ injected current density
- $\mathbf{\Phi}$ calculated electric potential
- $\mathbf{\Phi}_m$ vector of electric potential measured on Γ at points Γ_m
- M mesh (set of sub elements of the main area of interest)

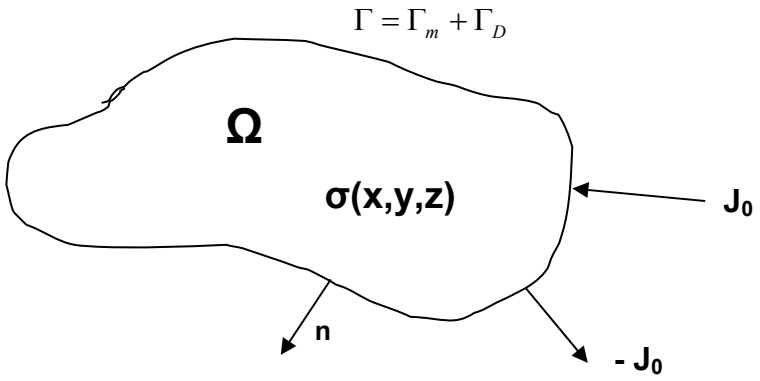

Figure 5.4: Problem domain and its notations.

5.2. Forward Solution

5.2.1. Problem Description and Basic Equations

The problem of calculating the steady state solution in any configuration, given the equations governing the physical situation and given the problem parameters and boundary conditions is usually referred to as the forward problem. In the case of EIT, the forward problem consists of finding the potential distribution in a three dimensional space given the electrical properties of the material and the boundary conditions. The governing equations for this problem are:

$$\nabla \cdot \sigma \nabla \Phi = 0 \tag{5.1}$$

in the domain Ω, subject to the boundary conditions

$$\sigma \frac{\partial \Phi}{\partial n} = J_0 \quad \text{on } \Gamma_N, \tag{5.2}$$

$$\Phi = \Phi_m \quad \text{on } \Gamma_m. \tag{5.3}$$

Because of the complexity of the three dimensional integrals, the techniques applied above to the cylindrical samples can not be applied to geometrically more complex parts. The underlying physics are the same; we still use Poisson's equation as given in (5.1). However, be-

cause the volume integrals that generate the solution can no longer be solved analytically, one has to resort to an approximating numerical approach for evaluation.

The most widely used numerical modeling approach to solve the forward problem is the finite element method. Here the basic concept relies on a suitable discretization of the problem geometry. Once that is accomplished, the computational method can then determine the voltage distribution on the surface of the P/M sample from the knowledge of the geometry of the sample and the current injection points. In our approach the entire sample volume is discretized into polyhedrons. The continuous electric potential inside the part is approximated as an interpolation over a finite number of discrete elements. Within each of the volume elements, the governing equation is represented through approximation functions as a linearized set of algebraic equations. Assembling all the elemental equations into a global, linear matrix equation, the governing differential equation can subsequently be solved for the electric potential throughout the entire volume.

The finite element method is particularly useful when the conductivity distribution inside the sample is non-uniform or when the shape of the part is such that analytical solutions for the potential distribution cannot be found. Both of these conditions render the task of solving (5.1) practically impossible. The division of the volume into many small parts overcomes both of the problems at the same time. For elements that are small enough, the conductivity within each element can be considered constant, and, choosing an appropriate geometry for the elements, a solution on each element can be found easily. Unfortunately, to achieve high accuracy, the size of the linear system of algebraic equations can be very large.

5.2.2. Discretization

The subdivision of a large, difficult problem into numerous smaller, better manageable tasks, and the subsequent reconstruction of the original system, is a technique that is used in practically all scientific, engineering or other complex work. As such it is a well known, thoroughly investigated approach. The finite element approach used to compute the forward solution is a classic example of this strategy [63].

In order to implement this method, the volume is discretized into a finite number of elements. This discretization naturally introduces an approximation of the true solution, which, hopefully, approaches the true continuous solution in the limit where the number of elements becomes infinite. This discretization of the problem is general to the specific application for which it will be eventually used; hence it is possible to define a standard discrete system. This standard discrete system can be described as follows [83]:

1. The continuum is divided into a finite number of elements, the behavior of which is specified by a finite number of parameters.
2. The solution of the complete system follows exactly the same rules as those for each sub element.
3. A set of discrete parameters a_i can be identified which describe both the behavior of each element e and of the whole system.
4. For each element a set of quantities q_i^e can be computed in terms of the system parameter a_i that usually can be linearized to be of the form

$$q_i^e = \sum_{j=1}^{n} F_{ij}^e a_j + c_i^e \tag{5.4}$$

5. The system quantities r_i can be found by simply adding the element quantities

$$r_i = \sum_{e=1}^{m} q_i^e \,, \tag{5.5}$$

which, in the linear case, results in a system of equations that can be represented in matrix form as

$$\mathbf{Fa} + \mathbf{c} = \mathbf{r} \,, \tag{5.6}$$

such that

$$F_{ij} = \sum_{e=1}^{m} F_{ij}^e \qquad c_i = \sum_{e=1}^{m} c_i^e \,. \tag{5.7}$$

This system of linear equations, after imposing the required boundary conditions, can now be solved for the system parameters a_i.

This standardized discrete system can be used for any electrostatic problem set, in which the governing differential equation is linearized on the element level.

5.2.3. Mesh Generation

The finite element method is based on solving discretized linear equations on small sub-sections of the volume, for which the approximations are valid. The sum of these solutions will then make up the solution of the complex two- or three dimensional spaces. Mesh generation is the process that discretizes the continuous volume. With increasing computational power available on every desk, the finite element method in recent decades has become a mainstay for industrial engineering design and analysis. Increasingly larger and more complex designs are being simulated using the finite element method. A very important part of the finite element method is the mesh generation.

Mesh generation can be defined as the process of breaking up a physical domain into smaller sub-domains (elements) in order to facilitate the numerical solution of a partial differential equation. While meshing can be used for a wide variety of applications, the principal application of interest is the finite element method. Surface domains may be subdivided into triangle or quadrilateral shapes, while volumes may be subdivided primarily into tetrahedra or hexahedra shapes. The shape and distribution of the elements is ideally defined by automatic meshing algorithms.

With the growing importance of three-dimensional simulation mesh generation has become a critical factor. Since the quality of the mesh directly influences the precision of the subsequent finite element calculations, this step carries a lot of emphasis. With the complex three-dimensional models that are to be meshed, the generation of a suitable mesh often becomes the bottle neck and poses more difficulties than the subsequent simulation. The amount of data in three dimensions requires efficient and more sophisticated algorithms and data structures and increases the complexity of the meshing task considerably. Meshing algorithms that have worked well for two-dimensional problems are often not feasible for higher dimensions. Manual partitioning techniques are not desirable and cannot be efficiently applied to model descriptions which contain several thousand or more vertices.

At the inception of the finite element method, most users were satisfied to simulate vastly simplified forms of their final design utilizing only tens or hundreds of elements. Painstaking pre-processing was required to subdivide domains into usable elements. Nowadays users expect to mesh complex domains with thousands or millions of elements with no more interactions than the push of a button.

A mesh can be defined as follows: a mesh of a domain Ω is defined by a set M of finite number of segments in 1D; segments, triangles and quadrilaterals in 2D; and segments, triangles, quadrilaterals, tetrahedra, pentahedra and hexahedra in 3D. In order to represent a quality mesh, it has to conform to three basic rules:

1. The domain Ω is completely and exactly covered by the mesh M. When the domain Ω is not polygonal (in 2D) or polyhedral (in 3D) (i.e., if it is defined by a smooth curve or a surface), the mesh M can only be an approximate partitioning of the domain.
2. All elements of mesh M must have a non-empty interior.
3. The intersection of any 2 elements in the mesh M is either an empty set, a point, an edge or a face (of both elements).

Figure 5.5 shows both a conformal and a non-conformal mesh.

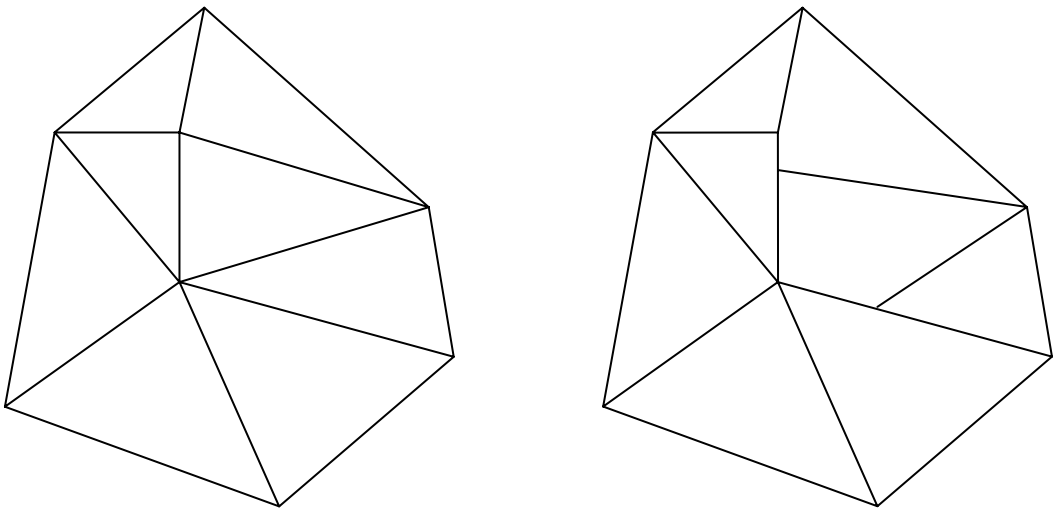

Figure 5.5: Conformal (left) and non-conformal mesh (right).

The quality of a mesh can be measured according to several criteria. Some of these criteria that are applicable to planar/surface meshes are:

1. The variation in the area or the volume of the elements should not be too large. The smaller the area or volume distribution of the elements is, the higher is the quality of the mesh.
2. The aspect ratio of triangular elements should be as close to 1 as possible. The aspect ratio of a triangular element is defined as the ratio of the circumradius of

the triangle to twice its inradius. Hence the aspect ratio of an equilateral triangle is exactly 1.

3. The ratio of the largest to the smallest edge, angle or face of the element should be close to 1.
4. Variations in the dimensions of the elements should not be large locally. I.e. elements should be very similar to their respective neighbors and changes should be gradual over the whole mesh.

Another important parameter of the mesh is its connectivity. The connectivity of a mesh is defined as the manner in which its vertices are connected. Two basic types of connectivity exist, structured and unstructured. A mesh is called structured if the connectivity is same throughout the mesh and each element has a fixed number of neighbors. An unstructured mesh does not have a fixed connectivity among its elements. An illustration of both types is provided in Figure 5.6. There is no preference towards either type of mesh connectivity. However, for complex volumes it is almost impossible to keep a structured mesh. A mesh is therefore mostly unstructured in order to optimize the mesh quality.

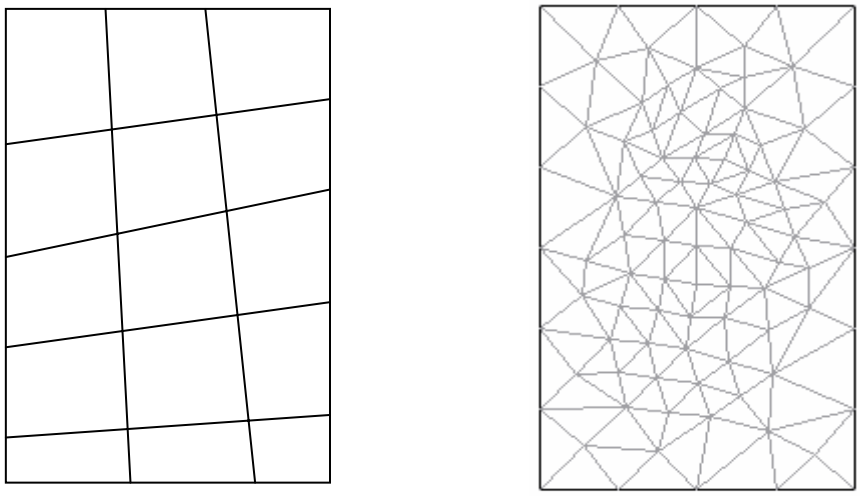

Figure 5.6: Structured (left) and unstructured mesh (right).

For the finite element discretization in our simulations we selected tetrahedral elements for our mesh. A mesh consisting of triangular elements in two-dimensional applications and tetrahedral elements for three-dimensional volumes has some advantages over other geometrical shapes. For one, elements of this shape result in a simple mathematical problem formulation.

Another important advantage is the adjustability of their area or volume. This makes them ideally suited for complex geometries, where the size of the features varies widely.

The first step in the discretization of the solid is the generation of nodes. Nodes are the points in space where the field and source functions of our simulations will be evaluated. Because we are dealing with Laplace's equation as defined in (3.2), the field function is the scalar electric potential Φ and the source function is the current source distribution *f*, which is zero inside the solid.

The method of node deployment is arbitrary and depends only on the desired degree of accuracy in our approximation. It is beneficial to have a higher node density where we expect to have a highly nonlinear behavior of the electric potential, i.e. around corners and edges of the part. The total number of deployed nodes is also arbitrary, but we have to trade-off between approximation accuracy and computational complexity, because the number of unknowns in our system of linearized equations and hence the size of the final matrix equation is directly proportional to the number of nodes.

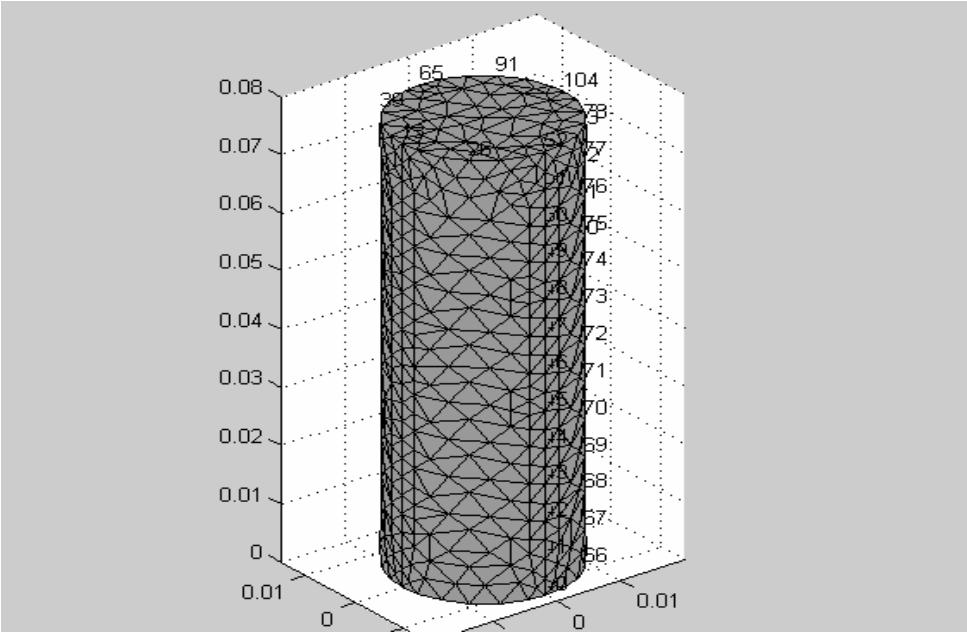

Figure 5.7: Three-dimensional finite element mesh on cylindrical sample (dimensions are given in meters).

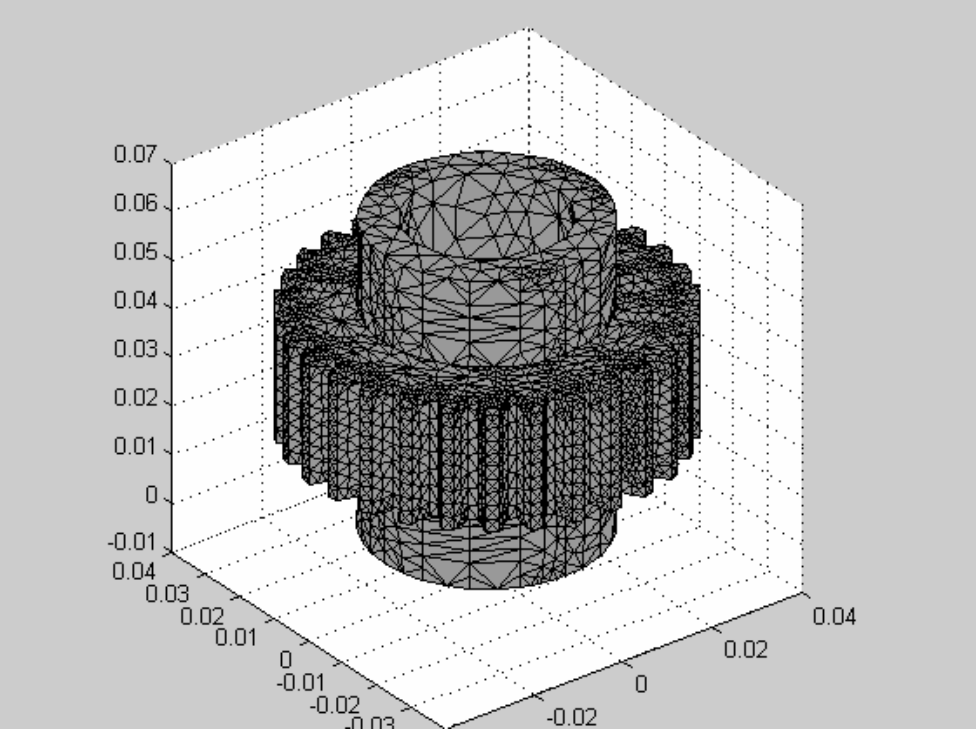

Figure 5.8: Three-dimensional finite element mesh on a geometrically complex part (dimensions are given in meters).

The nodes are then connected to form tetrahedrons. Care has to be taken not to create odd-shaped tetrahedrons, where some angles are very large or very small, which would reduce the quality of the mesh. As discussed above, the ideal element is a tetrahedron formed by equilateral triangles with all angles equal to 60°. Examples of such mesh generation are given on a relatively simple, cylindrical part in Figure 5.7 and a gear (provided by Borg Warner) in Figure 5.8. The differences in the regularity of the two meshes are clearly visible. The relatively simple geometry of the cylinder allows a very regular, structured mesh to be set up, while the complex geometry of the gear together with the widely varying dimensions of its features result in a mesh that is irregular and non-structured.

5.2.4. Basis Functions

In order to numerically calculate the potential inside the domain Ω, we need to linearize the governing differential equation. This linear approximation is valid for a small element e. A way to achieve this is to approximate the non-linear equation by a set of linear basis functions. Any

function $f(x)$, defined in an interval $0 < \mathrm{x} < \mathrm{k}$, may be expanded in terms of a complete set of functions $\{f_n(x)\}$ as [17]

$$f(x) = \sum_{n=1}^{\infty} a_n f_n(x), \tag{5.8}$$

with a_n the unknown weights of each basis function. Such a set $\{f_n(x)\}$ forms a basis in the function space, or in other terms, the set $\{f_n(x)\}$ spans the Hilbert space. Additionally, if the functions $f_n(x)$ are orthogonal, they can be normalized to build an orthonormal basis of the function space.

From the inner product definition one obtains for the coefficients a_n

$$a_n = \langle f, f_n \rangle, \tag{5.9}$$

where $\langle f, f_n \rangle$ is the inner product between functions $f(x)$ and $f_n(x)$ over the specified domain, here $0 < \mathrm{x} < \mathrm{k}$, defined as [70]

$$\langle f, f_n \rangle = \int_0^k f(x) f_n(x) dx. \tag{5.10}$$

and an iterative method can be used to calculate the weights for each basis function. In most cases however, the infinite sum is truncated and the weights are found by solving the resulting matrix equation.

Applying the concept of basis functions to our problem of calculating the electric potential Φ throughout the domain Ω and according to the standard discretization system, we can approximate the differential equation through a finite set of local basis functions as follows:

$$\Phi \approx \sum_{i=1}^{n} F_i a_i = \mathbf{F}\,\mathbf{a}, \tag{5.11}$$

The basis functions are arbitrary, as long as they conform to the general requirements for basis functions as outlined above. In order to find the set of functions that both is practical to use on a large scale and gives a good approximation of our problem, we first rewrite the main equa-

tion for the potential (5.1) in its weak form. This relaxes the continuity restrictions on Φ and leaves us with a broader choice for our basis functions. The weak form of (5.1) is [32]:

$$\int_{\Omega} \nabla v \cdot \sigma \nabla \Phi d\Omega - \int_{\Gamma} v J_0 d\Gamma = 0, \tag{5.12}$$

where v is an arbitrary function. The integral form permits the approximation to be obtained element by element and assembly of the whole system be achieved by summing the solution of the elements as defined in the standard discrete system. Specifically, the weak form allows discontinuities of the second derivative of Φ, where the original form requires both the first and second derivative of Φ to be piecewise continuous. This represents better the behavior we expect from the potential. We are approximating Φ to be piecewise continuous in Ω, which will lead to jump discontinuities is its derivatives.

Two different methods are available to obtain the basis functions and calculate the approximation in the weak form. We choose the method of variational principle, since it always results in a symmetric matrix system [72]. This in turn allows for faster computation. In general terms this results in a matrix equation for the coefficients a of the basis function as

$$\mathbf{H}\,\mathbf{a} = \mathbf{g}, \tag{5.13}$$

where **H** is a $n \times n$ matrix and **g** is a vector of length n. Mathematically these entities are defined as

$$H_{ij} = \int_{\Omega} \sigma \nabla F_i \cdot \nabla F_j d\Omega, \text{ and} \tag{5.14}$$

$$g_i = \int_{\Gamma} F_i J_0 d\Gamma, \tag{5.15}$$

Applying these general concepts to our specific problem of calculating the potential within a given volume, we formulate a choice for our basis functions. According to the discussion of the mesh generation in Section 5.2.3, we choose tetrahedral elements to subdivide the volume. The conductivity of each element is assumed constant. Since the system property a_i that is sought in our case is the electric potential, the a_i of the standard discrete system now refer to the potential at each node of our mesh. Subsequently, the basis functions are chosen such that they interpolate the potential linearly between each node. This automatically guarantees that the sum of these basis functions results in the overall potential according to (5.11). The interpolation works in such a way that the value of the basis function F_i is 1 at node i and drops off linearly towards

each of its neighboring nodes. It is zero at each node except node i and zero everywhere between nodes except between node i and its neighbors.

5.2.5. Finite Element Solution

The previous sections have laid the ground work to generate a finite element solution for the equations governing the electric potential in a bounden volume. Now we have to apply the general principles to our specific problem and set up the system of linear equations that allows us to solve for the potential Φ throughout our volume. As we have seen, equations (5.14) and (5.15) allow us to calculate the coefficients for each basis function in the approximation of the potential. However, we would like to break down the calculation to the element level. Each tetrahedral element is assigned a constant conductivity that can vary from element to element. We can therefore rewrite the integral expression for each element in the H matrix such that it is comprised of the sum of sub-matrices $\mathbf{H}_e$, each describing the contribution of one element to the global matrix **H** as follows:

$$H_{ij} = \sum_{e=1}^{m} \left[\mathbf{H}_e\right]_{ij} . \tag{5.16}$$

The procedure to calculate the sub-matrices is much simpler, since we have to integrate (5.14) only over the volume Ω_e, which is the volume of the e-th element, where the conductivity σ_e is constant. Rewriting (5.14) we obtain

$$H_{ij} = \sum_{e=1}^{m} \left[\sigma_e \int_{\Omega_e} \nabla F_i \cdot \nabla F_j \, d\Omega \right]. \tag{5.17}$$

Since the interpolation functions are defined in such a way that they only contribute between a node e and its neighboring nodes, we know that most elements of the matrix $\mathbf{H_e}$ are zero. Non-zero entries are only those where both the i-th and j-th node belong to the e-th element. This fact allows us to define a new, local matrix $\overline{\mathbf{H}}_e$ that acts only on the element e and, hence, contains only four entries, one for each node in the tetrahedron.

Using the local 4x4 matrix we note that the interpolation function F_i, which was previously defined for the whole volume, can now be rewritten in terms of the local coordinates of the e-th node. Since these functions interpolate linearly between the e-th node and its neighbors, the local version $\overline{F}_i$ can be written as

$$\overline{F}_i(x,y,z) = \alpha_i + \beta_i x + \gamma_i y + \delta_i z\,. \tag{5.18}$$

with $\alpha_i, \beta_i, \gamma_i$ and δ_i constant that depend on the size of each element and that are unique.

With the definition of the interpolation functions, which states that $\overline{F}_i$ is one at node i and zero at all other nodes, we can calculate the coefficients $\alpha_i, \beta_i, \gamma_i$ and δ_i from the following matrix equation:

$$\begin{bmatrix} 1 & x_1 & y_1 & z_1 \\ 1 & x_2 & y_2 & z_2 \\ 1 & x_3 & y_3 & z_3 \\ 1 & x_4 & y_4 & z_4 \end{bmatrix} \begin{bmatrix} \alpha_1 & \alpha_2 & \alpha_3 & \alpha_4 \\ \beta_1 & \beta_2 & \beta_3 & \beta_4 \\ \gamma_1 & \gamma_2 & \gamma_3 & \gamma_4 \\ \delta_1 & \delta_2 & \delta_3 & \delta_4 \end{bmatrix} = \begin{bmatrix} 1 & 0 & 0 & 0 \\ 0 & 1 & 0 & 0 \\ 0 & 0 & 1 & 0 \\ 0 & 0 & 0 & 1 \end{bmatrix}. \tag{5.19}$$

(5.19) can be solved easily to present us with the coefficients for the local interpolation functions $\overline{F}_i$. These coefficients depend on the coordinates of the nodes making up element e and are weighted by the volume of the element, as one can see when algebraically solving (5.19). The volume of each element can easily be obtained by calculating the determinant of the equation containing the coordinates of the nodes. It is worth noting that the local node numbering, and hence the arrangement in the matrix, should be made in a counterclockwise fashion. Numbering of the nodes that does not comply with this scheme will produce wrong or negative volume calculations.

In order to calculate the local matrices $\overline{\mathbf{H}}_\mathbf{e}$ as defined in (5.17), we have to obtain the three-dimensional gradients for $\overline{F}_i$:

$$\nabla\overline{F}_i = \left[\frac{\partial}{\partial x} \quad \frac{\partial}{\partial y} \quad \frac{\partial}{\partial z}\right](\alpha_i + \beta_i x + \gamma_i y + \delta_i z) = \begin{bmatrix}\beta_i & \gamma_i & \delta_i\end{bmatrix} \tag{5.20}$$

According to (5.17) the local matrix can be written as

$$H_e = \sigma_e \int_{\Omega_e} \nabla\overline{F}_i \cdot \nabla\overline{F}_j \, d\Omega = \sigma_e \nabla\overline{F}_i \cdot \nabla\overline{F}_j \int_{\Omega_e} d\Omega = \sigma_e \Delta_e \nabla\overline{F}_i \cdot \nabla\overline{F}_j\,. \tag{5.21}$$

with Δ_e representing the volume of element e. To obtain a compact mathematical representation, we can now assemble all four gradients of the interpolation functions of the four nodes of element e from (5.20) into a matrix $\nabla\overline{\mathbf{F}}_\mathbf{e}$ as follows:

$$\nabla\overline{\mathbf{F}}_\mathbf{e} = \begin{bmatrix} \beta_1 & \gamma_1 & \delta_1 \\ \beta_2 & \gamma_2 & \delta_2 \\ \beta_3 & \gamma_3 & \delta_3 \\ \beta_4 & \gamma_4 & \delta_4 \end{bmatrix}. \tag{5.22}$$

This expression for the gradient of the local interpolation functions for all four nodes representing element e can now be used to obtain the following expression for the local matrix $\overline{\mathbf{H}}_\mathbf{e}$:

$$\overline{\mathbf{H}}_e = \sigma_e \Delta_e \left[\nabla\overline{\mathbf{F}}_\mathbf{e}\right]\left[\nabla\overline{\mathbf{F}}_\mathbf{e}\right]^\mathrm{T}. \tag{5.23}$$

Having dealt with general terms for the system parameters so far, we have to ask ourselves how these general terms relate to the physical reality of our problem. As we have realized earlier that the system property denominated **a** in (5.13) is in fact the electric potential we seek to determine. Hence **a** is renamed to **V** to reflect the common notation for an electric voltage. The source term, **g** in prior notation, refers to the current sources on the boundary of the volume and is subsequently replaced by **I**. The physical entity relating electric voltage and current in a manner similar to **H** in (5.13) is admittance, commonly referred to as **Y**. With this new notation for the parameters, the equation for the master matrix can be rewritten as

$$\mathbf{YV} = \mathbf{I}. \tag{5.24}$$

Equation (5.24) reflects the physical context of (5.13). The local matrices can also be rewritten in the new terms, and the equation for the global admittance matrix Y can be written in terms of the local admittance matrix $\mathbf{Y_e}$ as

$$\mathbf{Y} = \sum_{e=1}^{m} \mathbf{Y}_e. \tag{5.25}$$

In this formulation we now see the true advantage of the finite element method. The local admittance matrix $\mathbf{Y_e}$, which are zero except for the entries corresponding to the nodes of a tetrahedral element, relate the voltage and current in the e-th element as if it were disconnected from

the rest of the volume. In such a small element, the potential can be calculated in a linear approximation. This is exactly what happens when using (5.23). The solution for the complete volume is then found by simply using the superposition principle, i.e. adding the solutions of each element.

When computing the matrices $\mathbf{Y_e}$ we usually separate geometry and material information. This means that these matrices are stored without the conductivity value σ_e in a separate matrix $\mathbf{s_e}$, resulting in the following representation:

$$\mathbf{Y_e} = \sigma_e \mathbf{s_e} \tag{5.26}$$

This way $\mathbf{s_e}$ contains only geometrical information of element e that is related to the mesh generation. Often the finite element mesh for a certain volume is created only once without the need of changing it again. The information stored in the $\mathbf{s_e}$ matrices can therefore be re-used without recalculating it every time we generate a new FEM solution. Also, as we will see later, the inverse algorithm makes use of the geometrical information in $\mathbf{s_e}$.

In order to complete our solution, we must impose the boundary conditions for the current sources as given in (5.2). If we are using K point sources to send current into the volume at locations r_{source} and sinking it at T other points $r_{\sin k}$, these sources are described by

$$J_0(r) = \frac{I}{K}\sum_{k=1}^{K}\delta(r - r_{source}) - \frac{I}{T}\sum_{t=1}^{T}\delta(r - r_{\sin k}) \tag{5.27}$$

with *I* the total source strength. If we choose our mesh in such a way that the source points coincide with nodes on the boundary Γ of the volume Ω, the source vector **I** simply consists of zeros everywhere except at the nodes that coincide with the source nodes, where they reflect the current strength flowing through the particular node.

If we consider a ring source or other area source instead of point sources, we can do so in a similar fashion. Instead of simply dividing the total current strength by the number of point sources, we now have to distribute the total current I over the whole surface area that is contacted by the source. This is accomplished by weighting the contribution of each source node by the area of the surface or boundary elements it is a member of. And again the vector I will contain all zeros except at the locations that correspond to the nodes which are part of the source area(s).

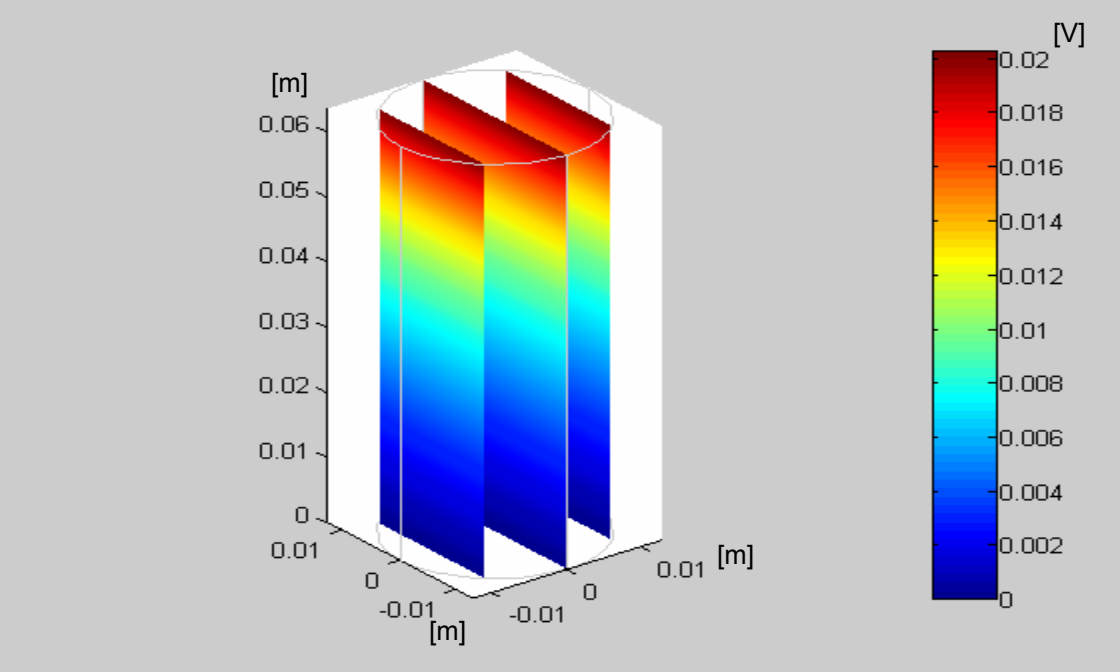

Figure 5.9: Voltage distribution resulting from a non-uniform conductivity distribution in a cylindrical part when injecting a constant current of 1A.

The final step is the application of the boundary condition regarding the potential. In order for the system to have a unique solution, we must set the potential to an arbitrary value at one node in the volume. The easiest solution is to generate a reference to ground, i.e. to effectively set the potential at one node to zero. This is achieved by setting the whole row and column in the admittance matrix **Y** that correspond to the ground node, to zero, except for the diagonal element, which is set to one. This operation renders the **Y** matrix nonsingular and hence insures that the system of linear equations can be solved.

Employing the above procedures, we can now calculate the voltage distribution of our area of interest. Although the matrix system, depending in the size of the generated mesh, can be very large, on the order of several thousand unknowns, powerful of matrix solvers permit us to find the potential distribution efficiently. Figure 5.9 presents the solution applied to a cylindrical P/M part with non-uniform conductivity distribution. The conductivity changes linearly from top to bottom, similar to the behavior expected from a long thin part when pressed in a single punch process. The solution is presented in a slice view, displaying the voltage throughout the volume, supposing a uniform current density resulting from the injection of 1A over the whole top and bottom surface areas.

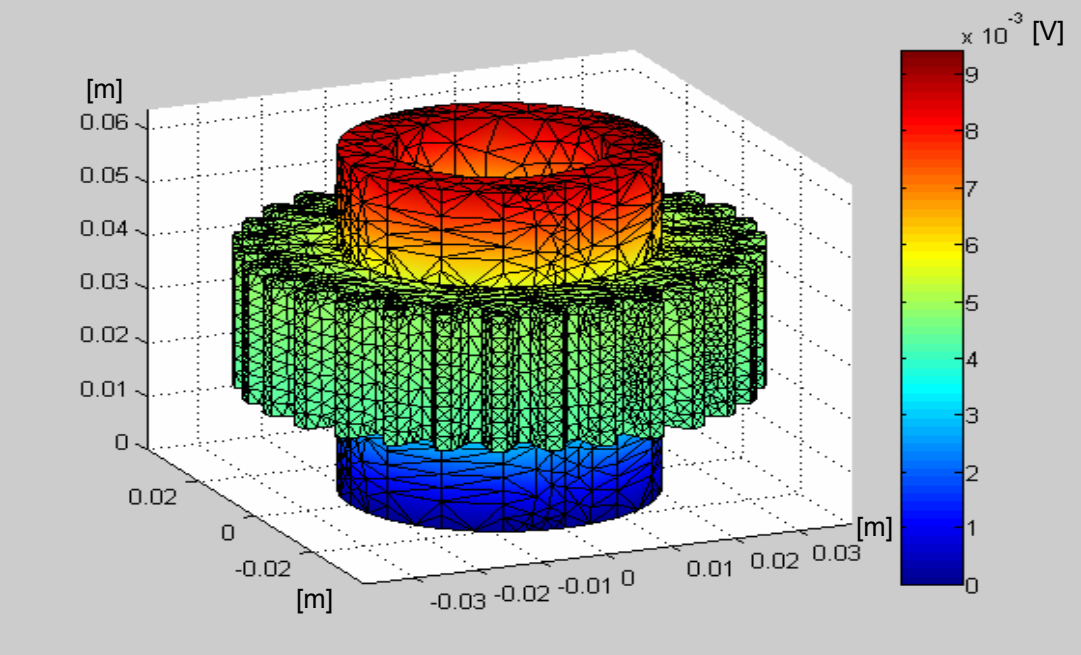

Figure 5.10: **Voltage distribution on the surface of the gear. The distribution was calculated for a current injection of 1A through the top surface and a ground plane at the bottom surface.**

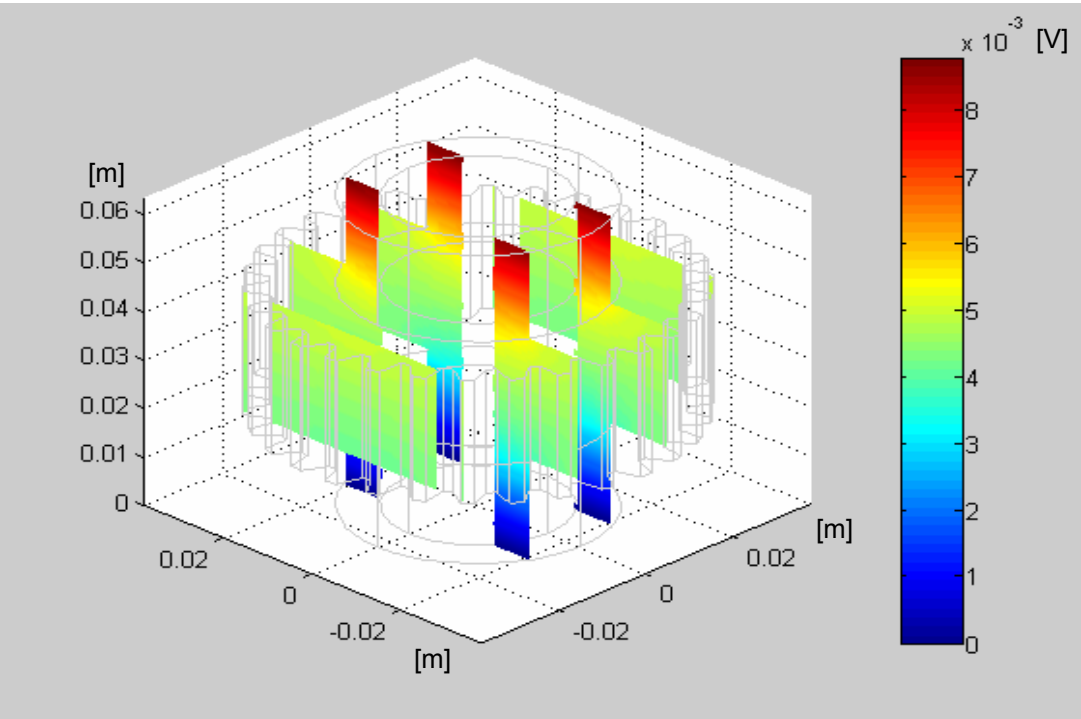

Figure 5.11: **Voltage distribution throughout the volume of the gear.**

As demonstrated in Chapter 3, the solution for a body as simple as a solid cylinder can still be calculated in analytical form, as long as the conductivity is constant within the part. Since this is not the case in the long, thin P/M cylinder, we have to resort to the finite element method to calculate the forward solution. Exact solutions can definitively no longer be found in the case of a complex shaped sprocket. Such a part was obtained from BorgWarner for our experiments. Applying the finite element method to this complex shape and assuming a constant conductivity, Figure 5.10 provides the potential distribution on the surface of the part while Figure 5.11 illustrates the results in the inner sections. Even more details are perceptible in the center slice shown in Figure 5.12, where the non-linearities due to the complex part geometry are readily visible.

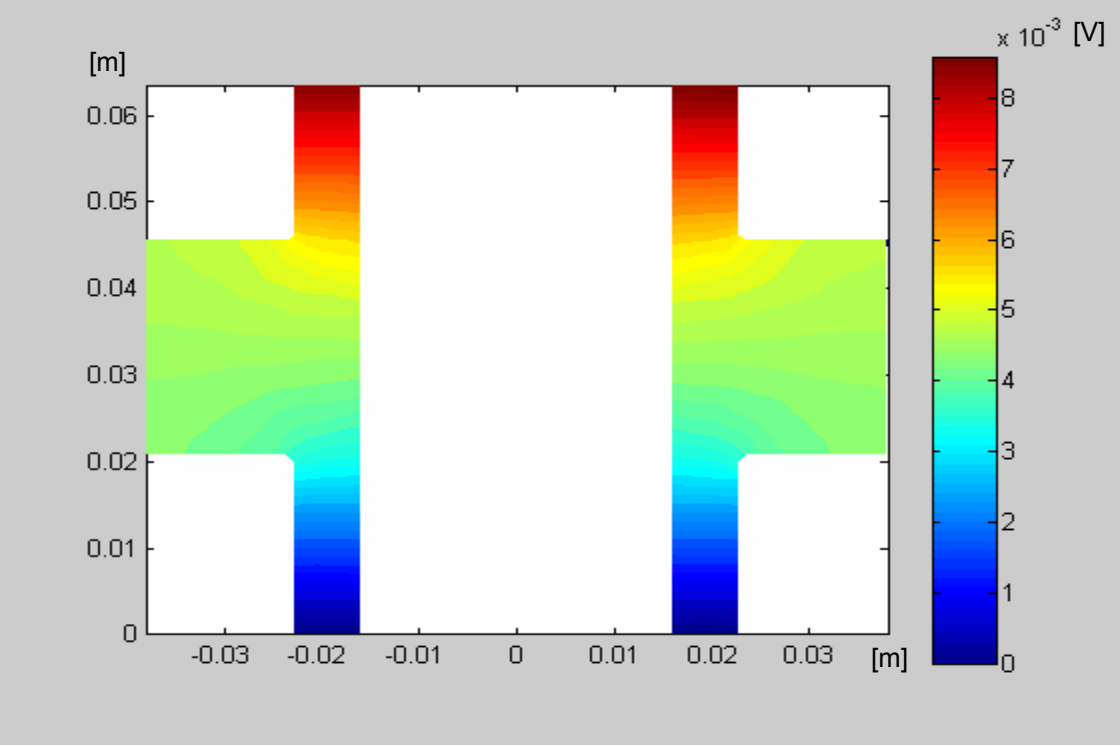

Figure 5.12: Volume distribution in a cross-sectional slice of the gear showing enhanced details especially in the corners of the part.

5.3. Inverse Algorithm

5.3.1. Problem Statement

The inverse problem attempts to find the model parameter, in our case the electric conductivity, given the boundary conditions and the measurement data, as illustrated in Figure 5.3. Contrary to the problem of generating the forward solution, we do not know the conductivity distribution of our part. Rather we have a set of surface voltage measurements and we need to find the conductivity distribution that, given the current injection, produces this particular set of data. The voltage and current density distribution are usually known at select points on the boundary, where either the current is injected or the voltages are measured. The reconstructed parameter distribution within the volume can then be displayed to obtain an image.

Inverse problems arise in a wide variety of different braches of the physical sciences. Some examples are [55]

- Medical tomography
- Image enhancement
- Earthquake location
- Satellite navigation
- Eddy current imaging
- Analysis of molecular structure by X-ray diffraction

While these examples all share the requirement to find the model parameters that govern the system, given the boundary conditions and a set of measured system data, they all have a different approach depending on the specific application. One obvious difference is the frequency range at which the method is used, which varies widely between the different applications. Medical tomography, for example, operates in a very high frequency range (usually > 100MHz). Eddy current imaging, on the other hand, employs frequencies in a medium frequency range on the order of 1MHz, while earthquake location usually uses signals of frequencies on the order of a few kHz.

5.3.2. Approach

The algorithm to solve the inverse problem relies on the forward solver (implemented through the finite element method, see section 5.2) by attempting to find a conductivity distribution that matches both the boundary condition and the calculated potential distribution as closely as possible. Usually, the numerical solution of an inverse problem requires iterative implementa-

tions of the forward problem, adjusting the conductivity distribution during each iteration step in order to minimize the error between the known boundary conditions and the calculated voltage distribution. Figure 5.13 illustrates the algorithm in a few abstract steps. Starting from an initial guess of the conductivity distribution $\boldsymbol{\sigma}_0$, a forward solution of the finite element mesh is calculated. The set of calculated voltages from the nodes that coincide with the measurement locations is then compared to the measurement data $\boldsymbol{\Phi}_m$. If the calculated and measured voltages coincide, we have found our conductivity distribution. If not, the current guess of the conductivity distribution is updated using a minimization scheme to hopefully minimize the difference between the two voltage sets. A new iteration is started using this new approximation for the conductivity distribution. Since we are dealing with vectors, the minimization scheme uses the L_2 norm, which is defined as

$$\left\|\boldsymbol{\Phi}-\boldsymbol{\Phi}_m\right\| = \sqrt{\sum_{i=1}^{m}\left(\Phi_i-\Phi_{mi}\right)^2}\ , \tag{5.28}$$

to define the distance between the measured and the calculated data. Here Φ_i and Φ_{mi} represent the calculated and measured values at the measurement nodes, respectively.

The unknown quantity we are looking to reconstruct is the conductivity of the material. Contrary to the forward problem, the admittance matrix **Y** in (5.24) is now unknown. Instead, we have to try to find **Y** such that both boundary conditions for the source terms and the voltage measurements as stated in (5.2) and (5.3) are fulfilled. This results in the solution of a general system of non-linear equations with a vector valued function

$$\mathbf{F(x)} = \mathbf{y}\ . \tag{5.29}$$

The non-linear nature of the problem makes a general closed form solution almost impossible to find. Instead, an iterative approach is usually taken. The iterative Newton method is an obvious choice, starting with an initial guess for the unknown parameter, in our case σ, and improving this approximation until the resulting voltages match the measured surface closely enough. We must use an error-function minimization method (like least squares) because the system to be solved tends to be either partially under-determined or partially over-determined, and there is no direct correspondence between the surface potential measurements and the conductivity distribution. In addition, the least squares method is the least computationally intensive. By using least squares, we automatically assume that all noise in the measurements is additive and has a normal distribution with zero mean. The success of the least squares method depends crucially on the validity of this assumption.

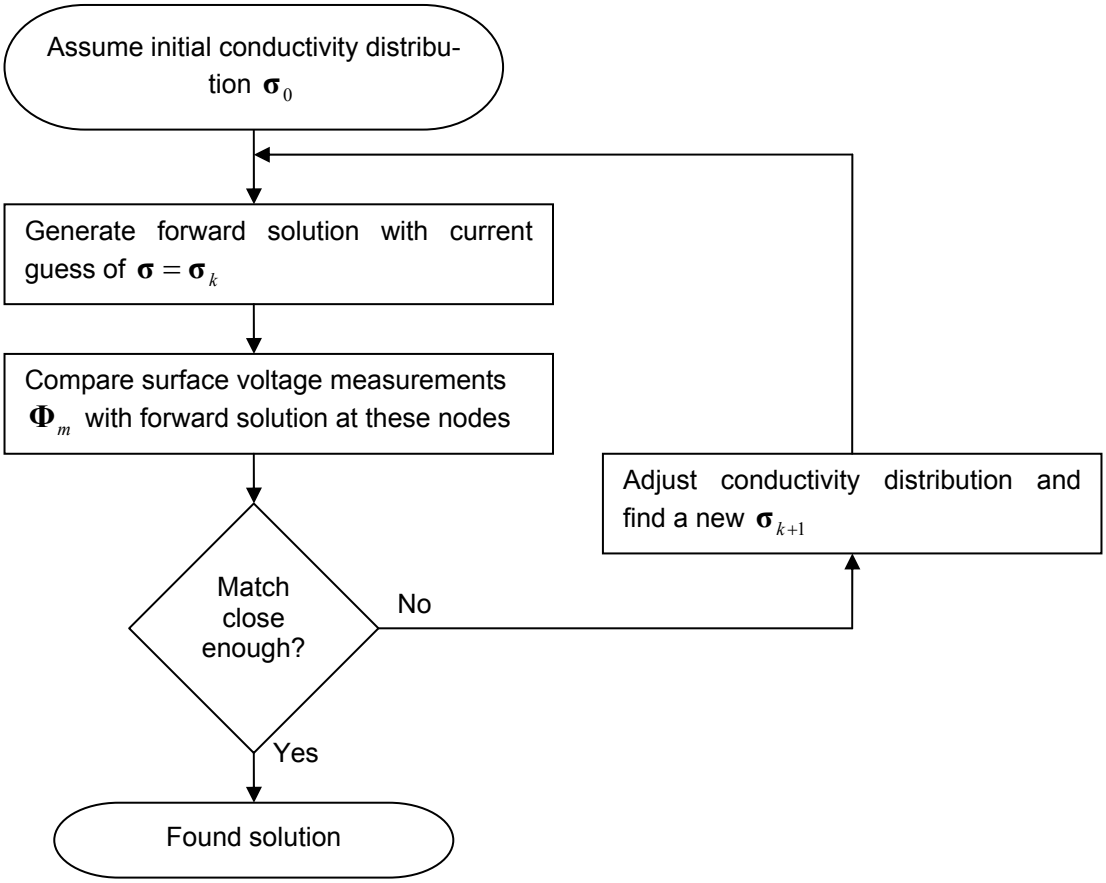

Figure 5.13: Flow diagram of inverse algorithm to determine the conductivity distribution.

The iterative procedure starts with an initial guess σ_0 that is used to generate an initial admittance matrix $\mathbf{Y_0}$. In step k of the iterative procedure, given the conductivity distribution σ_k, we obtain a conductivity correction δ_k estimate as

$$\frac{F_{\sigma_k}(\boldsymbol{\delta}_\mathbf{k})}{\partial \boldsymbol{\sigma}} = \boldsymbol{\Phi}_\mathbf{m} - \boldsymbol{\Phi}(\boldsymbol{\sigma}_\mathbf{k}) \tag{5.30}$$

and set

$$\boldsymbol{\sigma}_{\mathbf{k+1}} = \boldsymbol{\sigma}_\mathbf{k} + \boldsymbol{\delta}_\mathbf{k} . \tag{5.31}$$

Solving this problem lies in minimizing a so-called objective function, which can be written in matrix notation as

$$F(\boldsymbol{\sigma}) = \left\| \boldsymbol{\Phi} - \boldsymbol{\Phi}_m \right\|^2 . \tag{5.32}$$

This procedure uses the gradient to produce subsequent approximations of the conductivity. Since the number of independent measurements is usually not equal to the number of unknowns, we interpret (5.32) in the least squares sense and minimize

$$F(\boldsymbol{\sigma}) = \left(\boldsymbol{\Phi} - \boldsymbol{\Phi}_\mathbf{m} \right)^T \left(\boldsymbol{\Phi} - \boldsymbol{\Phi}_\mathbf{m} \right). \tag{5.33}$$

Since a minimum of the objective function results in a vanishing gradient, we effectively solve for

$$\nabla F(\boldsymbol{\sigma}) = 2\mathbf{J}^\mathbf{T} (\boldsymbol{\Phi} - \boldsymbol{\Phi}_\mathbf{m}) = \mathbf{0}, \tag{5.34}$$

where **J** is the Jacobian matrix of all partial derivatives of $\boldsymbol{\Phi}$ with respect to the conductivities such that

$$\mathbf{J}(\boldsymbol{\sigma}) = \begin{pmatrix} \frac{\partial \Phi_1}{\partial \sigma_1} & \frac{\partial \Phi_1}{\partial \sigma_2} & \cdots & \frac{\partial \Phi_1}{\partial \sigma_n} \\ \frac{\partial \Phi_2}{\partial \sigma_1} & \frac{\partial \Phi_2}{\partial x_2} & \cdots & \frac{\partial \Phi_2}{\partial \sigma_n} \\ \vdots & & & \\ \frac{\partial \Phi_m}{\partial \sigma_1} & \frac{\partial \Phi_m}{\partial \sigma_2} & \cdots & \frac{\partial \Phi_m}{\partial \sigma_n} \end{pmatrix}. \tag{5.35}$$

The dimensions of the Jacobian matrix are determined by the n elements in the mesh M and the m voltage measurement points. The calculation of the differentials used in the Jacobian is usually the most time consuming part of the whole inverse algorithm. The most direct way to calculate these differentials is by using a finite difference approach. However, we realize that this approach requires solving the forward problem for each node in the mesh. As discussed later, there are more efficient ways to calculate the Jacobian.

The Gauss-Newton approach is the most common method to solve such a problem. Given the problem in (5.34), we expand it in a Taylor series around an initial solution $\boldsymbol{\sigma}_k$, resulting in the following representation:

$$\mathbf{J}^{\mathrm{T}}(\boldsymbol{\sigma}_k)\left\{\left[\boldsymbol{\Phi}(\boldsymbol{\sigma}_k)+\mathbf{J}(\boldsymbol{\sigma}_k)(\boldsymbol{\sigma}_{k+1}-\boldsymbol{\sigma}_k)+\mathrm{HOT}\right]-\boldsymbol{\Phi}_{\mathbf{m}}\right\}=\mathbf{0}, \tag{5.36}$$

Here HOT stands for the higher order terms in the Taylor series expansion. The truncation of the higher order terms linearizes the equation. Rearranging (5.36) to solve for σ_{k+1} we get [31]:

$$\boldsymbol{\sigma}_{k+1}=\boldsymbol{\sigma}_k+\left[\mathbf{J}^{\mathrm{T}}(\boldsymbol{\sigma}_k)\mathbf{J}(\boldsymbol{\sigma}_k)\right]^{-1}\mathbf{J}^{\mathrm{T}}(\boldsymbol{\sigma}_k)\left[\Phi(\boldsymbol{\sigma}_k)-\Phi_m\right]. \tag{5.37}$$

Equation (5.37) provides us with a formula to compute the next set of conductivity values at step k+1 given the current approximation at step k and the surface voltage measurements. Convergence criteria can now be used to determine the successful approximation. The convergence criteria can be used on both the residual error and the change of conductivity between two iterations. The safer approach usually is to test the conductivity change between two successive approximations, since the amount of the residual least square depends on the measurement configuration and noise and cannot be predetermined accurately.

5.3.3. Underdetermined versus Overdetermined Problems

With the vast amount of unknowns in the system (the conductivity of every element in the system is unknown) one could expect the system to be under-determined. In an under-determined system, several solutions exist that fit the least squares approximation without any residual error, i.e. more than one conductivity distribution produce the exact same pattern of voltage measurements given an identical current source [55]. Interestingly this is not the case in our EIT problem. It can be shown that for every combination of boundary conditions and voltage measurements only one conductivity distribution exists that fits the situation without residual errors [5, 7, 10]. However, due to the noise in our voltage measurements, we will not be able to find a solution to the inverse problem that fits all boundary conditions exactly.

Overdetermined problems offer too much information to select one consistent solution. This is the case where the least squares algorithm can be used to its full advantage, selecting the one solution in the range of possible solutions that approximates the data with the smallest error. Typically overdetermined problems have more equations than unknowns, although, for reasons mentioned above, it is possible for inherently underdetermined problems to appear overdetermined, even though the number of available equations is fewer than the number of unknowns.

The problem of finding a conductivity distribution that produces a voltage pattern on the surface identical to the measured voltages falls into this category. Due to the measurement noise, uncertainties of probe placements and other imperfections in the measurement setup, the EIT

system behaves like an overdetermined problem. The least squares solution provides the best possible solution with the available data. However, the fact that the number of unknowns in the system – the conductivity at each node – is much larger than the number of available equations renders the problem mainly underdetermined.

Another aspect of underdetermined problems like the inverse algorithm is the non-uniqueness of the solution. In fact, it can be shown that an infinite number of solutions fit the voltage pattern measured on the surface [55]. The use of a priori information and regularization techniques help to steer the algorithm towards the solution that best fits the given requirements.

5.3.4. Regularization and Use of a Priori Information

EIT image reconstruction from surface data is a nonlinear ill-posed inverse problem [16]. This means in practice that large conductivity variations in the center of the volume may result in very low voltage variations on the surface and vice versa. Since the current injection and measurements take place on the surface of the part, the sensitivity to changes in the conductivity at or near the surface is much higher than to changes deeper inside the volume. As a result, the system matrices are usually ill-conditioned with ratios of minimal to maximal eigenvalue on the order of 10^{10} or higher [23, 35]. For these reasons we have to use regularization techniques and/or a priori information in order to achieve a stable solution. The so-called Tikhonov regularization is one way to improve stability and conversion behavior. The inverse problem can so be written in the form [74]

$$\min\left(\left\|\mathbf{\Phi}_m - \mathbf{\Phi}\right\|^2 + \alpha \left\|\mathbf{L}\boldsymbol{\sigma}\right\|^2\right), \tag{5.38}$$

where α is a regularization parameter and **L** is a regularization matrix. This matrix and parameter allow introducing expectancies towards the behavior of the conductivity distribution, such as smooth or slowly changing functions.

Others choose a weighting function which is large for undesirable solutions and thus "penalizes" gradients that move the algorithm in the wrong direction [10]. Again, we have weighting or regularization parameter α that operates on a regularization matrix. It is customary to choose the length of the vector of model parameters, or $\boldsymbol{\sigma}_k^T\boldsymbol{\sigma}_k$, as the regularization vector. The factor is usually found empirically. With these changes (5.37) becomes

$$\boldsymbol{\sigma}_{k+1} = \boldsymbol{\sigma}_k + \left[\mathbf{J}^{\mathrm{T}}(\boldsymbol{\sigma}_k)\mathbf{J}(\boldsymbol{\sigma}_k) + \alpha\mathbf{I}\right]^{-1}\mathbf{J}^{\mathrm{T}}(\boldsymbol{\sigma}_k)\left[\Phi(\boldsymbol{\sigma}_k) - \Phi_m\right]. \tag{5.39}$$

Several different implementation versions of this particular regularization approach exist in the literature [49, 56, 64].

Another approach is to use the a priori information available from the finite element mesh and the knowledge of the expected conductivity variations. Since we do not expect large jumps discontinuities or non-linearities between neighboring elements of the mesh, we can use this information by using a covariance matrix. This covariance matrix relates the conductivities between the elements in the FEM mesh and uses this information to "monitor" the solution process. Also the voltage distribution is not expected to jump by large factors over short distances. This allows introducing a similar covariance matrix for the estimated voltages in the objective function.

Often additional information is available about the expected conductivity of the measured part. Even though the ultimate goal of the method is to detect unknown density, and hence conductivity variations, we usually have a good idea about the expected value of the conductivity of the part. This information can be added to the objective function too, this way improving the system conditioning and aiding the conversion process towards a "reasonable" solution.

Including all this a priori information into our objective function, we can write the objective that needs to be minimized as [78]:

$$F(\boldsymbol{\sigma}) = \left(\boldsymbol{\Phi} - \boldsymbol{\Phi}_{\mathbf{m}}\right)^T \mathbf{C}_{\Phi}^{-1} \left(\boldsymbol{\Phi} - \boldsymbol{\Phi}_{\mathbf{m}}\right) + \left(\boldsymbol{\sigma} - \boldsymbol{\sigma}_{\exp}\right)^T \mathbf{C}_{\sigma}^{-1} \left(\boldsymbol{\sigma} - \boldsymbol{\sigma}_{\exp}\right). \tag{5.40}$$

where $\mathbf{C}_{\Phi}$ stands for the covariance matrix relating the voltages, $\mathbf{C}_{\sigma}$ for the covariance matrix of the conductivity values, and $\boldsymbol{\sigma}_{\exp}$ for the expected conductivity value of the part. The covariance matrices set more weight on the diagonal elements of the global matrix, improving the condition number and hence the accuracy when inverting the matrix. Physically, the use of the covariance matrix represents the smoothness of the conductivity distribution by averaging the solution in neighboring elements and increasing the influence of the solution in a given element to its neighboring elements. By setting the width of the covariance, the required smoothness can be varied, shifting the weight from the most accurate solution to a smoother distribution.

Using this new objective function, we can apply again our inverse algorithm and the gradient method to find a linearized equation for the update of the conductivity after the k-th iteration as [2]

$$\boldsymbol{\sigma}_{k+1} = \boldsymbol{\sigma}_{exp} + \mathbf{C}_{\sigma} \mathbf{J}_k^{\mathrm{T}} \left[\mathbf{J}_k \mathbf{C}_{\sigma} \mathbf{J}_k^{\mathrm{T}} + \mathbf{C}_V\right]^{-1} \left[\boldsymbol{\Phi}_m - \boldsymbol{\Phi} + \mathbf{J}_k \left(\boldsymbol{\sigma}_k - \boldsymbol{\sigma}_{exp}\right)\right]. \tag{5.41}$$

Unfortunately, neither the expected conductivity value nor the covariance of the conductivity is known precisely. First, instead of using the expected value of the conductivity, we resort

back to previous way of using the conductivity $\boldsymbol{\sigma}_k$ from the previous step as our best guess. Second, we can introduce an artificial covariance for $\boldsymbol{\sigma}$. The criterion for this matrix must be to generate full correlation between the element and itself, and degrading correlation for elements as we move farther away from the currently considered element. As a result, the covariance matrix will have all ones on the diagonal, values between 0 and 1 for entries that connect neighboring elements, and 0 everywhere else. This provides for a smooth distribution of the conductivity. This method introduces a normalized covariance matrix that depends on the geometry of the finite element mesh. Since we still do not know the actual variances, the regularization factor in (5.41) is equipped with a regularization parameter α. This factor serves as a multiplier to the regularization term and is adapted in each iteration to achieve convergence. The modified version of (5.41) becomes now:

$$\boldsymbol{\sigma}_{k+1} = \boldsymbol{\sigma}_k + \overline{\mathbf{C}}_\sigma \mathbf{J}_k^{\mathrm{T}} \left[\mathbf{J}_k \overline{\mathbf{C}}_\sigma \mathbf{J}_k^{\mathrm{T}} + \alpha \mathbf{C}_V \right]^{-1} \left[\boldsymbol{\Phi}_m - \boldsymbol{\Phi} \right]. \tag{5.42}$$

where $\overline{\mathbf{C}}_\sigma$ is the artificially created covariance matrix of the conductivity distribution $\boldsymbol{\sigma}$. Marquardt proposes to use $\alpha = 0.01$ in the beginning and to subsequently reduce it in every iteration [49]. For our purposes, a starting value of $\alpha = 0.1$ seemed more appropriate to achieve satisfactory performance of the algorithm.

The use of a priori information and regularization techniques is a common tool in solving least squares problems. In fact, the form of Equation (5.42) resembles the Kalman filters encountered in communication applications. Although applied to a different problem set, the Kalman filter iteratively solves a discrete data linear filtering problem using a least squares approach.

5.3.5. Efficient Calculation of Jacobian

A major part of the computational complexity in calculating the inverse solution is the generation of the Jacobian matrix **J**. According to (5.37) the iterative solution process requires the calculation of the **J** with a new value for the conductivity for every iteration.

The Jacobian matrix is a sensitivity matrix that contains the gradient of the observed system parameter with respect to one or several unknowns. In our particular case, each element in **J** can be calculated as

$$J_{ij} = \frac{\partial \Phi_i}{\partial \sigma_j}. \tag{5.43}$$

As we shall see later, the basic approach to calculate **J** requires generating a forward solution for each element in the finite element mesh. As one can imagine, the task of calculating one Jacobian can already become very time consuming for large mesh sizes. The fact that we have to recalculate the Jacobian in every iteration renders the calculation of **J** the true bottle neck in generating our solution. Since this problem of calculating the Jacobian of a system arises in many parameter estimation problems in many scientific applications, finding the most efficient way of calculating **J** has become a field of study of its own. Without reviewing this subject into too much detail, two methods of calculating **J** will be presented: the basic differentiation method and an optimized method according to Geselowitz' sensitivity theorem that reduces calculation time considerably [80]. One way to avoid this problem entirely is to resolve to a non-iterative solution. A number of researchers have tried this approach [13, 27, 56, 80], but usually with limited success. In these cases accuracy is directly traded for reduction in solving time.

The first method to calculate **J** is by using the definition as given in (5.43). Using the forward solution to generate the voltage values in the volume, we get for one entry in the Jacobian

$$J_{ij} = \frac{\partial \Phi_i}{\partial \sigma_j} = \frac{\partial (\mathbf{Y}^{-1}\mathbf{I})_i}{\partial \sigma_j}. \tag{5.44}$$

For a more compact representation and easier mathematical treatment, we realize that one column of **J** can be calculated at a time by using vector notation. Using this vector notation and rewriting (5.44), we find for the j-th column of the Jacobian

$$\mathbf{J_j} = \mathbf{Y}^{-1} \frac{\partial \mathbf{Y}}{\partial \sigma_j} \mathbf{\Phi}. \tag{5.45}$$

Referring back to the definition of **Y** as the collection of conductivities of all elements in the mesh, we can easily calculate a discrete version of $\partial \mathbf{Y} / \partial \sigma_j$. Since a change in the conductivity only affects the local 4x4 matrices of the tetrahedral elements, we realize that the differentiation $\partial \mathbf{Y} / \partial \sigma_j$ of the global matrix **Y** is zero for all entries except the 16 that contain the change according to $\partial \mathbf{y_j} / \partial \sigma_j$ of the local matrices.

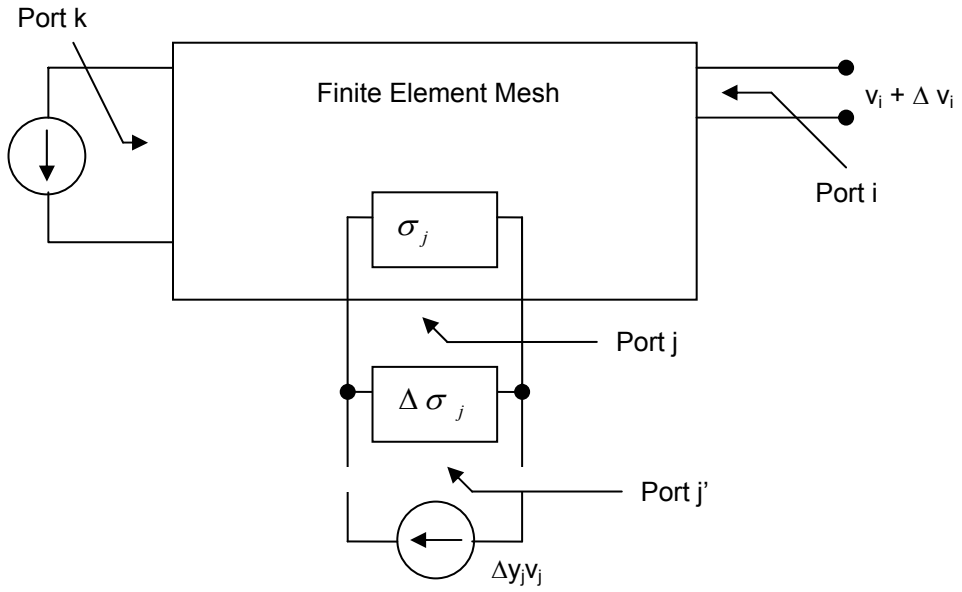

Figure 5.14: Illustration of Geselowitz' sensitivity theorem.

This method is very straightforward and intuitive to understand. Its big drawback is the fact that it automatically calculates the entries in J for each element in the mesh. Consequently, J is an $n \times n$ matrix, with n being the number of elements in the finite element mesh. As one can imagine, the time to calculate this matrix as well as the memory space to store it become almost unmanageable. The penalty of this method becomes even more obvious when one realizes that, after having calculated all the elements in J, we will only pick out and use the ones that coincide with the measurement points on the surface. The remaining entries are not needed and are discarded.

The method based on Geselowitz' sensitivity theorem avoids the calculation of the unneeded entries into the Jacobian and is therefore computationally much more efficient [25, 79]. This theorem, also called the compensation theorem, relates a change in measured voltage to a conductivity change inside a continuous medium. This is done as follows: at an arbitrary port k a current is injected into the volume. Given a conductivity distribution within the volume, this current produces a voltage v_i at port i that is measured. Changing the conductivity at port j from σ_j to $\sigma_j + \Delta\sigma_j$ creates a new port j', which affects the measured voltage at port i, so that it becomes $v_i + \Delta v_i$. Figure 5.14 illustrates the setup used to explain this theorem. If we consider a transfer

impedance z_{ij} between ports i and j, we can write the mathematical formulation for the voltage change occurring at port i as

$$\Delta v_i = -c_k \Delta\sigma_j z_{ij'} z_{kj} . \tag{5.46}$$

With the superposition principle, we can now include the change in measured voltage that occurs at port I for each of the elements in the mesh. Here we note that only ten ports are affected by a change in conductivity of a single tetrahedral element. These are the ports formed by any two nodes of the tetrahedron (effectively the edges) and of each node to the ground node. As a result, the total change in measured voltage at port i from a change of conductivity in a single element can be calculated as

$$\Delta v_i = -c_k \sum_{l=1}^{10} \Delta\sigma_{j(l)} z_{ij(l)'} z_{kj(l)} . \tag{5.47}$$

Using the finite element coefficients stored in the $\mathbf{s_e}$ matrices defined in section 5.2.5 removes the conductivity from the summation. Furthermore, since we are interested in the derivative of v_i with respect to $\Delta\sigma_j$, we let $\Delta\sigma_j \to 0$. Additionally substituting z=v/c, (5.47) becomes:

$$\frac{\partial v_i}{\partial \sigma} = -\frac{1}{c_k} \sum_{l=1}^{10} s_{j(l)} z_{ij(l)} z_{kj(l)} . \tag{5.48}$$

We note that by applying only an infinitesimal change $\Delta\sigma_j$, port j' becomes equal to port j and the prime can be dropped.

Further simplification of the expression in (5.48) is possible by using matrix notation. We can consider to calculate the nodal voltage with the source at its original location of port k using the FEM solver, and then changing the source between node i and ground to calculate the nodal voltages again. Subsequently the expression for the change of v_i with respect to σ_j becomes [9]:

$$\frac{\partial v_i}{\partial \sigma} = -\frac{1}{c_k} \mathbf{\Phi_k^T s_e \Phi_i} . \tag{5.49}$$

where $\mathbf{s_e}$ is the matrix of FEM coefficients for element e. $\mathbf{\Phi}_k$ is the vector of nodal voltages at the element under investigation for the "normal" placement of the current source at port k, $\mathbf{\Phi}_i$ is vec-

tor with the nodal voltages for this same element with the current source placed between node i and ground.

The computational complexity of calculating the Jacobian can be estimated by taking into account the number of forward solutions that are needed to assemble it. As we saw earlier, the direct method requires generating one forward solution for each element in the mesh. Using the sensitivity approach, we only calculate the entries in the Jacobian that correspond to measurement points on the surface plus one additional solution for the original placement of the current source. Since the number of measurement points is usually much smaller than the number of elements in the mesh, this method is faster by several orders of magnitude.

An additional increase in computational speed can be achieved by approximating the Jacobian by the use of Broyden's method [60, 67]. When derivatives are not available or are costly or difficult to calculate, the Jacobian matrix can be approximated by a finite-difference approximation. The remarkable feature of Broyden's method is that it is able to generate a reasonable approximation to the Jacobian matrix with no additional evaluations of the function or, in our case, the finite element solution.

Broyden's method is a generalization to the secant method for non-linear system which replaces the derivative by a finite difference. Using finite differences, the approximated Jacobian $\mathbf{J}_k^a$ in iteration k becomes

$$\mathbf{J}_k^a = \frac{\mathbf{\Phi}(\sigma_k) - \mathbf{\Phi}(\sigma_{k-1})}{\sigma_k - \sigma_{k-1}}. \tag{5.50}$$

Since (5.50) provides only n equations to determine the $n \times n$ matrix, the "best possible" approximation is a minimal modification of $\mathbf{J}_{k-1}^a$. Using

$$\Delta\mathbf{\Phi}_\mathbf{k} = \mathbf{\Phi}(\boldsymbol{\sigma}_k) - \mathbf{\Phi}(\boldsymbol{\sigma}_{k-1}), \qquad \Delta\boldsymbol{\sigma} = \boldsymbol{\sigma}_k - \boldsymbol{\sigma}_{k-1} \tag{5.51}$$

we find for $\mathbf{J}_k^a$

$$\mathbf{J}_k^a = \mathbf{J}_{k-1} + \frac{\Delta\mathbf{\Phi}_k - \mathbf{J}_{k-1}\Delta\boldsymbol{\sigma}_k}{\Delta\boldsymbol{\sigma}_k^T \Delta\boldsymbol{\sigma}_k} \Delta\boldsymbol{\sigma}_k^T. \tag{5.52}$$

This approach allows calculating the Jacobian for step k with only one forward finite element solution – the one that is required to calculate the nodal voltages with the current conductivity distribution – the knowledge of the changes in the solution that occurred in the previous step

and the previous Jacobian. However, since this method is only an approximation to calculating the true Jacobian, the convergence behavior may deteriorate after too many iterations. Since the method uses the previous Jacobian to calculate the new one, any error that the approximation introduces is carried on and, after too many iterations, may accumulate to unacceptable amounts. The solution we adopted was therefore to calculate the Jacobian using the sensitivity theorem in the first iteration in order to get an exact starting point, and then update it using Broyden's method in the subsequent operations. Depending on the number of iterations it is advisable to recalculate the Jacobian completely every six to ten iterations to avoid unacceptable error accumulation.

5.4. Application of EIT to P/M parts

The application of EIT to P/M parts, which has not been used before, generally follows the same rules as for any other application as mentioned above. A few special considerations about the specific goal have to be taken into account, though.

The application of EIT requires any material that is to be investigated to be electrically conductive to some degree. Since the main material in P/M parts is some kind of metal, this requirement is usually easily fulfilled. In fact, the conductivity in these metal compacts can reach such high levels, that practical measurements become difficult again. Since the measurement procedure records voltage differences occurring due to the source current flowing through a compact, a very high conductivity results in only small voltage drops. This is the main reason why the application of this method to sintered P/M parts is more difficult. Sintering increases the conductivity by approximately three orders of magnitude, resulting in voltage differences that are three orders of magnitude smaller. Increasing the source current would naturally take care of this problem again, but since we are using currents on the order of 1A, increasing the current by three orders of magnitude would result in current strengths of 1kA. In general we can say that the relatively high conductivity of the P/m parts require high currents and result in only small voltage drops on the surface of the part.

Another important fact to keep in mind is that we do not expect the density of the P/M part, and therefore its conductivity, to change drastically over small regions. This means we are not interested in finding local disturbances as they would occur in the vicinity of a crack or inclusion. The goal of this procedure is to measure macroscopic density variations over large areas of the part. As a result, we have different requirements to our reconstruction algorithm than applications that intend to identify separate sub-volumes with completely different electric properties. Such applications, like medical EIT, would like to enhance edge detection, where the exact location of a conductivity change can be determined. In our case, the opposite is true. Since we know

that the density in the compact does not change drastically over a small distance, we actually apply the above mentioned smoothing function. This enhances the reconstruction algorithm and improves convergence by using the appropriate prior information.

Another important consideration for the application of EIT to green state P/M parts is the fact that we are often not really interested in finding the exact location of a high or low density area. In fact, the detection of the presence of such an area within the part is usually sufficient. Therefore we often can apply simplified algorithms and measurement procedures that will not generate the same amount of detail in the result, but rather compare the characteristics of two parts based on the voltage measurements.

6 Density Measurements

6.1. Algorithm

The density measurements build upon all the previously introduced concepts. The theory of three dimensional current flow is required to enhance the current injection pattern and understand the limitations of the method. The EIT algorithm is used to calculate the conductivity distribution throughout the volume of the green-state P/M compact, based on known sources and the surface voltage measurements. Finally, the previously recorded conductivity – density relationship for the particular powder mixture allows the conversion of the reconstructed conductivities into a density map.

Due to the fact that the conductivity – density relationship for lubricated P/M samples is not linear, it even exhibits a local maximum, the correlation between the reconstructed conductivity and the density of these samples is ambiguous. This led to the concern that the method may not be employed for such parts, since it is not known which density corresponds to a given conductivity. However, forma practical point of view there is always sufficient prior information about the measured compacts available to generate an algorithm that renders the mapping unique.

The nominal density provides the starting point for this mapping algorithm. Given a specific conductivity for the given element, we would usually have to make a choice between two corresponding densities, as previously illustrated in Figure 4.21. Assuming that the real density is close to the expected nominal density, we select the value that is closer to the nominal density. There might still be an ambiguity, for example if the nominal density lays exactly half way between the two possible selections. Here again we can include prior information to finally make the correct decision. Depending on the press process, tonnage and powder mixture used to produce the compact, we should have a good idea whether the density at the particular location can be significantly higher or lower than the overall nominal density.

Having selected the correct density value corresponding to the measured conductivity for the first element, we can now proceed to the next step. Considering the two choices we are pre-

sented with for the neighboring element, it is obvious that it will exhibit a value that varies only slightly from the density of the element where the algorithm started. The selection of the correct density for this element is therefore straightforward. Proceeding in this manner throughout the volume, the conductivities can be mapped into corresponding densities for each element, always taking into account the previously assigned densities of its nearest neighbors.

Additional difficulties occur when the varying density moves across the inversion point from higher to lower densities or vice versa. Although the method is not recommended for use in such situations, increasing the complexity of the mapping algorithm will resolve most ambiguities in such cases. Instead of considering only the value of the density in the neighboring elements when making the selection, we now have to consider the local density gradient too. This requires monitoring not only the absolute value, but also the relative changes in the close neighborhood of the currently investigated element. Assuming that the trend in the local density variation continues, the addition of this information allows us again to make the correct choice and select the appropriate density value.

6.2. Measurements of Simple Parts

The new method of testing green state P/M compacts together with the inverse algorithm was first tested for the geometrically simple cylindrical shapes that we previously analyzed using the exact solution to Laplace's equation. Assuming piece-wise constant densities along the length of the cylinder, this geometry was chosen to allow us to validate the results obtained by the algorithm by comparing them to results obtained from conventional methods.

6.2.1. Parts and Measurement Setup for Density-Reconstruction

A new set of green state P/M parts was needed to measure density variations. Contrary to the parts used for conductivity measurements (which were wide and flat to achieve a density distribution that was as uniform as possible) the new parts needed to be long and slim. Since the goal was to measure density variations, parts with a "built-in" density gradient were the most obvious choice. Samples of aspect ratios of approximately 4:1 (length:diameter) would inherently exhibit significant changes in density from top to bottom, even more so when pressed in a single punch process.

We were able to obtain two sets of parts, of which especially the set provided by GKN Worcester proved to be exactly formed in the required aspect ratio. These cylindrical green-state compacts, shown in Figure 6.1, were 2.75" to 3.25" inches long and all had a radius of 0.75". Us-

ing the same powder mixtures that were used to press the flat disks used in the investigation of the density-conductivity relationship, the green samples had the following properties:

- iron 1000B as base material,
- four different sets of parts with no lubricant (die wall lubricated), 0.3% AWX, 0.5% AWX and 0.75% AWX respectively,
- each set with 7 to 8 parts of different pressures, ranging from 25 tsi to 55 tsi
- single punch pressing (to increase density gradient)

Figure 6.1: Green state P/M samples of length of 3" with length-to-width ratio of 4:1, used for measurement of density gradient.

The above parts were contacted in the same way as the previous samples during conductivity measurements, injecting a direct current of 1A from top to bottom and recording the voltages along the surface. However, this time we did not take an integral voltage measurement over the entire length of the part, effectively averaging all possible density variations, but rather measured the voltage drop over small slices of 0.25" each (see Figure 6.2 for the basic measurement arrangement).

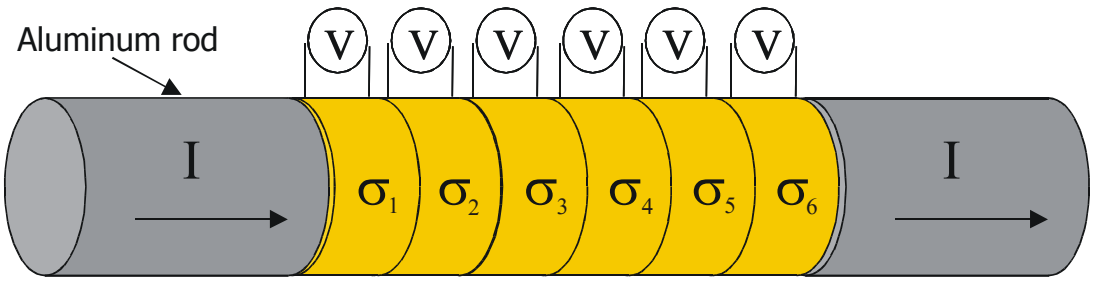

Figure 6.2: **Measurement setup for the recording of density variations over the length of a green state P/M rod. A controlled DC current is injected and the voltage on the surface is recorded on several slices of 0.25" thickness each.**

In such a setup, the conductivity, and hence the density, are considered constant over the measured length of 0.25". While this is obviously only an approximation (since it effectively averages the density over the measured length), it provides the means for a straight forward re-construction of the conductivity and the corresponding density. Since the constant current I is forced through each of the slices and the resulting current density is homogeneous throughout the volume, the conductivity can be calculated from the measured voltage V_i and the geometrical measures of the measured length *L* and the cross-section *A* as

$$\sigma_i = \frac{I}{V_i}\frac{L}{A}, \tag{6.1}$$

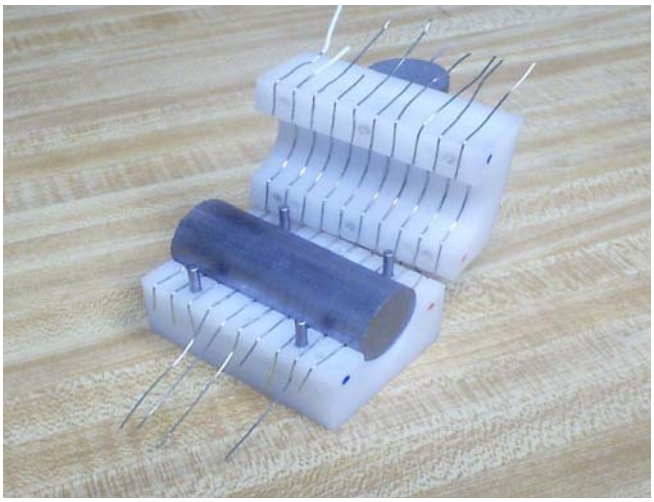

Figure 6.3: **Sensor developed for density measurements on long, thin cylinders.**

6.2.2. Measurement Results

The results of the voltage measurement on the surface of the long, thin green state P/M rods show a distinct change in conductivity over the length of the part. For a uniform conductivity distribution, the voltage drops by the same amount for each measured slice. Hence, changes in conductivity will manifest themselves in a change of these voltage differentials.

Even with the limited resolution of 0.25" for our first measurements, a conductivity and hence a density distribution is apparent. Furthermore, the difference in the conductivity – density relationship between non-lubricated parts and the parts with 0.75% AWX becomes apparent when compared to the results from the voltage measurements made on parts from different powder mixtures. While the density distribution in both sets is expected to be similar, changes in the voltage difference clearly indicate different behavior due to the linear and non-linear conductivity-density relationship, respectively. Figure 6.4 shows the monotonically increasing voltages measured for non-lubricated parts. In the lubricated parts on the other hand, we find a very slow increase, if not even a decrease of the voltage near the top of the part (where we expect to find the highest green state densities), with the expected monotonic increase following for the lower part. This again reflects the conductivity – density relationship in lubricated parts, which exhibits a maximum conductivity between densities of 6.8 and 7.0 g/cm. The voltages recorded for the parts lubricated with 0.75% AWX are depicted in Figure 6.5.

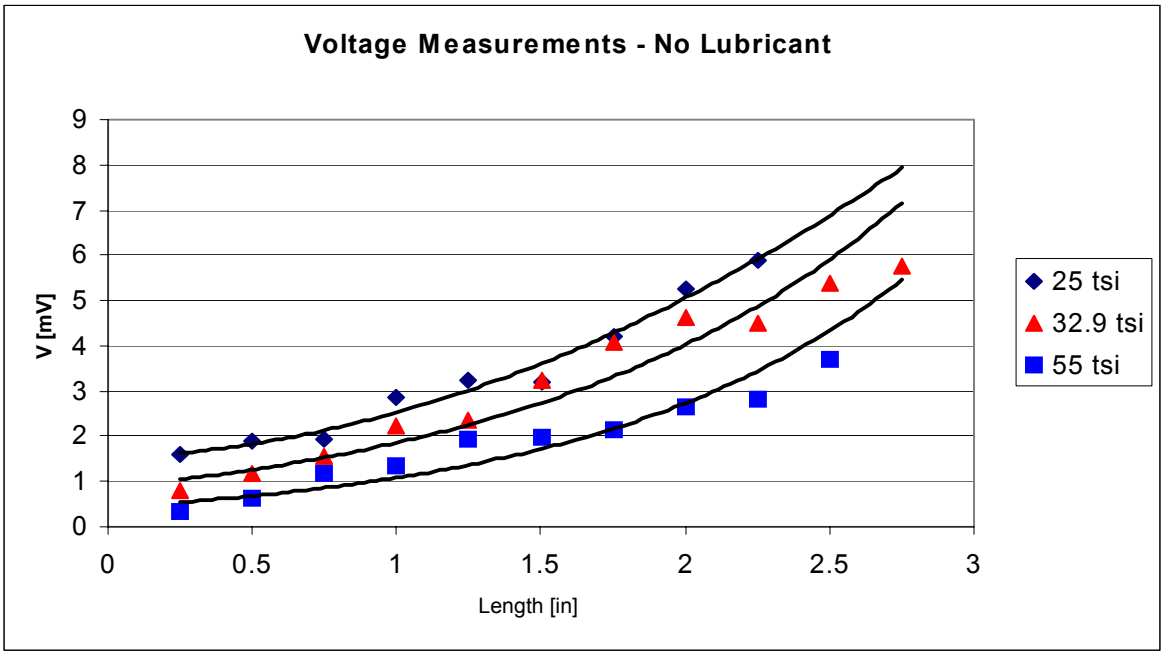

Figure 6.4: **Voltage measurements on slices of non-lubricated green state samples of various initial densities. The press tonnage ranges from 25 tons per square inch (tsi) to 55 tsi.**

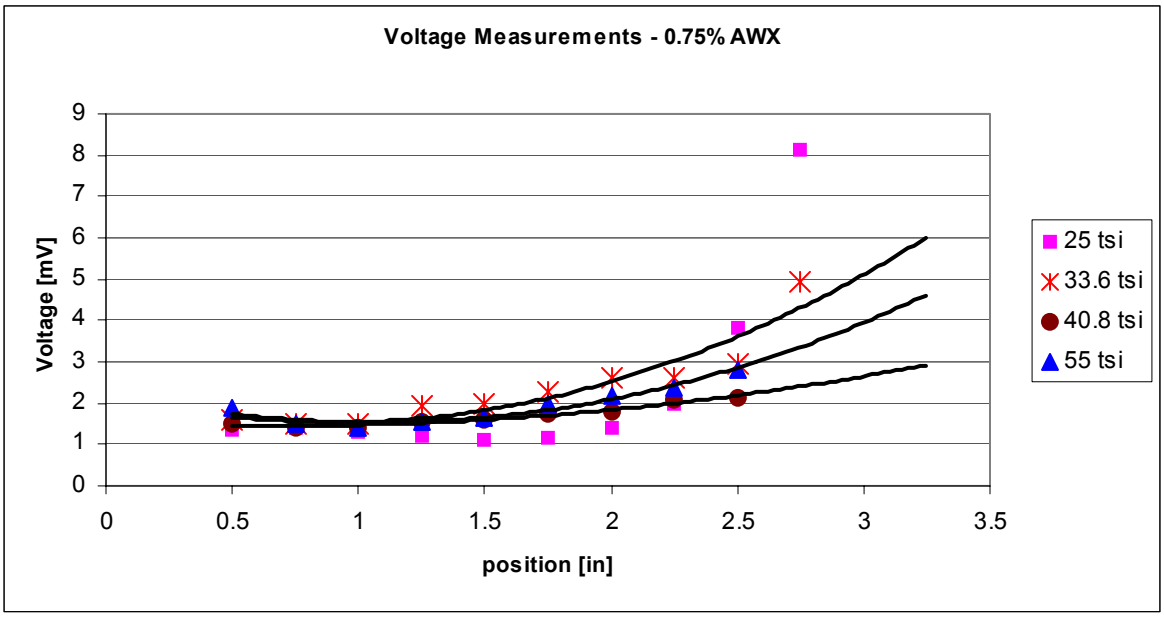

Figure 6.5: **Voltage measurements on slices of green state samples of various initial densities, lubricated with 0.75% AWX.**

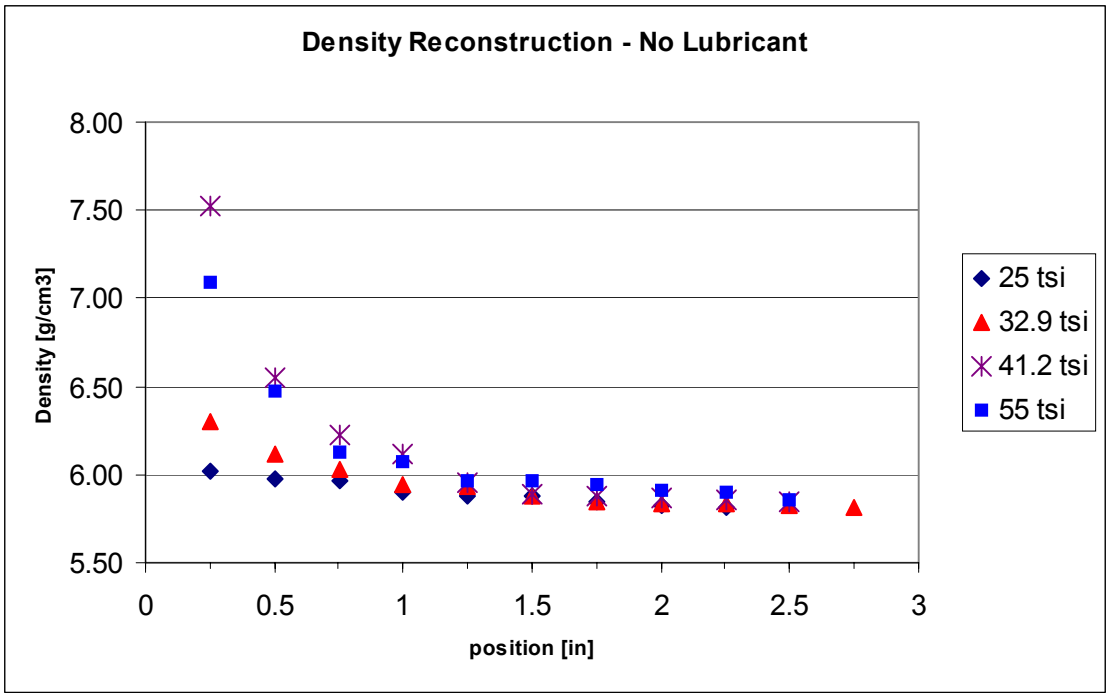

Figure 6.6: **Reconstructed density distribution over the length of the non-lubricated green state P/M rods. Highest densities are found at the top, lowest at the bottom of the parts (single punch pressed).**

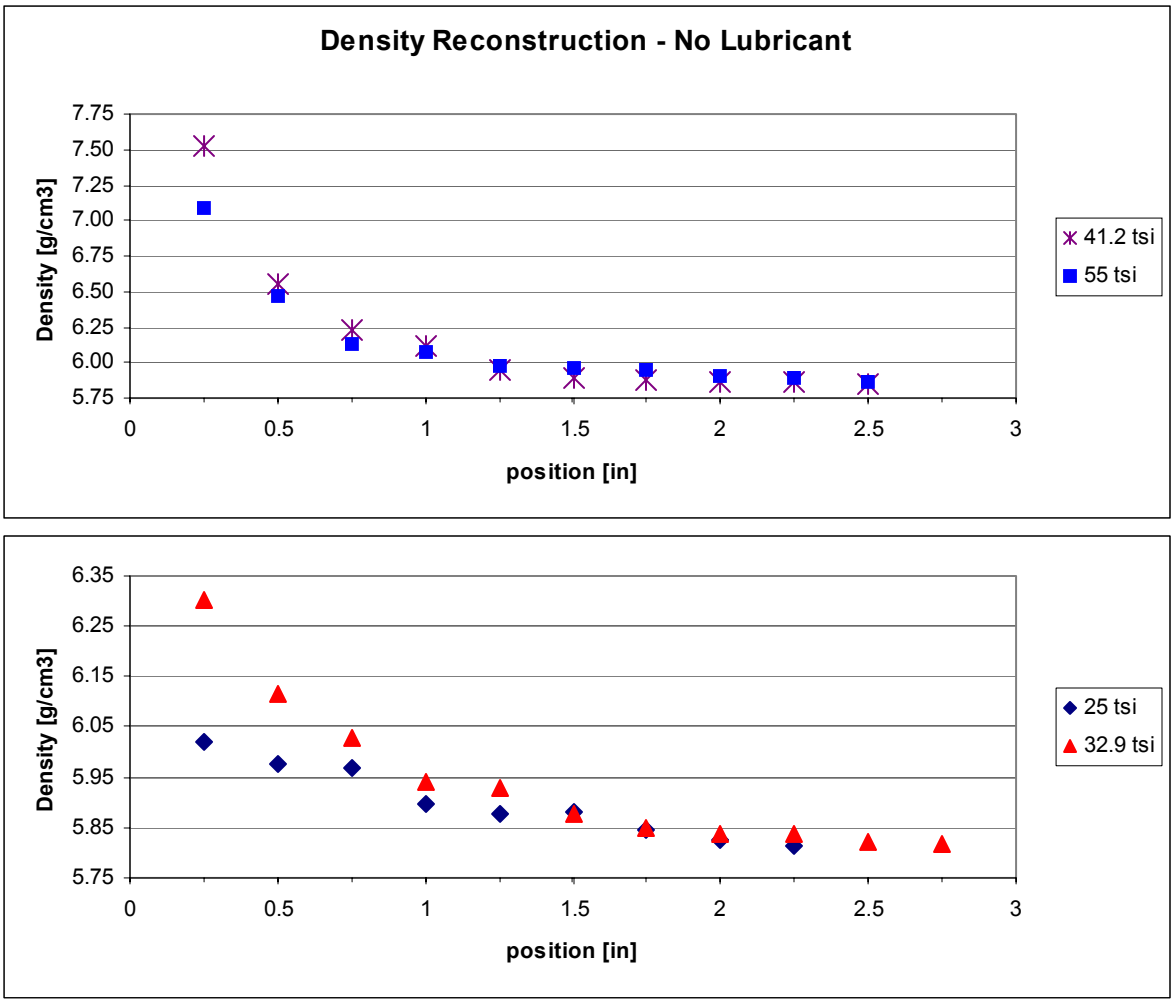

Figure 6.7: **Reconstructed density distribution over the length of the non-lubricated green state P/M rods (same as in Figure 6.6). The separation of the high and low pressure parts into separate diagrams allows rescaling of the axis. This demonstrates the same inherent density distribution in the four different parts.**

Using the previously recorded relationship between the conductivity of pressed powder and its density, we can now reconstruct the density distribution over the length of the parts. This reconstruction is especially straight forward in case of non-lubricated parts, where the relationship is linear. Here every conductivity can be directly mapped into a corresponding density. The reconstructed densities for compacts produced at four different pressures are shown in Figure 6.6. The in this way reconstructed distribution indicates that the densities at the bottom of the parts are the same, regardless of the pressure used. On the other hand, the calculated densities at the top, where the press contacts the powder, correlate directly with the amount of pressure used.

Figure 6.7 provides the same data as presented in Figure 6.6, but the high and low pressure parts have been separated to allow rescaling of the axis. This way we recognize the same inherent behavior of the density distribution in high and low-pressure parts.

The densities for the lubricated parts can be reconstructed in much the same way, with the only additional requirement that the algorithm must be somewhat intelligent to discriminate between densities above and below the inversion point as discussed in Section 6.1. The results of this reconstruction are presented in Figure 6.8. As we can see, the parts exhibit a higher density than the non-lubricated counterparts when pressed with the same tonnage. Also the density distribution seems to be more linear with no leveling off towards the bottom of the part.

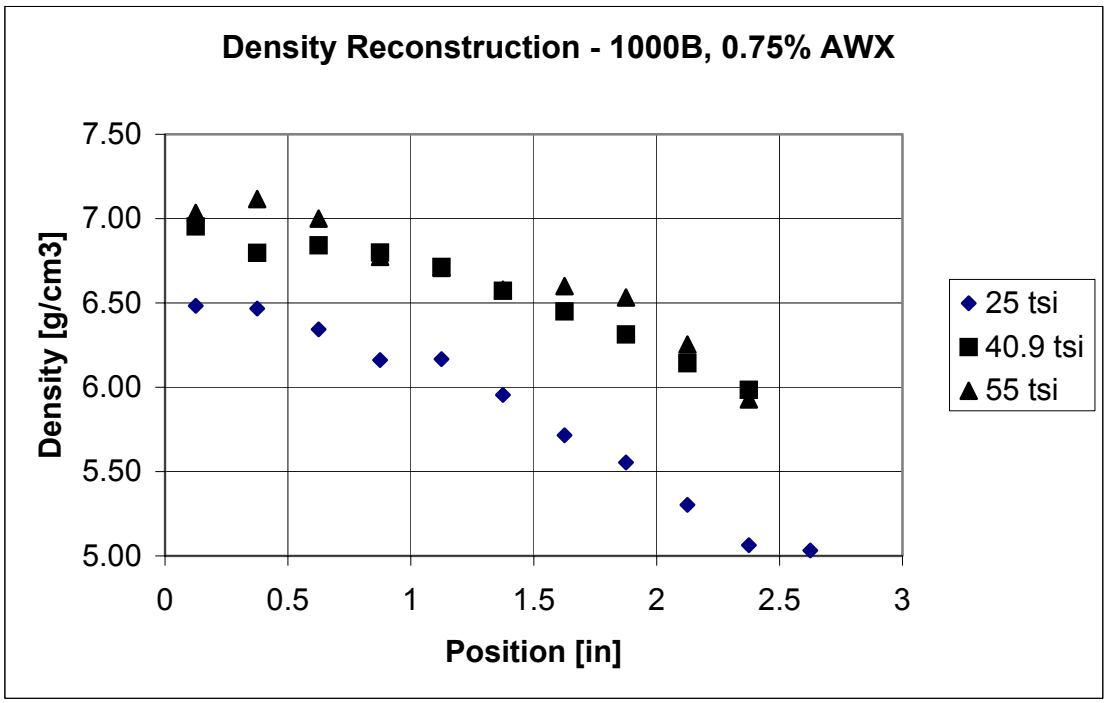

Figure 6.8: **Reconstructed density distribution over the length of green state P/M rods pressed from iron 1000B with 0.75%AWX. Highest densities are found at the top, lowest at the bottom of the parts (single punch pressed).**

6.2.3. Comparison with Conventional Methods

In order to verify the density distribution obtained from the conductivity measurements, destructive density measurements were performed on the previously analyzed samples. The samples were cut into 0.25" thick slices, exactly the same spacing used as for the non-destructive density reconstruction. These slices, shown in Figure 6.9, were then weighed on a precision balance. Together with the calculated volume, the weight allowed to obtain an average density for

each slice. The results of these comparative, destructive measurements are shown in Figure 6.10 and Figure 6.11 for non-lubricated samples and for samples with 0.75%AWX lubricant respectively. In both cases we find a nearly linear decrease of the density from the top to the bottom of the sample, which seems to flatten out at a minimum of about 5 g/cm^3, independent of the specific lubricant amount or applied pressure.

The preparation of the cylinders into small, cross-sectional slices allowed testing another aspect of the conductivity-density relationship. Some concern was raised by possible lubricant migration during compaction. This lubricant migration, it was reasoned, could lead to an accumulation of non-conducting particles towards the surface. Upon close examination of the individual slices no such lubricant accumulation at the circumference could be observed.

Figure 6.9: Green state P/M rod sliced into 0.25' thick pieces for density measurements.

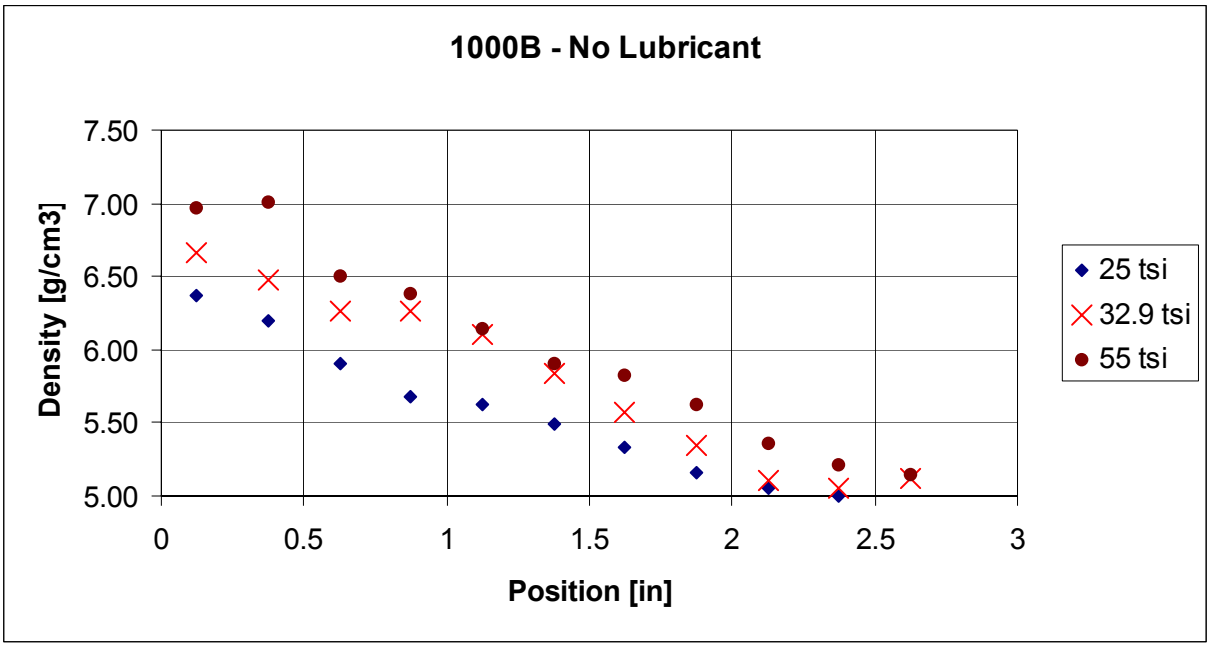

Figure 6.10: **Density distribution over the length of green state P/M parts pressed at different nominal pressures from iron powder 1000B without lubricant.**

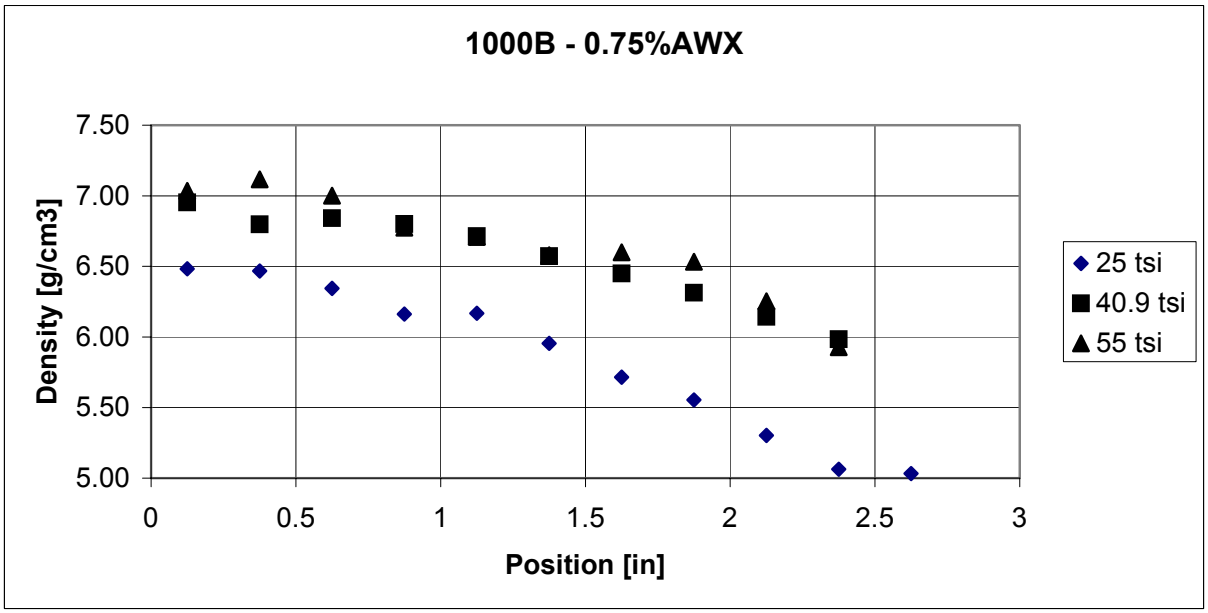

Figure 6.11: **Density distribution over the length of green-state P/M parts from iron powder 1000B with 0.75% AWX lubricant with different nominal pressures.**

Figures 6.12 to 6.14 compare the density values that were reconstructed from our conductivity measurements to actual density values obtained from the sliced samples. Not surprisingly, the numbers do not match exactly, but the correlation between the data sets recorded with the two different methods is striking. Several interesting observations can be made which explain the presented data:

- It is obvious that whenever the real density (as measured on the sliced samples) falls below 6.0 g/cm^3, the reconstruction from the non-destructive measurements does not work properly anymore. This is true for both lubricated and non-lubricated parts. It can be attributed to the fact that our conductivity – density baseline does not contain data below this density point. Apparently the extrapolation beyond this point as assumed for the reconstruction at hand is not valid. Establishing an extended baseline would solve this problem.
- For densities above 6.0 g/cm^3 the reconstructed density is close to the actual values found on the sliced samples. Even more striking is the similarity of the density changes over the length of the parts. This observation stresses once more the fact that our method delivers reasonable absolute numbers, the real value of the method, however, lies in comparative measurements against an established baseline. It is not the goal of this method to accurately measure absolute density values but to detect variations of density within parts and from one part to the next.
- Figure 6.14 shows the data comparison for non-lubricated green state P/M parts down to a density of 6.0 g/cm^3. On this scale we recognize that, indeed, the reconstructed density data closely tracks the real density in the region where baseline data is available.
- The close tracking of the density variation obtained from the two different methods can be observed in Figure 6.12 for lubricated and in Figure 6.13 for non-lubricated samples. The close results indicate that the method works equally well for lubricated parts as for the non-lubricated parts, even though the conductivity-density relationship is not linear in the first case. The presented algorithm relating the conductivity measurements to density values works flawlessly as demonstrated in these curves.

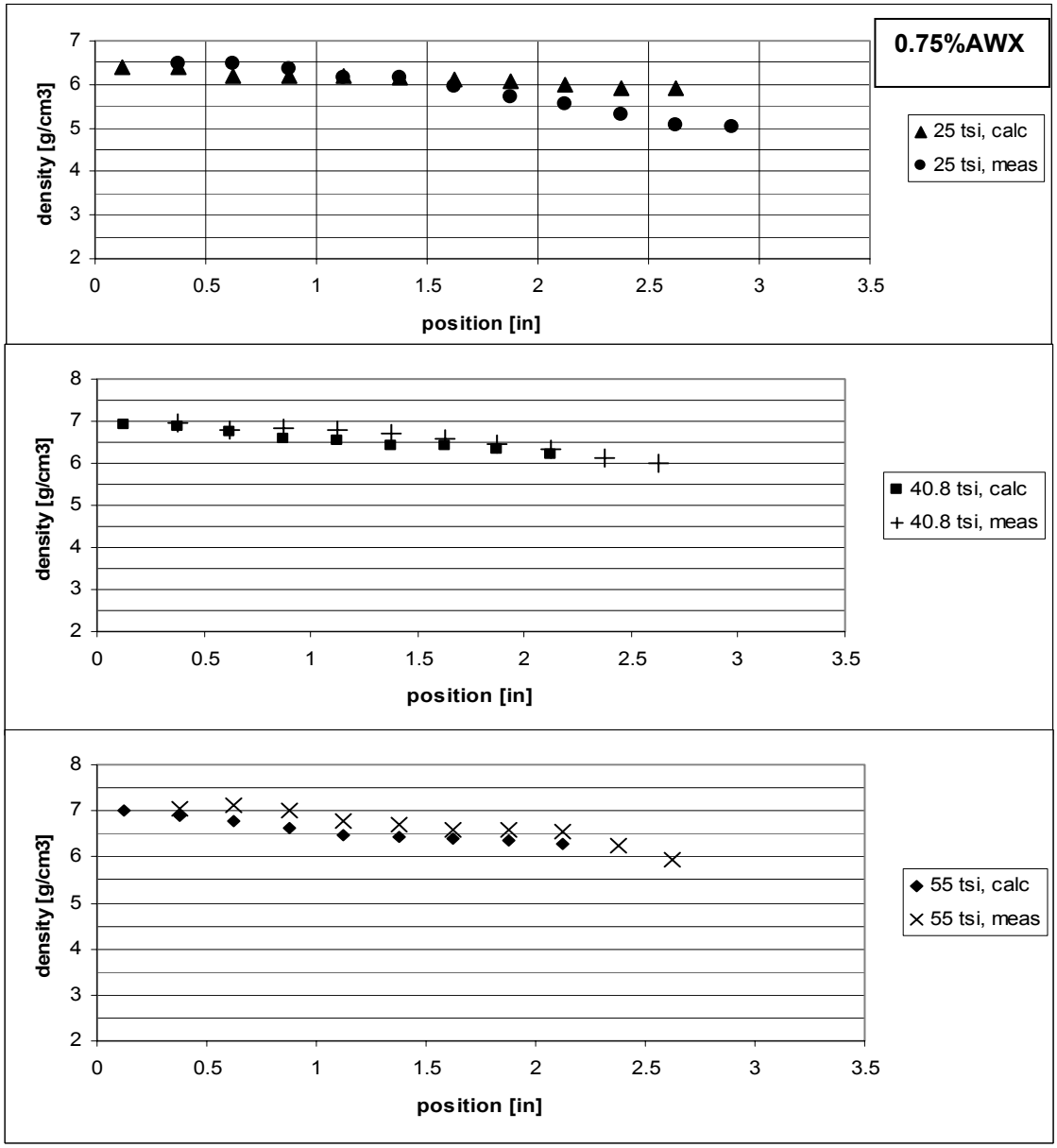

Figure 6.12: **Comparison of density values obtained from predictive and destructive testing respectively. Results shown are for green state P/M parts made from 1000B powder with 0.75% AWX lubricant at three different nominal pressures: a) 25 tsi, b) 40.8tsi, c) 55 tsi.**

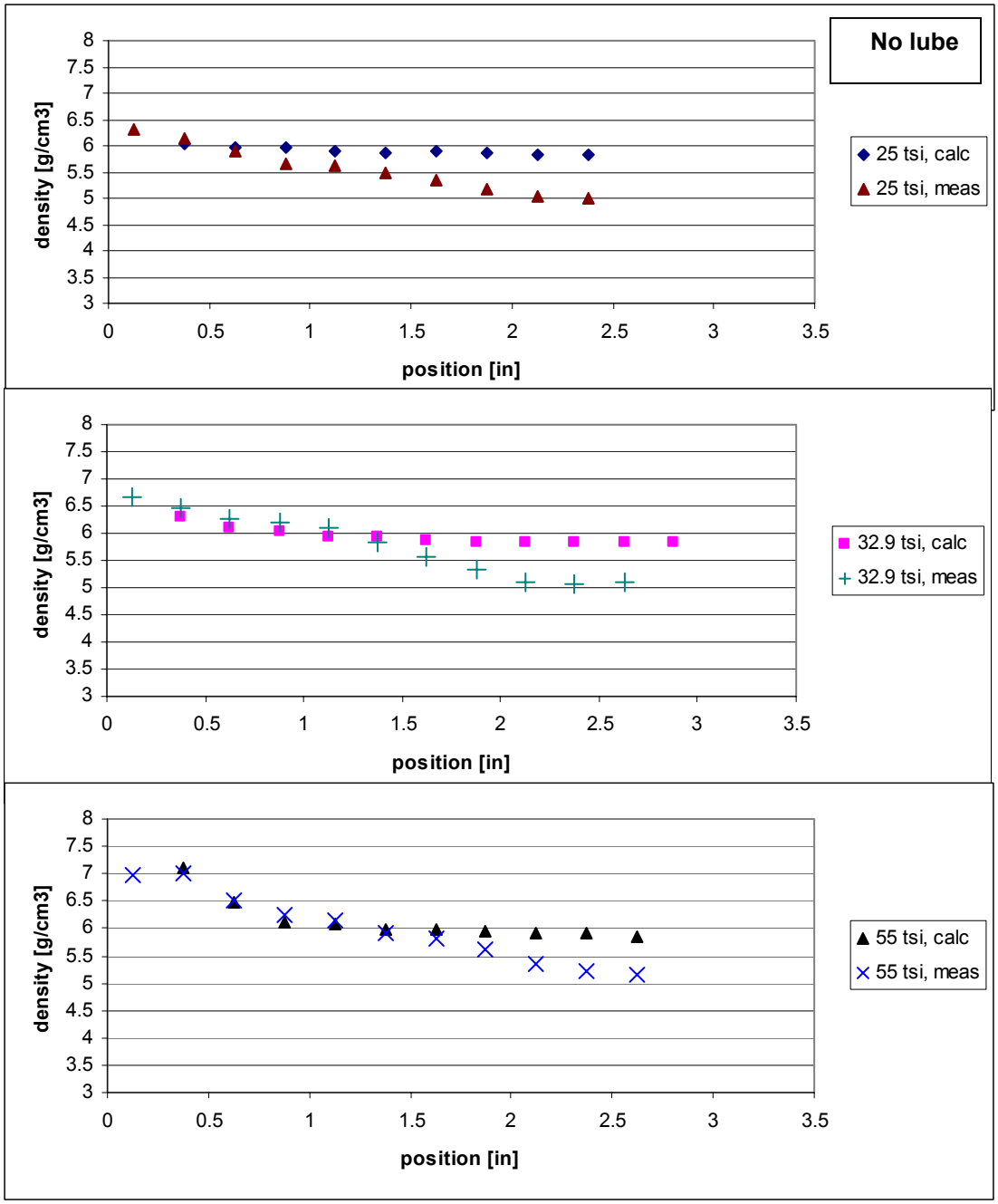

Figure 6.13: **Comparison of density values obtained from reconstruction and destructive testing respectively. Results shown are for green state P/M parts made from 1000B powder without lubricant.**

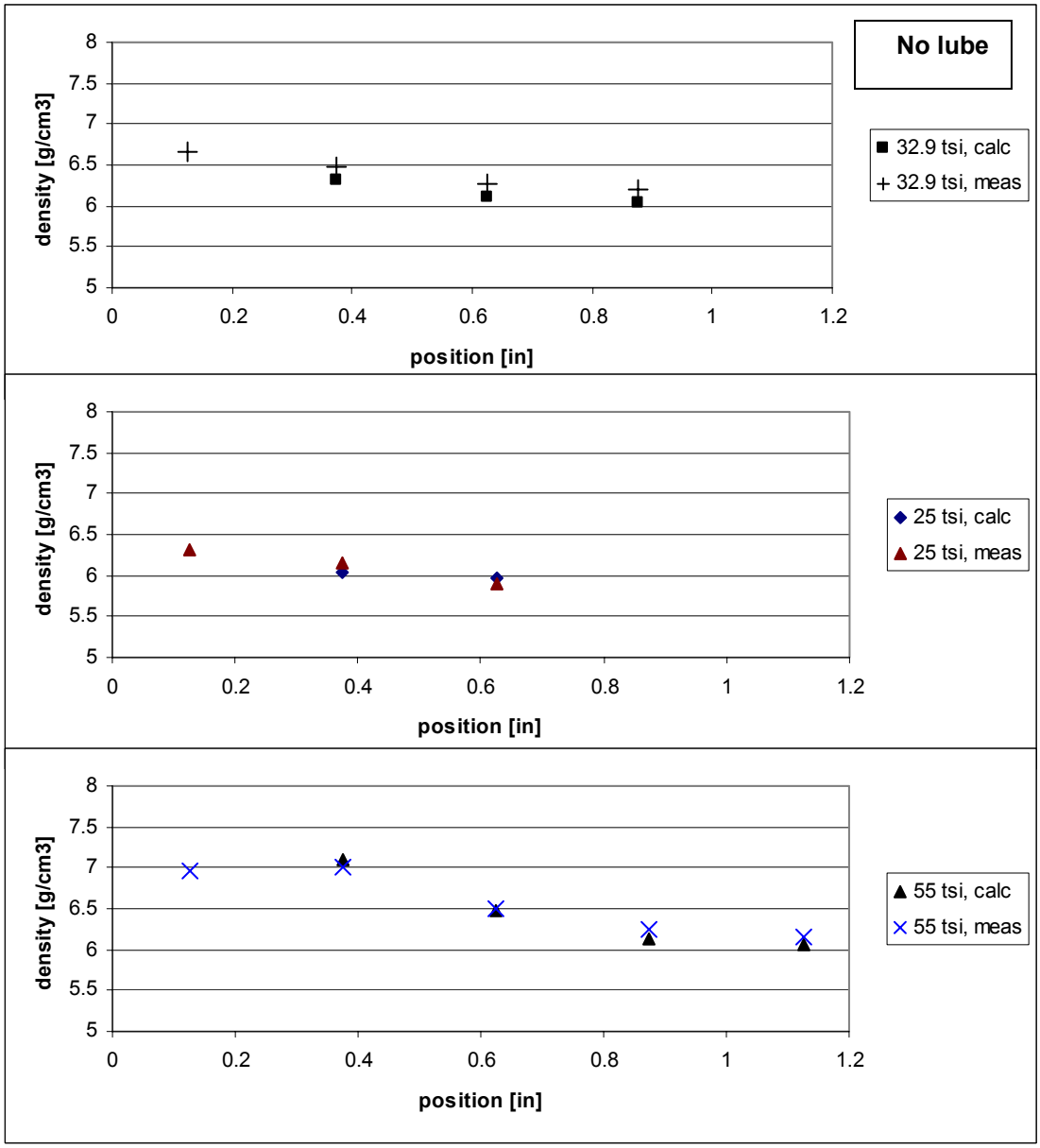

Figure 6.14: **Comparison of density values obtained from reconstruction and destructive testing, respectively, on green state P/M parts made from 1000B powder without lubricant. The close tracking of the data for values above 6.0g/cm^3 is clearly observable.**

6.2.4. Density Measurements with EIT Algorithm

In a next step, the density distribution throughout the cylindrical compact was reconstructed using the EIT algorithm. In order to do that, the cylindrical volume was subdivided into a

finite element mesh. The boundary conditions for the FEM simulation were chosen the same way as dictated by the measurement setup. A constant current of 1A was injected through the top surface by evenly distributing the current source over all nodes located on this cylinder face, resulting in a uniform current density throughout the volume. The bottom surface of the cylinder was made a ground plane, giving it the required relative observation point for the voltage and sinking the current at the same time. Then the voltage measurements taken from the experiments were applied as boundary constraints along the surface of the cylinder. Using the inverse EIT algorithm, the conductivity throughout the cylinder could be reconstructed. Figure 6.15 shows voltage distribution throughout the cylinder that results from the application of the reconstructed conductivity. The quality of the convergence can be observed in Figure 6.16. On the left we see a plot of both the actual voltage measurements and the voltage values at the same locations after executing the inverse algorithm. It is not a mistake that actually only one single step curve is visible. The measured and reconstructed voltages match closely to the point, so that they are basically identical and therefore appear as one line. On the right, the residual error between the two voltage sets is depicted. As we can see, the reconstructed conductivity produces a voltage pattern that very closely matches the measurements and therefore reflects the true conductivity distribution in the compact.

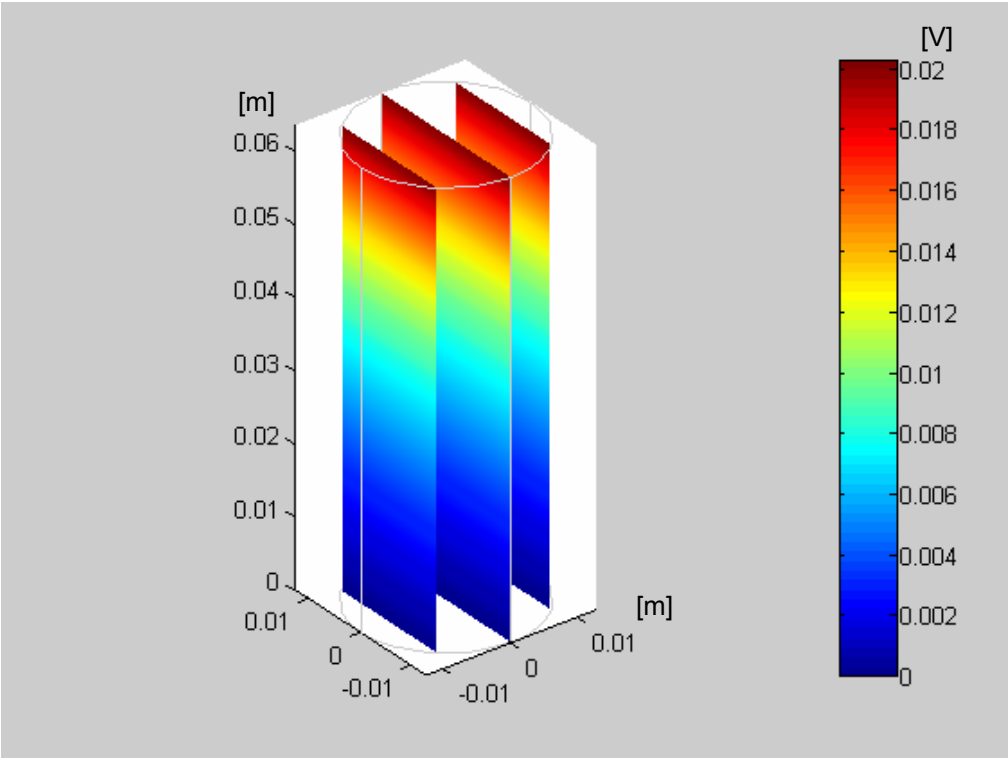

Figure 6.15: Voltage distribution resulting from the reconstructed conductivity distribution when injecting a constant current of 1A.

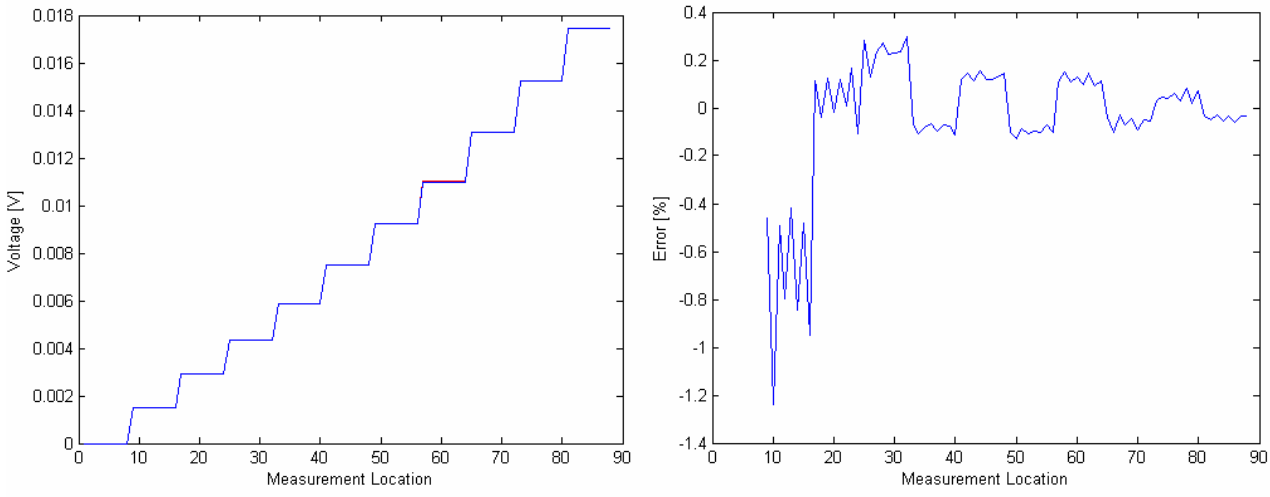

Figure 6.16: **Left: comparison of measured and reconstructed voltages. Right: Residual error in percent at measurement location after reconstruction. The measurement location corresponds to an arbitrary numbering of the probe location.**

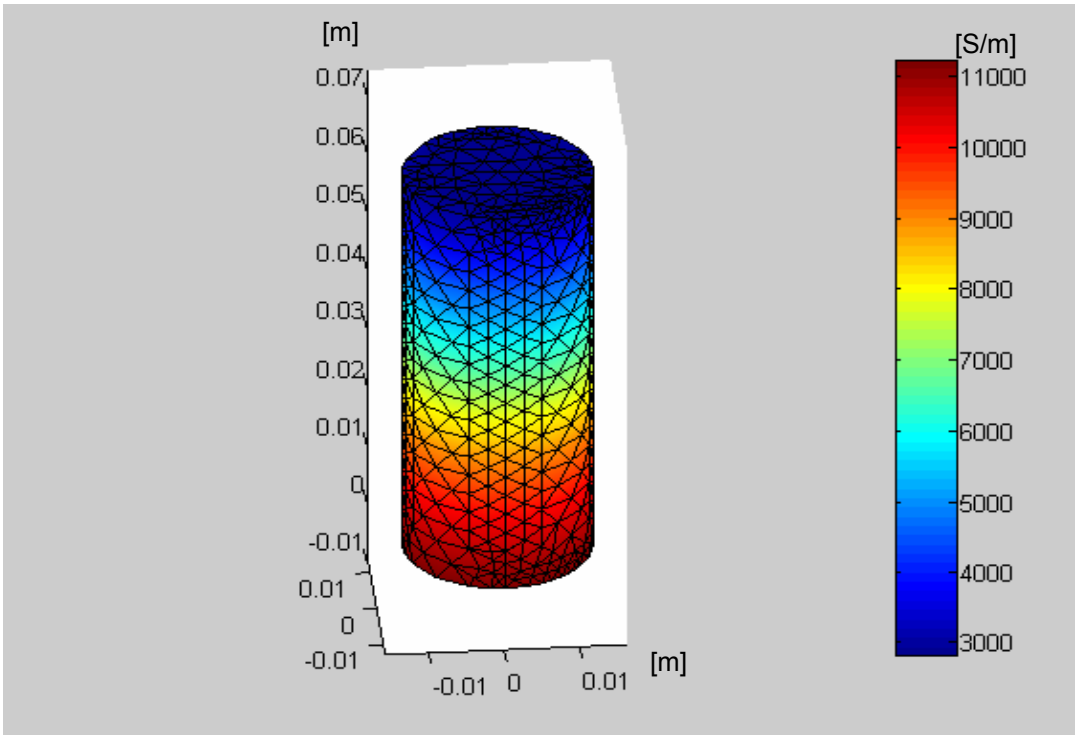

Figure 6.17: **Reconstructed conductivity distribution on the surface of the cylindrical sample.**

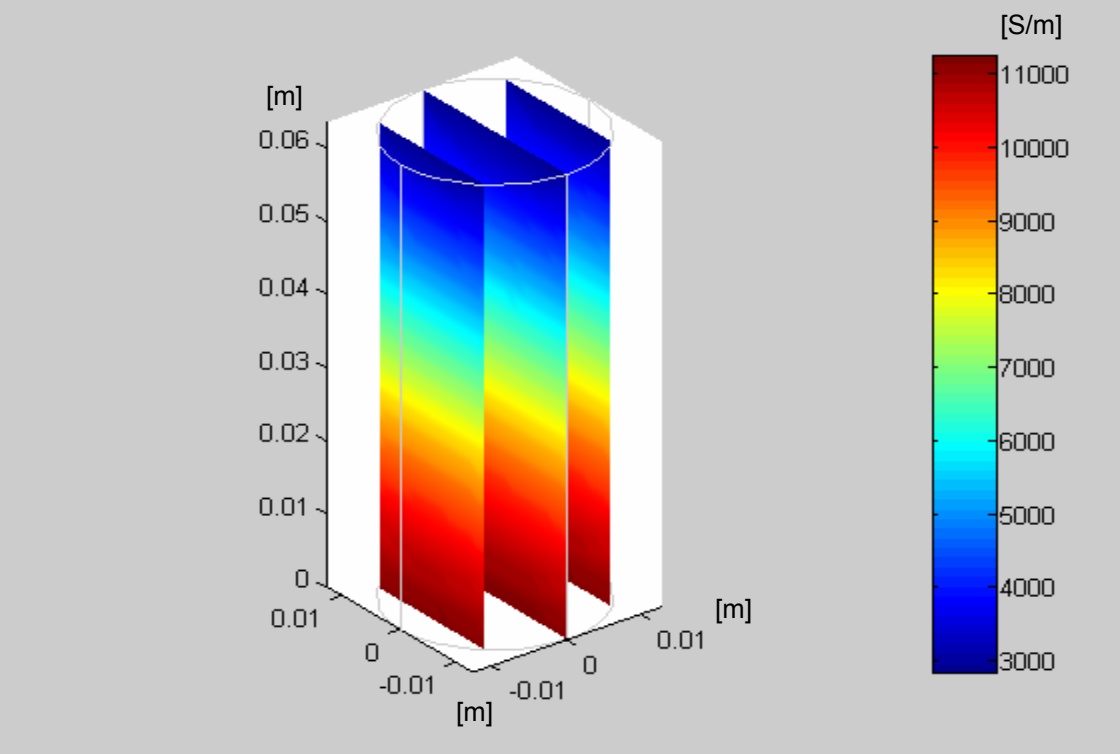

Figure 6.18: Reconstructed conductivity throughout the volume of the cylinder.

Figure 6.17 and Figure 6.18 display the reconstructed conductivity distribution on the surface and throughout the volume of the cylinder. As expected, the conductivity changes almost linearly from top of the part to bottom. Special consideration has to be given to the wide range of conductivities, which stems from the large density variation in the long, thin cylinder. The wide conductivity range makes the reconstruction more difficult, but as demonstrated in the results, even this does not pose a significant problem.

An even more detailed look at the conductivity distribution, as it was reconstructed by the inverse algorithm, is provided in Figure 6.19. Here we see a cross sectional slice through the center of the cylinder. As we can observe, the resulting conductivity distribution is not reconstructed as only changing along the length of the sample. The slight curvature is due to the limited amount of information available from the surface measurements.

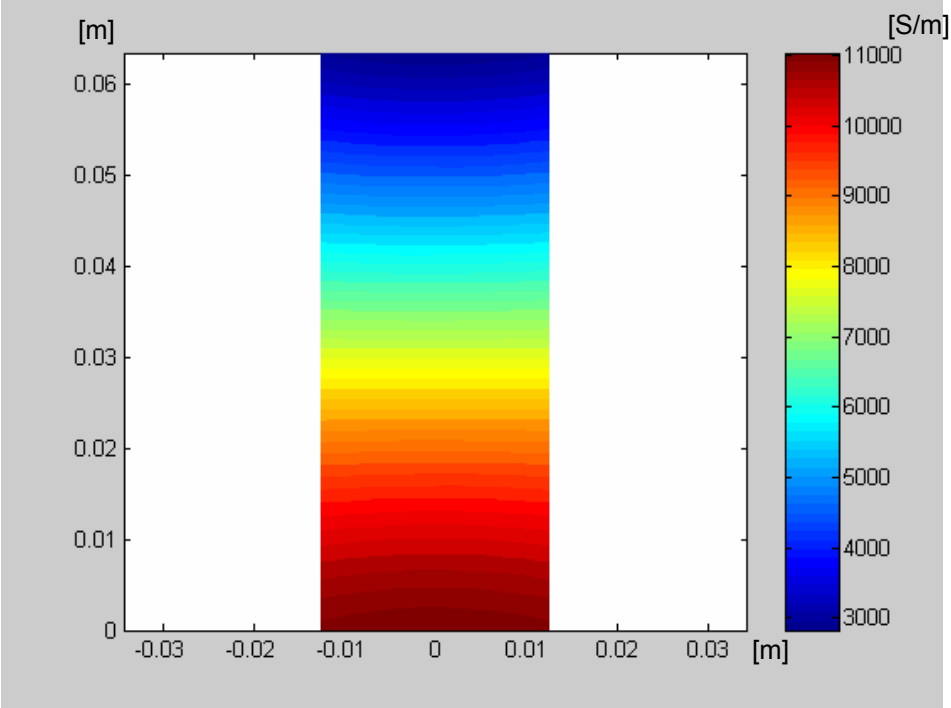

Figure 6.19: Cross-section of cylinder with details of reconstructed conductivity distribution.

The results obtained from the inversion algorithm can now be compared to the analytical results calculated from the destructive measurements or the simplified measurements that assumed piecewise constant densities. Figure 6.20 and Figure 6.21 compare the results for the direct (analytical) approach and the inverse algorithm based on two of the cylindrical samples that were analyzed. The conductivities shown are from the top of the part (starting at 0m) down to the bottom (0.06m). Shown are the results for two lubricated cylinders that were pressed at different tonnages. The lubricated samples were selected since the non-linear relationship between conductivity and density in these samples supposedly poses more difficulties for the reconstruction. A successful measurement of these parts would indicate a reconstruction that is even more straightforward for the non-lubricated P/M compacts.

The results are remarkably close, which is particularly surprising since we are dealing with an extraordinarily large range of conductivities (11000 S/m to 3000S/m) and the fact that one method assumes the conductivities to be piecewise constant, while the other method calculates a smooth distribution.

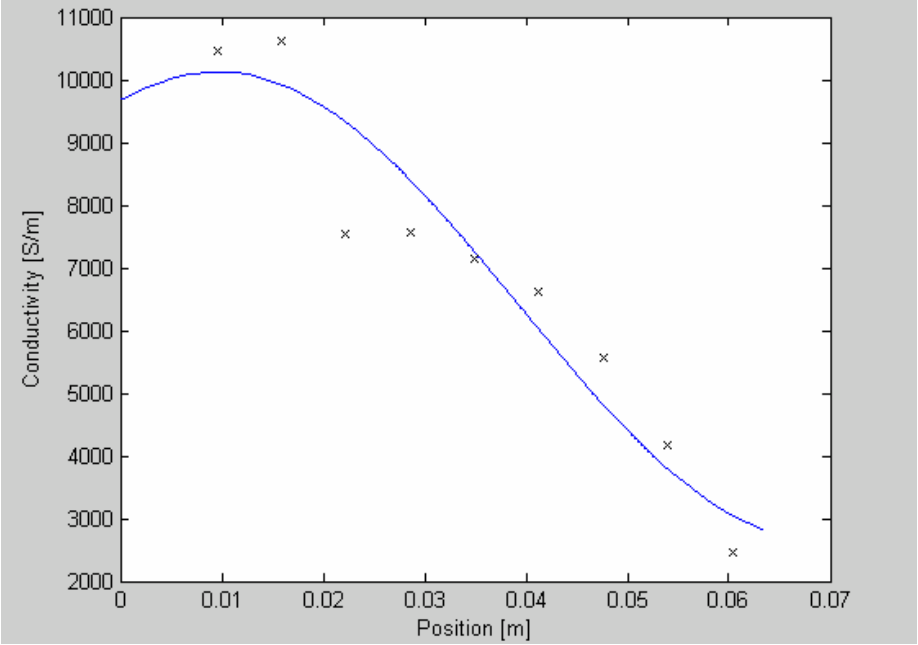

Figure 6.20: **Comparison of reconstructed (line) and measured (points) conductivity distribution in a cylindrical sample pressed from 1000B iron powder with 0.75% AWX lubricant at 25tsi.**

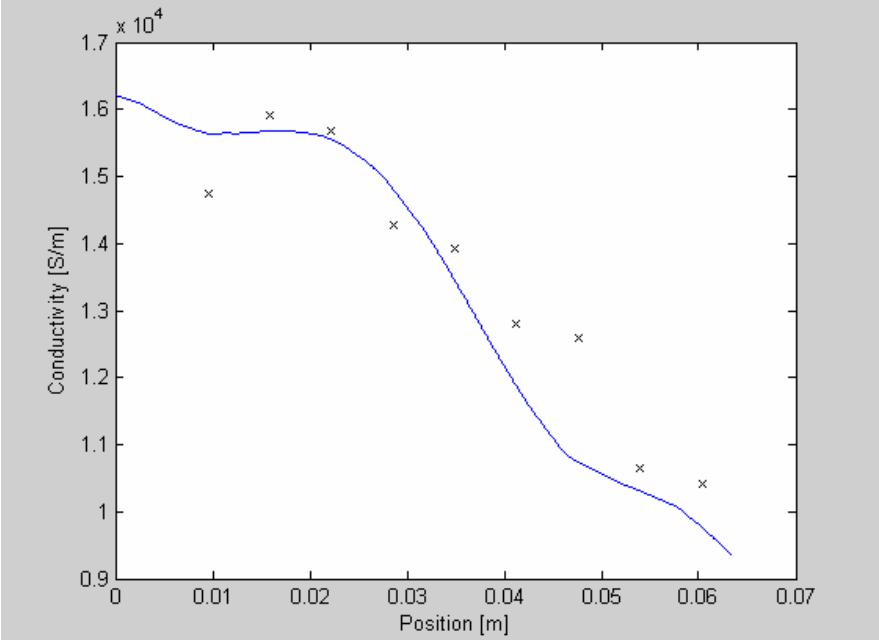

Figure 6.21: **Comparison of reconstructed (line) and measured (points) conductivity distribution in a cylindrical sample pressed from 1000B iron powder with 0.75% AWX lubricant at 44.7tsi.**

6.3. Measurements of Complex Parts

The applicability of the newly developed method to test green-state P/M parts for density variations of an arbitrarily shaped geometry was investigated with the measurement of a complex, hub-shaped gear. These parts, depicted in Figure 6.22, were provided by BorgWarner. And have the following specifications:

- Overall height 2.5” (0.8”, 1”, 0.7”), outer diameters 1.94”, 3”, 1.81”, inner diameter 1.25”
- Powder mixture FN0405 (Ancorsteel 1000B + 3.5% Ni + 0.6% graphite + 0.75% P-11 lubricant + ANCORBOND)
- Nominal density 6.9 ± 0.05 g/cm^3 in teeth, 6.85 ± 0.10 g/cm^3 in the two hubs

Figure 6.22: Complex, hub-shaped gear, provided by BorgWarner.

Two different types of density measurements were performed. First, the full density reconstruction was performed to generate a density map throughout the compact. Second, the same set of voltage measurements were used to test the possibility to discriminate between low and high density parts based on a simple comparison of the voltage measurements against a baseline recorded from a set of parts. The possibilities of this baseline method were also investigated by a number of finite element simulations. The measurement arrangement as well as the employed sensor for both methods was identical.

6.3.1. Sensor and Test Arrangement

A special sensor was fabricated to measure the density in the hub-shaped gear. The sensor was machined in two halves with contacting wires at a spacing of 0.1". The geometry of the sensor was such that it fits tightly around the compact. The two halves can be closed to provide an electrical contact all around the circumference of the gear in 0.1" spaced contacts. The wire was a non-insulated solid copper wire of size AWG 20. The ends of these contacting wires were led out of the sensor to close the loop at the outside and provide access for the measurements. The leads were left long enough to allow opening and closing of the two halves to insert a compact, even when the ends of the leads are soldered together for optimal electrical contact. The tight fit of the sensor around the gear and, hence, proper contact pressure, is guaranteed by four screws that hold the two halves together. The open sensor is depicted in Figure 6.23.

The sensor was used in a setup similar to the one used to measure the density – conductivity relationship for the disc-shaped compacts. Current was injected from top to bottom of the gear through cylindrical aluminum rods that contacted the two surfaces. A voltage controlled current source provided a constant current of 1A. The gear was placed in the sensor and voltage measurements were taken differentially between the leads protruding from the sensor. These voltages were measured manually using a bench top voltmeter with microvolt resolution. A picture of the measurement setup is given in Figure 6.24.

This test arrangement was adequate for our measurements to validate the concept of the proposed method. However, it still leaves ample room for future improvements. A computer controlled setup could be used to multiplex the measurement lines as well as the current source contacts. Such an automated setup would provide several distinct advantages:

- Decrease the measurement error by removing the necessity to manually change the connection of the voltage measurement probes.
- Take voltage measurements between several different contacts, further reducing measurement error and noise.
- Provide an opportunity to select several current injection patterns, which would increase the amount of information available for reconstruction.

The development of such an advanced measurement arrangement is left for future research.

Figure 6.23: Sensor developed for measuring density in complex hub-shaped gear.

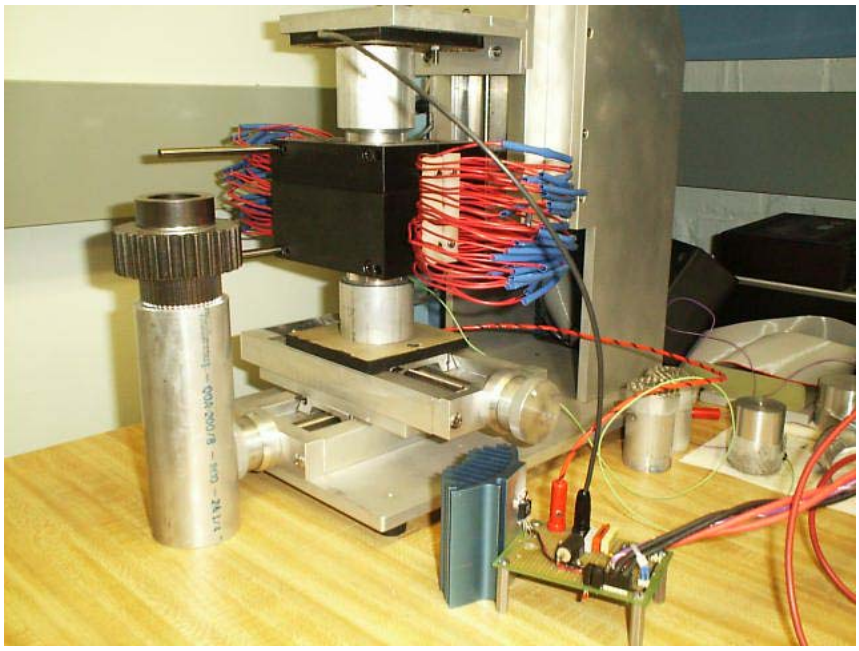

Figure 6.24: Measurement setup for EIT application to complex gear, showing the current source, bench press, sensor, and a part identical to the one that is currently in the sensor.

6.3.2. Inversion Results

The voltage measurements taken in concentric rings around the circumference of the gear were used as boundary constraints in the reconstruction algorithm. The reconstruction algorithm was implemented in Matlab®. The mesh, containing approximately 9000 nodes and 27000 elements was created by a mesh generating algorithm in the Femlab® software packet.

The reconstructed density distribution, depicted in Figure 6.25, shows the expected trend. While the density is clearly higher in the upper hub and somewhat higher in the lower hub, the center section is of lower density. The cross-sectional view, provided in Figure 6.26, confirms the expression gained from the surface information.

It is important to note that due to the limited amount of available information, the details provided in the two plots should not be taken “literally”. Instead it is the trend that is most indicative of the true behavior at the different nodes. Especially the local maxima and minima formed during reconstruction are probably an artifact due to missing information. An indication of this is the fact that these spots occur mainly in the center of the part where no measurements can be taken. An improved measurement setup with several different current injection patterns could help to overcome this problem. However, the presented pictures of approximated density variations throughout the gear already provide valuable information that was previously not available without destroying the part.

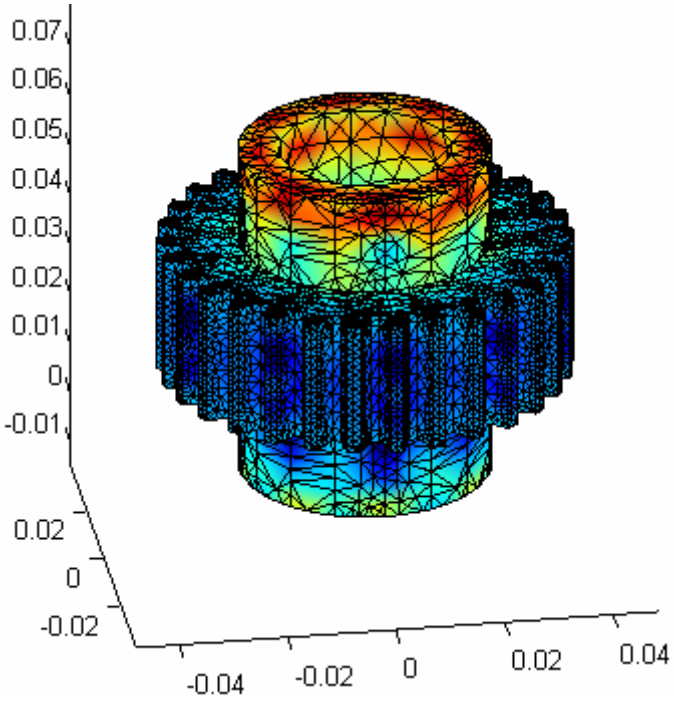

Figure 6.25 Reconstructed density distribution for hub-shaped gear. All dimensions are given in meters.

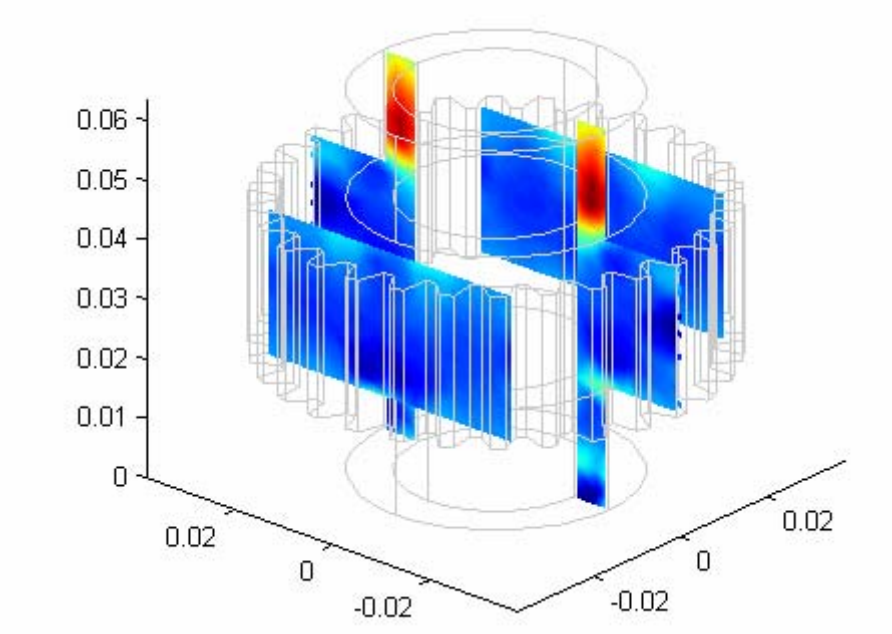

Figure 6.26: Cross-sectional view of reconstructed density distribution throughout the volume of the hub-shaped gear. Dimensions are given in meters.

6.3.3. Comparison against a Baseline

Another method of evaluating the voltage measurements is the comparison against a baseline. Here we are not interested in calculating absolute density variations or exactly locating the region of lower density. Rather we simply want to compare the results taken from a set of known good samples against the voltage measurements recorded from parts coming off the production line.

The background of this evaluation method relies on the fact that a given conductivity distribution produces a unique voltage pattern at the specified measurement points. Parts made form identical powder mixtures and with identical density distributions will produce identical voltage measurements when subjected to the same boundary conditions. Therefore, any change in the voltage pattern must be due to a change of any of these parameters. Since both the powder mixture and the boundary conditions are usually well controlled, the varying parameter is likely to be the density distribution. As a consequence, the method allows a simple comparison between the voltages measured at the test points and the voltages measured at the same test points on parts that were previously determined to be flawless. An identical voltage pattern indicates a part that is equally flawless. It is obvious that absolutely identical results can never be achieved. Therefore a baseline should be created from a number of known good parts, and subsequently, a

threshold must be defined. Voltage patterns from compacts that fall within this threshold will still be accepted, parts with measurement outside the threshold are rejected.

The possibilities of the suggested testing method were first evaluated in simulations. The solution for the forward problem was applied to the geometry of the hub-shaped gear. A number of measurement points were defined on the surface of the gear as shown in Figure 6.27. The vertical spacing of the points was 0.1", the same as the spacing of the ring contacts in our real sensor.

In a next step, two forward solutions were generated with different conductivity distributions. The boundary conditions for both cases were identical with a direct current of 1A injected evenly through the top surface of the gear, and the bottom surface being a ground plane. In the first solution, however, the conductivity was assumed to be constant throughout the part, while for the second solution a small region of lower conductivity was introduced. This conductivity distribution is depicted in Figure 6.28. The region of lower density was placed in the corner of the hub-shaped part where the highest concern for irregularities arises. The density was varied only over a very small region and by a small amount. The applied conductivity variation of 5% corresponds to a density change of approximately 0.1 g/cm^3, depending on the employed powder mixture.

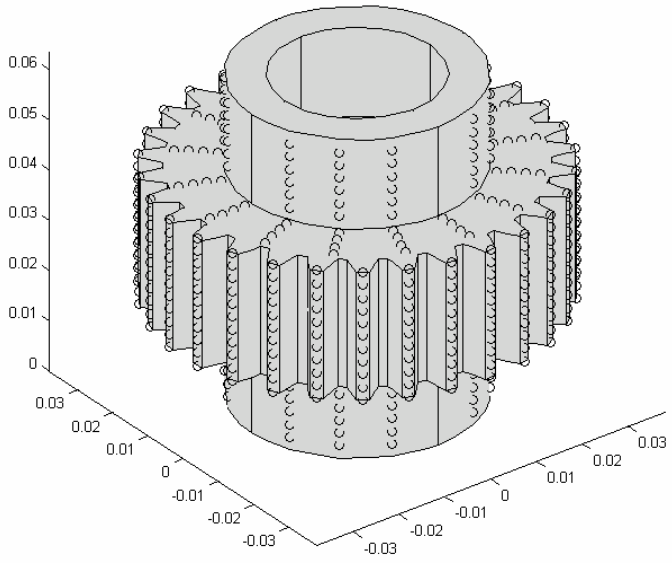

Figure 6.27: Three dimensional drawing of the gear indicating the measurement locations (rings) used in the simulation. All dimensions are given in meters.

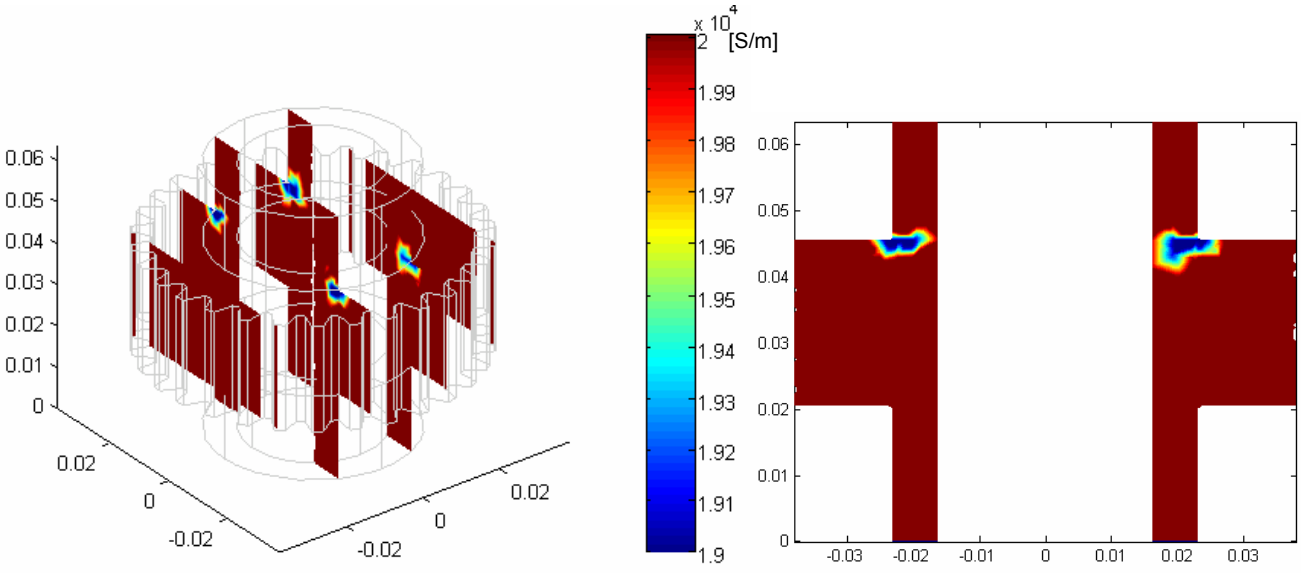

Figure 6.28: Simulated variation of density in the corner of the hub-shaped gear. Dimensions are given in meters.

The forward solutions for the two conductivity distributions, evaluated at the measurement nodes, were compared and the resulting voltage differences are plotted in Figure 6.29. The differences are clearly visible and can easily be used to discriminate between the two cases. The magnitude of the difference is small, but still measurable with high quality bench top instruments. Also the differences are on the order of magnitude of the absolute voltage measurements, indicating that they should be easily recordable.

It is obvious, however, that the results presented in Figure 6.29 are only so “clear-cut” because they stem from pure simulations. Measurements taken on real parts, will exhibit a measurement noise that makes the distinction more difficult. Measurement noise is not so much expected to arise from the measurement instrument, but more from the setup and from the measured part. Since we are injecting and measuring DC currents and voltages, instrument noise can usually be reduced to the microvolt level, such that it will not affect the accuracy. More reason of concern is presented by the placement of the measurement probes and small density variations throughout the green-state compact that both will result in small changes in the forward solution. Since these changes and their effects are not known at the time of measurement, they are perceived as measurement noise.

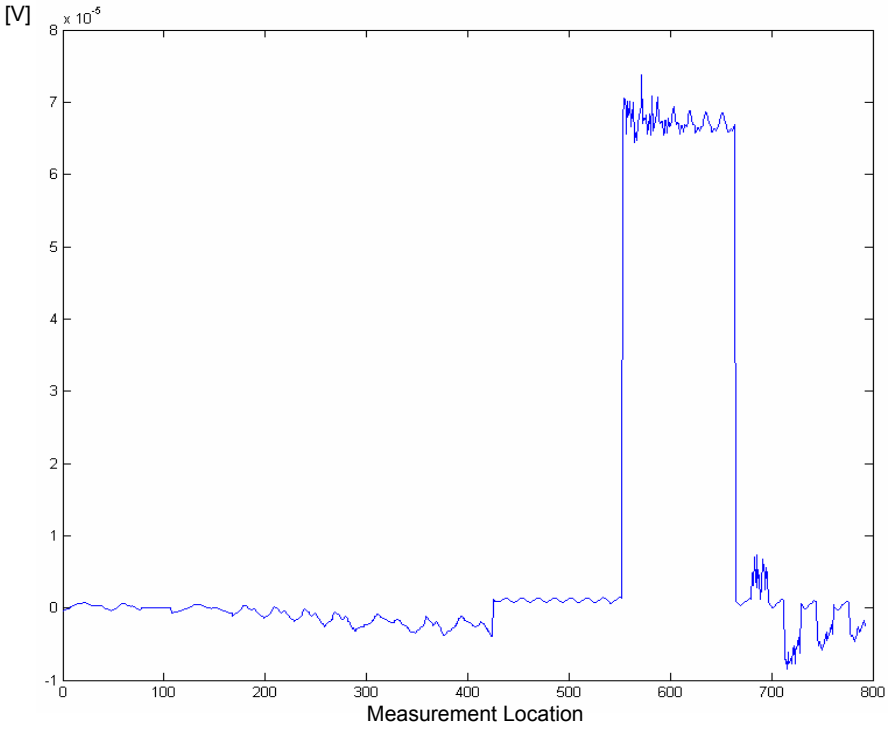

Figure 6.29: Voltage differences at measurement points that occur between uniform density and simulated low density regions. The measurement locations correspond to an arbitrary numbering of the selected measurement points.

The effects of measurement noise to the discrimination possibilities were investigated by adding white noise to the measurement data for both sets. The noise was added artificially to the simulation results through the use of a random generator that produces random numbers evenly distributed over the interval (0, 1). The amplitude of the noise was scaled to reach maximally 20% of the measurement voltage. The comparison of these noisy signals, shown in Figure 6.30, clearly shows a reduced visibility of the differences. Although the differences are still visible to the eye, an automatic detection algorithm will find it difficult to positively discriminate between the two signals.

Although this result seems to predict severe limitations to the usability of the method, the opposite is the case. We have to keep in mind that the above comparison was made only between two compacts. The situation can be drastically improved when comparing the measurements of the “faulty” part against a baseline consisting of the measurements of many good parts. Acquiring a baseline of the voltages measured on a number of good parts is the same as building an average over a set of noisy data. If the data set taken from the “faulty” part is compared against a baseline of 50 good parts, we can again clearly detect the variation. This is illustrated in Figure 6.31.

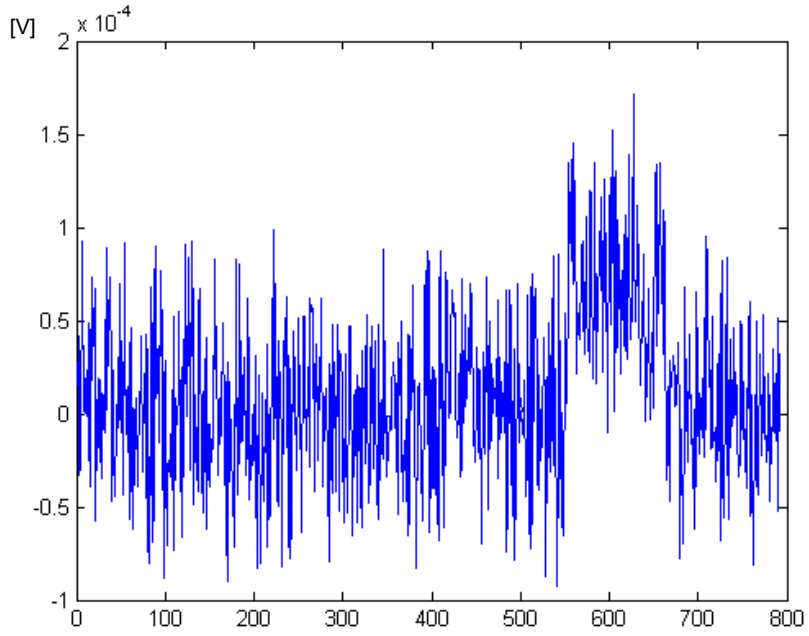

Figure 6.30: **Resulting voltage differences for the same 800 measurement points when adding 20% noise to the measurement data.**

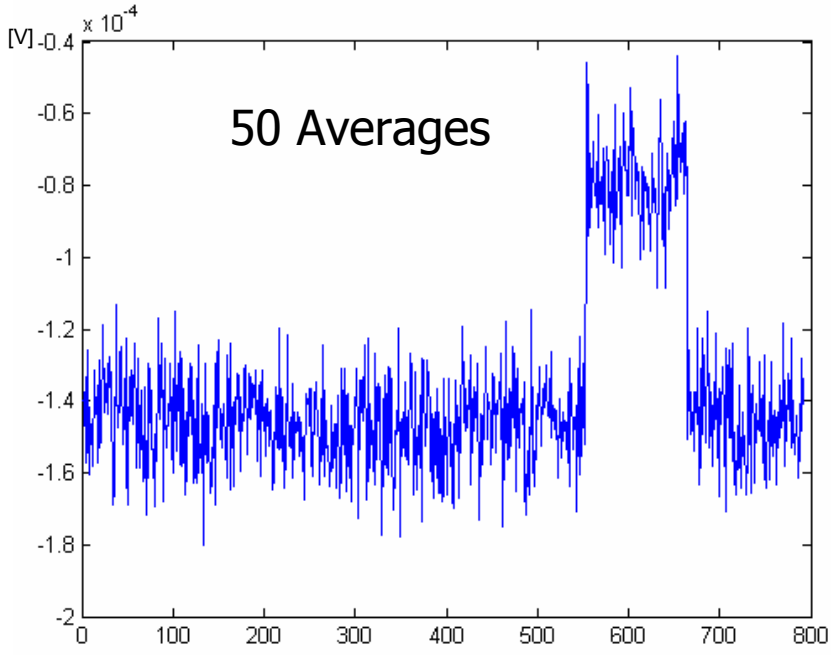

Figure 6.31: **Resulting voltage differences for noisy data (20% noise) using 50 averages.**

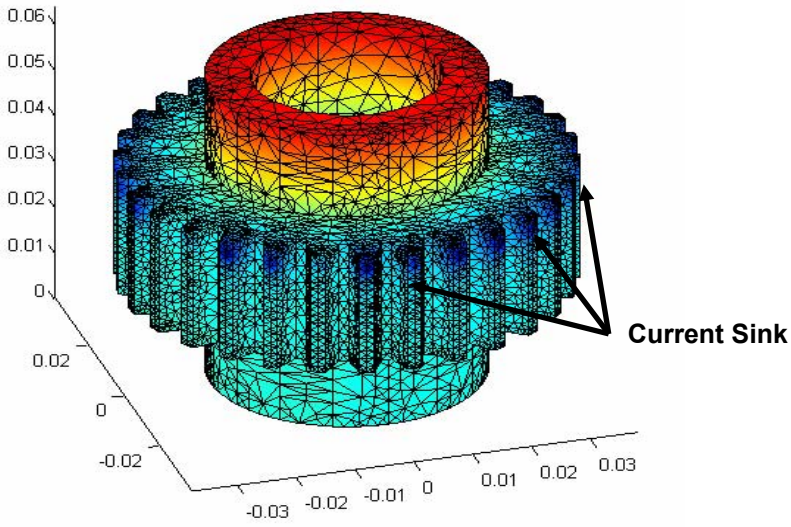

Figure 6.32: Improved current injection scheme for detection of density variation in corner of hub-shaped gear. Current is injected through the top surface and a ring around the teeth of the gear. All dimensions are given in meters.

The ability to detect a density variation can be further improved upon by applying boundary conditions specific to the current investigation. If the uniformity of the density in a certain region within the part raises cause for concern, this area can be targeted specifically by applying the boundary conditions in a way that would cause a maximal voltage difference on the surface. Since the surface voltages depend directly on the amount of current flowing through the part, the goal must be to direct as much current as possible through the region of concern. A change in the conductivity in this region will then lead to a larger change in the measured voltages. Such a setup is shown in Figure 6.32, where the current is still injected through the top surface of the gear, the ground nodes and therefore the current sink, however, are now located around the teeth of the gear. This forces the current to flow out toward the teeth through the area of interest. We should note that such a current injection scheme automatically reduces the amount of information that can be obtained from sections that are below the current sink. Careful selection of one or several sets of boundary conditions will enhance the ability to detect density variations while reducing the amount of unwanted information.

The simulation results encourage the use of this method to compare the recorded voltages of production samples against a baseline created from the measurement of a set of known good parts. Small deviations in the density distribution can be singled out and potentially faulty parts can be detected at an early stage. The simulation results seem to be confirmed by the data

provided in Figure 6.33. Here we see the absolute voltage measurements as they were recorded on the gear using the above mentioned sensor. The graph shows the measurements, taken on a number of compacts, from the top to the bottom of the part. Even with the limited amount of samples that were available for testing, a separation into two groups with different conductivities seems apparent. Although the method cannot provide any detailed information about the localization or size of the region exhibiting a different conductivity, it still allows recognizing the different behavior under test. As such, this method allows a fast and simple way to separate potentially faulty parts from the production, without the need of a full EIT inversion.

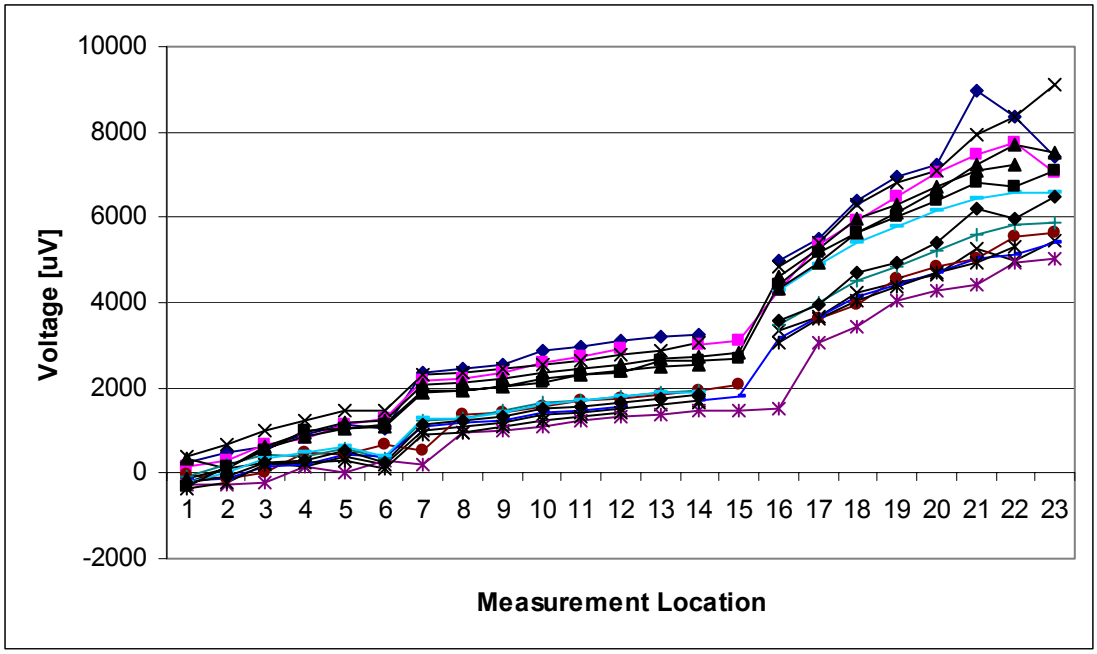

Figure 6.33: Voltage measurements on a number of gears. One data set shows the recordings on one gear from top to bottom. A clear separation between lower density and higher density parts can be observed.

7 Conclusions

The goal of this project was to show the feasibility of the detection of density variations in green-state compacts from surface voltage measurements. The basic premise was to inject currents into the compacts and measure the resulting electric potentials at several measurement points on the surface of the part. By assuming a direct relationship between the conductivity of a green-state P/M sample and its density, density variations between otherwise identical samples could be detected. Additionally, executing an inverse algorithm would allow the generation of a density map based on this information.

In a first step, the relationship between conductivity and density of green-state P/M compacts was investigated. Tests were made on a number of parts from various different powder mixtures. In all cases a clear correlation between conductivity and density could be established, indicating that measurements of electric conductivity can indeed be exploited to render valid information about the density of a green-state P/M compact. However, while the correlation between green density and electric conductivity is linear for non-lubricated parts, the results show a different behavior for lubricated samples. For lubricated samples it was found that the conductivity increases with increasing density, but only up to a maximum conductivity reached at approximately 6.9g/cm^3. Further increase of the density reduced the conductivity again. This behavior was confirmed to be inherent to all powder mixtures with lubricants added.

Since this relationship between conductivity and density lies at the core of our proposed method of detecting density variations, further investigation into the matter is warranted to explain the physical effects that produce the above mentioned behavior. As a result of these investigations, a new electrostatic model was presented that is capable of predicting the conductivity in green-state metallurgy parts for both lubricated and non-lubricated samples. Simulations show that the developed model faithfully describes the electrostatic situation in a green-state P/M compact. Besides explaining the physical effects leading to the phenomenon of the observed inversion behavior, the model provides the basis for future research, investigating the effect of each model parameter in more detail.

It is important to note that this model is not intended to calculate the absolute value of the conductivity of a green-state P/M compact for a given density. Due to parameter variations entering the model equations and due to the unknown influence of each of these parameters, this

model cannot provide absolute values. Additional research is required to make further progress in this direction. However, the model provides a physically correct approach when calculating the conductivity–density relationship and as such is capable of adequately explaining the counter-intuitive inversion effect.

The changes of the conductivity with density variations were found to be strong enough to provide a good basis for the discrimination between regions of varying densities. In a subsequent step, an algorithm was developed that allows predicting the conductivity distribution from a set of surface voltage measurements. This included a thorough understanding of the electrostatic situation for a solid with known boundary conditions. The research in this area led to a closed form calculation of the electric potential in a two-dimensional circular disc with two different conductivities. The investigations were then expanded to three dimensions with the development of a closed form solution for the current flow and electric potential inside a conducting cylinder. The insight into the current flow patterns gained from these investigations proved to be invaluable for the development of an appropriate measurement setup for the P/M parts.

A finite element solver together with an inversion algorithm was then implemented that can be employed for samples of arbitrary geometry. The algorithm can reconstruct the conductivity distribution and thus the density distribution from surface voltage measurements. This finite element method is a significant extension of the previous analytical solution, which works only for the simplest geometries.

A test arrangement was constructed that includes a voltage-controlled current source, a bench top voltmeter and two new special purpose test sensors. One sensor was used for the cylindrical sample, the other one was constructed for the testing of hub shaped gears. The sensors contact the P/M sample around the circumference with a resolution of 0.1”. These contacts provide the means to acquire the data for detecting density variations along the longitudinal axis of the parts.

Using this measurement arrangement and the newly developed sensors, the validity of the inverse algorithm was tested for both the cylindrical parts and the hub shaped gear. For the cylindrical compacts, the validity of the simulations was verified by comparing the results obtained from the finite element solver to the results from destructive measurements with conventional methods. These comparisons showed a remarkable agreement between the reconstructed densities and the results from the conventional measurement, even though the approximate calculations used in the destructive measurements assumed a piecewise constant conductivity, whereas the finite element solver calculated a smooth conductivity distribution.

The feasibility of the instrumentation approach for both simple and complex parts could also be demonstrated. The new method of measuring density variations in a non-destructive manner by recording surface voltages generated by a DC current source has the potential to

serve as an important add-on for inspection tools available for quality assurance. Since no known method can provide similar information without destroying the analyzed sample, the presented method is a major step forward in the ability to gain quantitative information about the inside of a green-state compact without the need for expensive equipment, time consuming procedures, or destructive tests. The simplest application of the proposed method is the comparison of the recorded voltages against a baseline. Although simple in its application it is nonetheless sensitive enough to detect even small density variations throughout the sample.

8 Recommendations for Future Work

The presented work has introduced new ways to obtain basic physical properties of green-state P/M compacts. The work also documents a new way to monitor density variations. As a result, it has opened a venue of investigation that provides many opportunities for additional research.

One area of possible future research is the in-depth investigation of the relationship between electric conductivity and green density of P/M compacts. The presented work has introduced a physical explanation that provides an insight into the changes occurring in the powder mixtures that were investigated. Additional research should now be carried out to focus on

- the experimental confirmation of potential anisotropic material effects that are expected from the depolarization of the lubricant particles,
- the effects of lubricant migration and its impact on correctly predicting the electric conductivity distribution
- the need to calculate the conductivity-density relationship for any given powder mixture and density, thereby eliminating the requirement for potentially tedious measurements to establish this relation.

Another interesting area for future research is the development of optimized sensors for the density predictions. For instance, modular designs may be required to adapt the sensor to a range of part geometries. Furthermore, a sensor configuration may be established that provides an optimal amount of data for the EIT algorithm. This optimal sensor configuration will again depend on the geometry of the particular part under inspection. Further issues are the current injection locations, the setup of “localized” measurements on small features of a part, and probe spacing.

An important additional research area is the possible integration of the voltage sensor concept into the press. Such an on-line approach would have several advantages:

1. No additional test step is required to perform the density measurement. The parts remain in the die at the end of compaction process and are measured automatically without the need for costly manual intervention or complex automation.
2. The location of the sensor probes in the die is likely to produce very repeatable measurements with no variations regarding probe location or contact pressure.
3. Built-in sensors in the press allow online monitoring of the compaction process by measuring the voltage during press motion. This could provide valuable additional information about the compaction process itself as well as about the dynamic behavior of the part.

Additional research should concentrate on identifying new areas of application for this nondestructive evaluation technique. Although the most advantageous application appears to be related to the P/M industry, the method itself can also be implemented in other industries where the monitoring of possible density variations is of interest. The test methodology can be applied to wide range of different materials. The prerequisite is that the material does exhibit a functional relationship between density and electric conductivity, and that the electric conductivity is in a range that yields measurable signal responses.

9 References

1. __, “Powder Metallurgy Design Manual”, Metal Powder Industries Federation, Princeton, NJ, 1989
2. Adler, A., Guardo, R., “Electrical impedance tomography: regularized imaging and contrast detection”, *IEEE Transactions on Medical Imaging,* Volume 15, Issue 2, 1996, pp. 170-179
3. Aharoni, S.M., “Electrical Resistivity of a Composite of Conducting Particles in an Insulating Mixture”, *Journal of Applied Physics*, vol. 43, No.5, May 1972, pp. 2463-2465
4. Arridge, S.R., Schweiger, M., “Inverse Methods for Optical tomography”, *Information Processing in Medical Imaging. 13th International Conference, IPMI '93 Proceedings*, 1993, pp. 259-277
5. Aubert, G, Kornprobst, P, “Mathematical Problems in Image Processing”, *Applied Mathematical Sciences*, vol. 147, Springer, New York, 2002
6. Barber, D.C., Brown, B.H., “Applied potential tomography”, *Journal of Physics E: Sci. Instrumentation*, vol. 17, 1984, pp. 723-733
7. Binley, A., Pinheiro, P., Dickin, F., “Finite element based three-dimensional forward and inverse solvers for electrical impedance tomography”, *IEE Colloquium on Advances in Electrical Tomography,* (Digest No.1996/143), 1996, Page 6/1-3
8. Bogdanov, G. ; Ludwig, R.; Michalson, W.R., “A new apparatus for non-destructive evaluation of green-state powder metal compacts using the electrical-resistivity method”, *Measurement Science & Technology,* Volume 11, Issue 2, 2000, pp. 157-166
9. Bogdanov, G., “Theoretical Basis and Practical Implementation of Electrical Impedance Material Inspection of Powder Metallurgy Compacts”, Master Thesis, Electrical and Computer Engineering Department, Worcester Polytechnic Institute, 2000
10. Breckon, W. R.; Pidcock, M. K., “Mathematical Aspects Of Impedance Imaging”, *Clinical Physics and Physiological Measurement*, vol. 8 suppl. A, 1986, pp. 77-84

11. Bruggemann, D.A.G., „Berechnung verschiedener physikalischer Konstanten von hetoregenen Substanzen I“, in *Annalen der Physik,* vol. 24, 1935 pp. 636 – 679

12. Bruggemann, D.A.G., „Berechnung verschiedener physikalischer Konstanten von hetoregenen Substanzen II“, in *Annalen der Physik,* vol. 25, 1936 pp. 645 – 672

13. Brühl, M., Hanke, M., “Numerical Implementation of two noniterative methods for locating inclusions by impedance tomography”, *Inverse Problems*, vol. 16, 2000, pp 1029-1042

14. Celzard, A., Mareche, J.F. and Payot, F., “Simple method for characterizing synthetic graphite powders”, *J. of Physics D: Applied Physics*, vol. 33, 2000, pp.1556-1563

15. Chen, Z.Q., Paoloni, F.J., “An error study on some linear reconstruction algorithms for electrical impedance tomography”, *Clinical Physics and Physiological Measurement*, vol. 13, Issue 4, 1992, pp. 389-409

16. Cheney, M., Isaacson, D., “Issues in electrical impedance imaging”, *IEEE Computational Science and Engineering,* vol. 2, Issue 4,, pp. 53-62

17. Chew, C.W., “Waves and Fields in Inhomogeneous Media”, Van Nostrand Reinhold, New York, NY, 1990

18. Clark, F., “Advanced Techniques in Powder Metallurgy”, Rowman and Littlefield, Inc, New York, NY, 1963

19. Deprez, I and McLachlan, D.S., “The analysis of the electrical conductivity of graphite powders during compaction”, in *Journal of Physics D: Applied Physics*, vol. 21, issue 1, 1998, pp.101-107

20. Edic, P.M.; Isaacson, D.; Jain, H.; Newell, J.C.; Saulnier, G.J.; “An iterative Newton-Raphson method to solve the inverse admittivity problem”, *IEEE Transactions on Biomedical Engineering,* Volume 45 Issue 7 , Jul 1998, pp. 899 -908

21. Euler, K.-J., „Elektrische Leitfähigkeit von komprimierten Metallpulvern”, in Planseeberichte für Pulvermetallurgie, vol 27, 1979, pp. 15 – 31

22. Euler, K.J., Fromm, R., Sperlich, B., “Electric Conductivity of Compressed Nickel Powder”, *Planseeberichte für Pulvermetallurgie*, vol. 28, 1980, pp. 127-134

23. Gelfand, I.M., Gindikin, S.G., “Mathematical Problems of Tomography“, American Mathematical Society, Providence, RI, 1990

24. German, R.M., “Powder Metallurgy Science”, Metal Powder Industries Federation, Princeton, New Jersey, 1984

25. Geselowitz, D.B., “Application of the compensation theorem in the development of the scattering parameters”, *IEEE Transactions on Education*, vol. E-14, n 2, May 1971, pp. 71-72

26. Gladwell, G.M.L., “Inverse Problems in Scattering”, Kluwer Academic Publishing, Dordrecht, Netherlands, 1993

27. Gosh Roy, Dilip N., “Methods of Inverse Problems in Physics”, CRC Press, Boca Raton, 1991

28. Haus, H.A., Melcher, J.R., “Electromagnetic Fields and Energy”, Prentice Hall, NJ, 1989, pp. 147.

29. Hausner, H.H., “Handbook of Powder Metallurgy”, Chemical Publishing Co., New York, NY, 1982

30. Hirschhorn, J, “Introduction to Powder Metallurgy”, American Powder Metallurgy Institute, Princeton, NJ, 1976

31. Hofmann, B., “Approximation of the inverse electrical impedance tomography problem by an inverse transmission problem”, *Inverse Problems*, vol. 14, 1998, pp. 1171-1187

32. Isakov, V., “Inverse problems for partial differential equations”, *Applied Mathematical Sciences*, vol. 127, Springer, New York, 1998

33. Jie-Ren Shie, Li, C.J., Jen-Tai Lin, “Differential imaging in electrical impedance computerized tomography, *Materials Evaluation,* Volume 59, Issue 3, 2001, pp. 406-412

34. Jones, W.D., “Fundamental Principles of Powder Metallurgy”, Edward Arnold Publishers Ltd, London, 1960

35. Kallman, J.S., Berryman, J.G., “Weighted Least-Squares Criteria for Electrical Impedance Tomography”, *IEEE Transactions on Medical Imaging*, vol. 11, No. 2, June 1992, pp. 284-292

36. Klar, E. (Ed.). “Powder Metallurgy: Applications, Advantages and Limitations”, American Society for Metals, Metals Park, Ohio, 1983

37. Kress, R. “Linear Integral Equations”, *Applied Mathematical Sciences*, vol. 82, Springer, New York, 1999

38. Lam, J., “Effective longitudinal dielectric constant of a rectangular lattice of parallel prolate spheroids”, *Journal of Applied Physics*, vol. 68, July 1990, pp. 392-403

39. Landauer, Rolf, „Electrical Conductivity in Homogenous Media”, in *Am. Inst. of Physics Conf. Proceedings*, vol. 40, 1978, pp. 2 – 43

40. Langenberg, K.J., Schmitz, V., “Generalized tomography as a unified approach to linear inverse scattering: theory and experiment”, *Acoustical Imaging. Proceedings of the 14th International Symposium*, 1985, pp. 283-294

41. Leuenberger, G., Ludwig, R., Apelian, D., “Electrostatic detection of density variations in green-state powder metallurgy compacts”, *Proceedings of QNDE 2001*

42. Ludwig, R., Leuenberger, G., Makarov, S., Apelian, D., “Electric Voltage Predictions and Correlation with Density Measurements in Green-State Powder Metallurgy Compacts”, *Journal of Nondestructive Evaluation*, vol. 21, No. 1, pp. 1-9

43. Ludwig, R., McNeill, J.A., and Stander, J.A., US Patent No. 6,218,846 (17 April 2001)

44. Ludwig, R., Zenger, D., Zhang, R., “Review of Various Non-Destructive Testing Methods for Detecting Cracks in Green P/M Components”, Carl Gunnard Johnson Powder Metallurgy Research Center, Departments of Electrical and Manufacturing Engineering, Worcester Polytechnic Institute, Worcester, Massachusetts, April 1995.

45. Luk, S.H., Narasimhan, K.S., Winterton, P.J., Pfingstler, T., Russel, S., “Higher green strength enhancements to increase process robustness”, *Hoeganaes Technical Library*, Paper No. 100

46. Makarov, S. ; Ludwig, R.; Apelian, D., “Identification of depth and size of subsurface defects by a multiple-voltage probe sensor: analytical and neural network techniques”, *Journal of Nondestructive Evaluation,* Volume 19, Issue 2, 2000, pp. 67-80

47. Makarov, S., Ludwig, R., and Apelian, D., “Numerical Solution Of A Direct 3D Electrostatic Resistivity Test Of Green-State Metal Powder Compacts,” in *Review of Progress in Quantitative NDE*, vol. 17B, Plenum Press, 1998, pp. 1462 - 1470.

48. Malliaris, A. And Turner, D.T., „Influence of Particle Size on the Electrical resistivity of Compacted Mixtures of Polymeric and Metallic Powders”, in *Journal of Appl. Physics*, vol. 42, 1971, pp. 614 – 618

49. Marquardt, D. W., “An Algorithm for Least-Squares Estimation of Nonlinear Parameters”, *Journal of the Society for Industrial and Applied Mathematics*, vol. 11, Issue 2, June 1963, pp. 431-441

50. Maxwell, J.C., “A treatise on electricity and magnetism”, Dover Publications, New York, NY, 1954, Art. 437 and 438

51. McLachlan, D.S., “Equations for the conductivity of macroscopic mixtures”, *Journal of Physics C: Solid State Physics*, vol. 19, 1986, pp. 1339-1354

52. McLachlan, D.S., „An equation for the conductivity of binary mixtures with anisotropic grain structures“, in *Journal of Physics C: Solid State Physics*, vol. 20, 1987, pp. 865 - 877

53. McLachlan, D.S., „Equation for the conductivity of metal – insulator mixtures“, in *Journal of Physics C: Solid State Physics*, vol. 18, 1985, pp. 1891 – 1897

54. McLachlan, D.S., Blaszkiewicz, M., Newnham, R.E., “Electrical Resistivity of Composites“, *Journal of American Ceramic Society*, vol. 73, 1990, pp. 2187-2203

55. Menke, William, “Geophysical Data Analysis: Discrete Inverse Theory”, Academic Press, San Diego, 1989

56. Morucci, J.-P., Marsili, P.-M., “Bioelectrical Impedance Techniques in Medicine, Part III: Impedance Imaging; Reconstruction Algorithms”, Critical *Reviews in Biomedical Engineering*, vol.24, 1996, pp. 599-654

57. Morse, P., Feshbach, H., “Methods of Theoretical Physics“, Volume I, McGraw-Hill, NY, 1953, pp. 869

58. Morse, P., Feshbach, H., “Methods of Theoretical Physics“, Volume II, McGraw-Hill, NY, 1953, pp. 1252

59. Natterer, F., “The Mathematics of Computerized Tomography”, Wiley, New York, NY, 1986

60. Ortega, J.M., Rheinboldt, W.C., “Iterative Solution of Nonlinear Equations in Several Variables”, Academic Press, Inc., New York, New York, 1970

61. Osborn, J.A., “Demagnetizing Factors of the General Ellipsoid”, *Physical Review*, vol. 67, No. 11/12, June 1945, pp. 351-357

62. Pease, L.F. III, “Inspection and Quality Control for P/M Materials”, Materials Handbook, vol.17, 1984

63. Polstyanko, S.V., “Fast Adaptive Schwarz-type Finite Element Approach for Solving Electrostatic Problems”, Ph.D. Thesis, Department of Electrical and Computer Engineering, Worcester Polytechnic Institute, 2000

64. Rheinboldt, W.C., “Methods for Solving Systems of Nonlinear Equations”, Society for Industrial and Applied Mathematics, Philadelphia, 1998

65. Rigaud, B., Morucci, J.-P., “Bioelectrical Impedance Techniques in Medicine, Part III: Impedance Imaging; General Concepts and Hardware”, Critical *Reviews in Biomedical Engineering*, vol.24, 1996, pp. 467-597

66. Roberts, J.N. and Schwartz, L.M., “Grain consolidation and electrical conductivity in porous media”, *Physical Review B*, vol. 31, issue 9, 1985, pp. 5990-5997

67. Romanov, V. G., “Inverse Problems of Mathematical Physics”, VNU Science Press, Utrecht, Netherlands, 1987

68. Sands, R.L., Shakespeare, C.R., “Powder Metallurgy: Practice and Applications”, CRC Press, Cleveland, OH, 1966

69. Scarisbrick, R.M., “Electrically conducting mixtures”, *Journal of Physics D: Applied Physics*, vol. 6, 1973, pp. 2098-2110

70. Stakgold, I., “Green’s Functions and Boundary Value Problems”, Second Edition, John Wiley & Sons, New York, NY, 1998

71. Stander, J. G., Plunkett, J., Zenger, D., McNeill, J., and Ludwig, R., “Electric resistivity testing of green-state powdered metallurgy compacts,” in *Review of Progress in Quantitative NDE*, vol. 16B, Plenum Press, 1997, pp. 2005 - 2012.

72. Stasa, Frank, “Applied Finite Element Analysis for Engineers”, CBS Publishing, New York, 1985

73. Stround, D., “Generalized effective-medium approach to the conductivity of an inhomogeneous material”, Physical Review B, vol. 12, no. 8, October 1975, pp. 3368-3373

74. Vauhkonen, M., Vadasz, D., Karjalainen, P.A., Somersalo, E., Kaipio, J.P., “Tikhonov regularization and prior information in electrical impedance tomography”, *IEEE Transactions on Medical Imaging*, Volume 17, Issue 2, 1998, pp. 285-293

75. Watson, G. N., “A Treatise on the Theory of Bessel Functions”, Cambridge University Press, London, 1966, pp. 132

76. Wenxin, R., Guardo, R., Adler, A., “Experimental evaluation of two iterative reconstruction methods for induced current electrical impedance tomography”, *IEEE Transactions on Medical Imaging,* Volume 15, Issue 2, 1996, pp. 180-187

77. Westerberg, A.W., Director, S.W, “A modified least squares algorithm for solving sparse n*n sets of nonlinear equations”, *Computers & Chemical Engineering,* Volume 2, Issue 2-3, 1978, pp. 77-81

78. Woo, E. J., Hua, P., Webster, J.G., Tompkins, W.J., “A Robust Image Reconstruction Algorithm and Its Parallel Implementation in Electrical Impedance Tomography.” *IEEE Transactions on Medical Imaging*, vol. 12, no. 2, June 1993, pp. 137-146

79. Yorkey, T.J., “Comparing reconstruction algorithms for electrical impedance tomography”, Ph.D. Thesis, University of Wisconsin, Madison, WI, 1986

80. Yorkey, T.J., Webster, J.G., Tompkins, W.J., “Comparing reconstruction algorithms for electrical impedance tomography”, *IEEE Transactions on Biomedical Engineering*, Volume BME-34, Issue 11, 1987, pp. 843-852

81. Zapolski, H.S., “The depolarization field inside a homogeneous dielectric: A new approach” in *American Journal of Physics,* vol. 55, 1987, pp.77 – 81

82. Zenger, D., Cai, H, “The Common Cracks in Green P/M Compacts Handbook”, Powder Metallurgy Research Center, Worcester Polytechnic Institute, Worcester, Massachusetts, March 1996

83. Zienkiewitz, O.C., “The finite element method”, Butterworth-Heinemann, Oxford; Boston: 2000, chapters 2, 3